University of Bologna

Department of Electrical, Electronic and Information Engineering

XXV Ph.D. Program in Information Technologies

ING-INF/03, 09/F2

---

Universitat Pompeu Fabra

Department of Information and Communication Technologies

Ph.D. Program in Information and Communication Technologies

# Advanced Beamforming for Distributed and Multi-Beam Networks

by

**Ilaria Thibault**

Advisers:

Prof. **Alessandro Vanelli Coralli**

Prof. **Giovanni Emanuele Corazza**

Prof. **Angel Lozano**

Coordinator:

Prof. **Claudio Fiegna**

---

# Abstract

Beamforming entails joint processing of multiple signals received or transmitted by an array of antennas. The design of this technique and the implementation challenges associated with it depend on the configuration of the array itself and on its application objectives, which can be related to a very broad domain of diverse scenarios and engineering problems.

This thesis addresses the implementation of beamforming in two distinct systems, namely a distributed network of independent sensors, and a broad-band multi-beam satellite network.

With the rising popularity of wireless sensor networks as a new tool to interact with the physical world, scientists are taking advantage of the flexibility and portability of these devices, which come with very low implementation costs. Simplicity and miniaturization, however, are inevitably intertwined with scarce power resources, which must be carefully rationed to ensure successful measurement campaigns throughout the whole duration of the application. In this scenario, distributed beamforming translates into a cooperative communication technique, allowing nodes in the network to coordinate to emulate a virtual antenna array seeking power, directivity, or diversity gains in the order of the size of the network itself, when required to deliver or receive a common message signal, or multiplex streams of data for or from multiple independent terminals. In order to achieve a desired beamforming configuration, however, all nodes in the network must agree upon the same phase and frequency reference, which is challenging in a distributed set-up where all devices have independent local oscillators. The first part of this thesis presents new algorithms for phase alignment, which prove to be more energy efficient than existing solutions. Performance of these schemes is also analytically characterized in the absence and in the presence of impairments such as fading and thermal noise, and compared to previously proposed solutions based on random search paradigms.

With the ever-growing demand for seamless and continuous broad-band connec-

tivity, satellite systems have the great potential to guarantee service where terrestrial systems still can not penetrate. In order to satisfy the constantly increasing demand for throughput, satellites are equipped with multi-fed reflector antennas to resolve spatially separated signals which co-exist on the same time and frequency slots. Users are then multiplexed in space, similarly to what happens for cellular terrestrial networks. However, incrementing the number of feeds on the payload corresponds to burdening the link between the satellite and the gateway with an extensive amount of signaling, and to possibly calling for much more expensive multiple-gateway infrastructures. This thesis focuses on an on-board non-adaptive signal processing scheme denoted as Coarse Beamforming, whose objective is to reduce the communication load on the link between the ground station and space segment, by projecting feed signals on a sub-space, and thus by reducing the need for spectral resources on the feeder link. The scenario considered is the forward link of a multi-beam, single-gateway, broad-band satellite network, and the impact of Coarse Beamforming on the performance of interference management schemes implemented at the ground station is evaluated.

# Acknowledgments

Firstly, I would like to thank Professor Giovanni Emanuele Corazza and Professor Alessandro Vanelli Coralli for giving me the possibility of engaging in a Ph.D. program in their research group at the University of Bologna. They always supported and encouraged my ideas and went along with my willingness to travel and to be in contact with many different research environments. They guided me during my Ph.D. years providing feedback to my thoughts, fueling my activity with creative and original insights, and trusting my own capabilities by allowing me to enjoy a great deal of independence and flexibility while working on my research topics. This indeed has been a challenging and rewarding experience that will always have a very important place in my life, both from a professional and a personal perspective.

A very special thank you is for Professor Angel Lozano, who welcomed me very warmly in his research group at Pompeu Fabra University, where I spent almost one year of my Ph.D., which finally became a joint degree between Bologna and Barcelona. During my time there, he closely supervised my research activity, with genuine interest and curiosity, always providing encouraging feedback and fertile grounds for constructive discussions, also with the members of his research group. If ever I happened to be in a moment of frustration, talking to him always rekindled my desire to devote my efforts to research. I miss the Pompeu Fabra Family a lot, and I will always cherish my time there.

I wish to express all my gratitude to Dr. Azadeh Faridi, with whom I had the privilege to work with during my time in Pompeu Fabra. Azadeh, not only you have been a great work-companion, so passionate about what we were doing, and so accurate in your approach towards research, but also a very dear friend, with whom I shared very nice moments in Barcelona, and I am sure we will share many more in the future.

A big thank you is for Dr. Bertrand Devillers, with whom I had the pleasure to work with when I visited CTTC for a month, during the first year of my Ph.D., in

November 2010. Dear Bertrand, thank you for investing time and effort in regularly discussing research with me! You also have become a dear friend, as well as a great work-companion. My time in CTTC gave a huge boost to my activity, definitely providing us with very interesting and unexpected results.

I would like to thank Professor Hamid Jafarkhani, from the University of California, Irvine, Professor Carlos Mosquera, from the University of Vigo, Spain, and Dr. Kai-Kit Wong, from the University College of London, UK, for accepting to review my thesis, and for devoting time and effort in sending me their comments, and precious advice. Their opinions mean a lot to me, and I was so honored to receive their feedback.

I thank my Family, especially my Mum, for always being there to support me, and to comfort me, whenever I felt overwhelmed by the fear of being stuck somewhere along my research path, or of not finding any light at the end of the tunnel.

Finally I thank with all my heart Deniz, who, during this adventure, has been the most important person by my side, always motivating me to do my best, giving me a lot of courage and strength to tackle challenges and difficulties, and always providing me with the means of finding the bright side of things.

# Contents

# List of Figures

# List of Tables

# Introduction

## 0.1 Motivation and Goals

This thesis focuses on the application of beamforming techniques in two distinct scenarios:

1. A network of distributed and independent sensors.
2. A broadband multi-beam satellite system.

Scenario 1 represents, for instance, a Wireless Sensor Network (WSN), where beamforming translates into a collaborative communication procedure denoted as *Distributed Beamforming* (DBF). According to this technique, a cluster of simple radiating devices is able to coordinate and consequently emulate a more complex and better performing virtual antenna array with potential power and directivity gains in the order of the number of cooperating nodes, with the objective of delivering a common message signal to the receiver. The benefits related to this technique are manifold, such as enhanced energy efficiency of communication, improved communication range, interference rejection, and ability to spatially multiplex streams of data. The drawback of this scheme is related to the strain in terms of network coordination needed to shape the desired beam pattern in space. This in fact is not a trivial task to pursue, since all cooperating elements are independent and spatially distributed, hence with autonomous local oscillators. The system does not have a unique phase and frequency reference, as it naturally happens for a centralized antenna array, and this makes synchronization a critical and absolutely necessary issue to be tackled. This thesis focuses on the problem of distributed phase synchronization, and presents new synchronization schemes which yield reduced overhead and complexity with respect to already existing solutions.

Scenario 2 represents a network composed by a space segment, i.e., a satellite, and a ground component, i.e., a gateway (GW). The goal of this system is to provide

interactive broadband services to a number of users located in the satellite coverage area. In order to boost system throughput, the satellite has to be equipped with a multi-fed reflector antenna which can steer multiple directive beams on the coverage area, and thus resolve spatially separated signals which co-exist on the same time and frequency slots. As intuition suggests, this comes with an increase in system complexity, which burdens the communication link between the satellite and the GW (feeder link) with an extensive amount of signaling. This thesis focuses on the study of a fixed on-board signal processing technique called *Coarse Beamforming* (CB), which, while still keeping payload complexity low, aims at reducing the amount of signals to be exchanged between the ground and the space segments, and thus at making a more efficient use of the spectral resources available on the feeder link.

## Scenario 1: Novel Contributions

In order for a distributed network of sensors to achieve a desired beamforming configuration, and thus to shape a particular beampattern in space, each node has to correctly process its outgoing (or incoming) signal. We here assume that the signals are narrow-band, hence this processing translates into locally applying a complex coefficient to the outgoing (or incoming) signal which yields the joint effect of a phase rotation and an amplitude scaling. We consider the case where the network has to steer a single beam, i.e., a maximum of radiation, in the direction of the receiver to successfully deliver a common message signal. Thus, the shaping of the beampattern has to comply with a single constraint, which is maximizing the signal strength in one direction. This condition is verified when all the transmitted signals achieve electromagnetic coherence at destination.

This work presents innovative, efficient, non-power-draining, fast, simple, and distributed phase-synchronization methods. This thesis puts forth two families of closed-loop algorithms which rely on quantized feedback from the receiver, and on the availability of predefined sets of phase adjustments that nodes can locally apply to their outgoing signals. The main idea that lies beneath these methods is that each node has to locally tune its signal phase, and the choice of the best phase adjustment is driven by the receiver's feedback. The available phase shifts result from a uniform quantization of the phase range $[0, 2\pi)$ which can be coarsely or finely quantized, according to the chosen resolution of the synchronization procedure. A finer quantization, as will be shown in the following sections, translates into better

beamforming gains, but requires more resources in terms of time to synchronize, or feedback channel bandwidth.

We denote our synchronization schemes as follows:

- Deterministic Joint Activation (DJA).
- Successive Deterministic Distributed Beamforming (SDDB).

The keyword *Deterministic* emphasizes the fact that the applicable phase corrections are extracted from predefined sets of possible values.

The performance of these synchronization schemes is evaluated in terms of achievable levels of Received Signal Strength (RSS) in given time frames. We compare our methods to a random synchronization procedure known in the literature as the Random 1-Bit-Feedback (R1BF) algorithm [1], and we show how, at the small price of a slightly increased level of network coordination, our approach outperforms R1BF in terms of time to achieve coherence, thus introducing less overhead due to phase synchronization. This is crucial for both energy saving policies, and for counteracting the effect of oscillator dynamics.

According to the DJA phase synchronization method, sensors perform, in turns, one after the other, phase rotation tests to their outgoing signals, on the basis of the chosen phase resolution. The receiver measures the RSS relative to the joint transmissions of all nodes after each of these phase adjustments, sending a one-bit feedback to inform the node whether the tested shift has improved or worsened the best achieved RSS until that moment. The node chooses the phase adjustment relative to the last positive feedback. Clearly, the finer the resolution of the set of possible phase adjustments is, the more time consuming the phase synchronization procedure becomes.

The following points summarize the main outcomes of the work relative to the DJA approach:

- Comparison in a static channel scenario, via Monte-Carlo, with the R1BF algorithm.
- Comparison in a time-varying channel scenario, via Monte-Carlo, with the R1BF algorithm.
- Introduction of a hybrid synchronization approach which combines different synchronization routines, both deterministic and random, with a view to im-

proving the convergence of the overall phase synchronization process, and to maintaining signal alignment in the case of time-varying channel fluctuations.

According to the SDDB algorithm, the receiver successively estimates the complex carrier relative to each sensor, and sends a quantized phase correction to each node so to align its phase to a fixed local bias. The number of feedback bits depends on the available capacity on the feedback link, and it determines the number of possible phase adjustments that the receiver can feedback to the nodes, i.e., the resolution. When only one bit of feedback is allowed, the receiver can only tell the node whether to flip or not its phase to sum constructively with the rest of the carriers. For SDDB, we also include Additive White Gaussian Noise (AWGN) in the model and we show that its impact on the synchronization performance can not be disregarded, as it is in the literature on random distributed phase synchronization. The performance of the SDDB algorithm is evaluated in terms of the achievable RSS for given Signal-to-Noise Ratio (SNR) levels and given quantization resolutions.

The main outcomes relative to the study of SDDB are:

- Analytical performance characterization of the SDDB algorithm in the absence of noise.
- Analytical performance characterization of the SDDB algorithm in the presence of noise with particular focus on the low- and high-SNR regimes.
- Analytical performance characterization of the SDDB algorithm in the presence of fading and noise, with emphasis on the low- and high-SNR regimes.
- Performance comparison with R1BF via Monte-Carlo.
- With a view on analytically comparing the performance of SDDB with the R1BF, we also derive an upper bound for the RSS obtained during the R1BF procedure, and characterize its usefulness.

## Scenario 2: Novel Contributions

We consider a hybrid on-board/on-ground architecture, where both the satellite and the GW actively participate in signal processing for serving a set of users on the coverage area, spatially divided into multiple-beam cells. We focus on the Forward Link (FL) of this system. The GW jointly implements beamforming and interference mitigation techniques (precoding), and the role of the on-board processing is to

guarantee that only a subset of the original stack of signals that the GW should forward to the space component, can be relayed to the satellite, in order to reduce bandwidth consumption on the feeder link. The satellite processing is fixed, in order not to burden the payload with excessive computational complexity, and we study the effect of this on-board processing on the performance of the precoder in terms of spectral efficiency and availability.

We propose two CB techniques based, respectively, on *Discrete Fourier Transform* (DFT), and *Principal Component Analysis* (PCA). Roughly, the concept of CB can be associated with a projection on a subspace. When the GW processes the user signals according to the joint beamforming and precoding algorithm, a stack of feed signals is produced, which must be relayed to the satellite: each of these signals must then be injected in each one of the antenna feeds. If CB is implemented, these signals, before being transmitted to the satellite, are projected on a subspace defined by a subset of dimensions of the DFT or the PCA basis. We call *feedlets* the result of this projection. The satellite then applies the inverse transform, reconstructing the feed signals from the feedlets. Clearly, this comes with a certain degree of feed signal degradation, according to the cardinality of the stack of feedlets. The following points summarize our novel contributions:

- We propose two different CB techniques based on DFT and PCA, respectively.
- We conduct a preliminary analysis to measure feed signal degradation as a consequence of compression both in case of an ideal analog and digital feeder link.
- We extend the analysis to the GW to User Terminals (UTs) link and consider a joint precoding and CB implementation scheme evaluating its impact on system spectral efficiency and availability when the feeder link is analog and ideal.

## 0.2 Thesis Outline

This thesis consists in two parts, namely, Part I, which focuses on Distributed Beamforming and Part II, which focuses on Coarse Beamforming. Chapters 1, 2, and 3, are included in Part I, and they provide an overview on distributed arrays and on distributed phase synchronization, the description and the analysis of our synchronization schemes, and concluding remarks, respectively. Chapters 4, 5, 6, and 7, are

included in Part II, and they provide a description of the hybrid space/ground processing considered architecture, a description of the preliminary study on Coarse Beamforming, of the impact of Coarse Beamforming on interference mitigation schemes, and concluding remarks, respectively.

The work relative to Part II of this thesis has been carried out in collaboration with the Centre Tecnològic de Telecomunicacions de Catalunya (CTTC), under the supervision of Dr. Bertrand Devillers, in the framework of the SatNEx III project, funded by the European Space Agency (ESA).

# List of Publications

## Conference Papers

$\mathcal{C}$.1 I. Thibault, A. Faridi, G. E. Corazza, A. Vanelli Coralli, A. Lozano, "*Successive Deterministic Distributed Beamforming* ", to appear in Proc. IEEE International Conference on Communications, (*ICC'13*), Budapest, Hungary, Jun. 2013.

$\mathcal{C}$.2 I. Thibault, F. Lombardo, E. A. Candreva, A. Vanelli Coralli, G. E. Corazza, "*Coarse Beamforming Techniques for Multi-Beam Satellite Networks*", in Proc. IEEE International Conference on Communications, (*ICC'12*), Ottawa, Canada, Jun. 2012.

$\mathcal{C}$.3 J. Arnau-Yañez, M. Bergmann, E. A. Candreva, G. E. Corazza, R. de Gaudenzi, B. Devillers, W. Gappmair, F. Lombardo, C. Mosquera, A. Pérez-Neira, I. Thibault, A. Vanelli Coralli, "*Hybrid Space-Ground Processing for High-Capacity Multi-Beam Satellite Systems*", in Proc. IEEE Global Communications Conference, (*GLOBECOM'11*), Houston, TX, Dec. 2011, pp. 1-6.

$\mathcal{C}$.4 F. Lombardo, E. A. Candreva, I. Thibault, A. Vanelli Coralli, G. E. Corazza, "*Multi-User Interference Mitigation Techniques for Broadband Multi-Beam Satellite Systems*", in Proc. IEEE 45th Asilomar Conference on Signals, Systems and Computers, Nov. 2011, pp. 1805-9.

$\mathcal{C}$.5 I. Thibault, G. E. Corazza, L. Deambrogio, "*Phase Synchronization Algorithms for Distributed Beamforming with Time Varying Channels in Wireless Sensor Networks*", in Proc. 7th IEEE International Wireless Communications and Mobile Computing Conference, (*IWCMC'11*), Istanbul, Turkey, Jul. 2011, pp. 77-82.

$\mathcal{C}$.6 I. Thibault, G. E. Corazza, L. Deambrogio, "*Random, Deterministic, and Hybrid Algorithms for Distributed Beamforming*", in Proc. IEEE 5th Advanced Satellite Multimedia Systems Conference and the 11th Signal Processing for Space Communications Workshop, (*ASMS/SPSC'10*), Cagliari, Italy, Sep. 2010, pp. 221-5.

### Journal Articles

$\mathcal{J}$.1 I. Thibault, A. Faridi, G. E. Corazza, A. Vanelli Coralli, A. Lozano, "*Design and Analysis of Deterministic Distributed Beamforming Algorithms in the Presence of Noise*", accepted for publication in the IEEE Transactions on Communications, 2013.

### Submitted Journal Articles

$\mathcal{SJ}$.1 I. Thibault, B. Devillers, E. A. Candreva, F. Lombardo, A. Vanelli Coralli, G. E. Corazza, "*Joint Feeder Link Bandwidth Compaction and Interference Mitigation based on a Hybrid Space/Ground Processing Architecture for a Broadband Multi-Beam Satellite System*", submitted to the International Journal of Satellite Communications and Networking, Wiley Interscience, Feb. 2012.

# Part I

# Distributed Beamforming

# Chapter 1

# Background on Distributed Beamforming

## 1.1 Centralized Beamforming

An *array* is a configuration of individual antennas which need to be coordinated to form a spatial filter. The objective of this system is to achieve successful transmission (or reception) of a signal in a desired direction in space, and effective null pointing, i.e. cancellation of signals (both in transmission and in reception), towards other target directions. A *beam* is transmission (and/or) reception of energy that is concentrated in a particular direction. *Beamforming* is a signal processing technique which foresees the combination of radio signals transmitted (or received) by a set of antennas to create the effect of a large directional antenna to counteract the effects of noise and interference. The desired signal can in fact be spatially separated from other interfering and unwanted signals, and since the array gain scales with the number of devices, the effect of noise is considerably reduced. The useful signal in a target direction is enhanced by constructive combination, whereas noise or interference are rejected by destructive combination. The information related to how the array radiates (or receives) power in space is contained in its *beampattern*, which combines the spatial characteristics of the array with the radiating capabilities of the single devices. The beampattern can be considered as a mapping between field strength and direction, and, because of reciprocity, it is the same for transmission and reception. When the signals are narrow-band, beamforming is implemented by choosing appropriate complex weights that multiply the outgoing (or incoming) signals at each sensor. A centralized array is a system where all elements are interconnected,

and locked to a unique time, frequency, and phase reference. Arrays can be uniform, i.e., the elements are uniformly placed along an imaginary line, plane, or sphere, or non-uniform. In array theory [2], mathematical models are derived to show how the interplay among the number of sensors, their spacing, the beamforming coefficients, and the signal wavelength, determines the shaping of the beampattern in space, and hence the array performance. Ideal beamforming weight vector calculation yields the exact desired beampattern, when the geometry of the system is known a priori. When the array is random, the positions of the elements are random variables, and so is the beampattern. Random array theory embraces the study of the statistical properties of beampatterns generated by random arrays [3–11].

## 1.2 Motivation for Distributed Beamforming

The miniaturization trend dictated by Moore's law is allowing for decreasing volumes and costs of given computing capacities thus boosting the popularity of WSNs [12]. Researchers are in fact taking advantage of the achievements of the semiconductor technology by designing exceptionally small sensing devices that will be engaged in the intriguing task of monitoring and observing, in an increasingly accurate manner, any physical phenomenon of interest. In a very near future, science will be fully equipped with smart, miniature nodes that will communicate over wireless links, and that will greatly expand the spectrum of potential observations and enhance granularity of surveillance by naturally blending into the environment, harmonizing with the surrounding world, and unobtrusively seeping in remote and inaccessible areas to provide reliable data. WSNs are thus paving the way for new interactions between technology and physical world and the potential benefits they can bring to society are manifold , namely:

- Enhanced forms of productivity (including manufacturing and agriculture) [13, 14].
- More reliable infrastructure and means of transport [15, 16].
- Improved emergency response.
- Reinforced homeland security [17–19].
- Smart home energy management [20].
- Close environmental and habitat monitoring [21–23].

- Health monitoring [24].

The history of WSNs finds its roots in passive logging systems that required manual download of collected data. Nowadays, WSNs have the potential to offer more efficient, autonomous, reconfigurable, less intrusive, less expensive, and easy to deploy systems where sensors convey acquired data to elected sinks through wireless links.

Clearly, simplicity and miniaturization come with some drawbacks: sensors are in fact resource constrained devices, with limited processing speed, restricted storage capacity, low communication bandwidth, and limited battery life span. In order to maximize the network's life time, applications should run in harmony with strict energy efficient policies, that must limit power consumption thus preserving battery charge. Single-node communication happens to be highly inefficient since the signal transmitted from a typically low-cost isotropic antenna is undirected and, consequently, only a fraction of the transmitted power becomes useful for communication purposes. Moreover, the transceiver is the most power-consuming element in a sensor, thus a more efficient use of this resource is desirable. Under these circumstances, collaboration comes as a compelling solution when a common message, usually the result of a sensing campaign, must be relayed to a receiver.

Cooperation and beamforming can then be merged into a single concept: *Distributed beamforming*. The distributed network of sensors emulates a virtual array to shape a specific beampattern in space, seeking power and directivity gains in the direction of the receiver, spatial diversity [25], and possibly null-pointing towards other target directions [26], as shown in Figure 1.1. This approach has been proven to be extremely power efficient: authors in [27] show how, in a network of $N$ nodes, the power efficiency achieved with cooperative beamforming scales at least by a factor of $\sqrt{N}$. This means that each node can spend $1/\sqrt{N}$ times the energy needed in a single-user channel to transmit at the same communication rate. In addition, practical implementations of distributed beamforming have been proven to be effective, [28] to considerably boost network throughput.

## 1.3 Challenges for Distributed Beamforming

For a cluster of distributed nodes, emulation of a virtual array is not trivial. As opposed to a centralized scenario, in fact, where all elements naturally share a common phase and frequency reference, and where a fixed and regular geometry guarantees tight control on the relative phase shifts among elements, this distributed set up

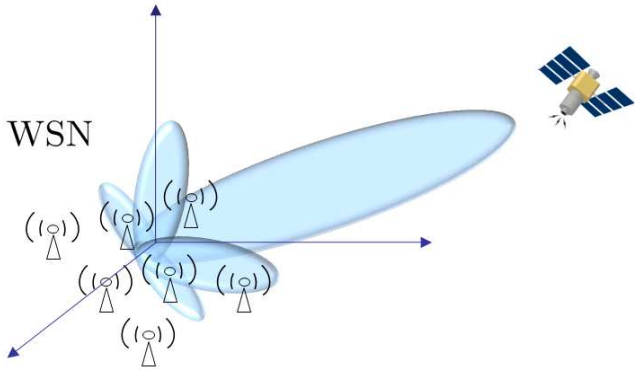


Figure 1.1: The concept of Distributed Beamforming: a wireless sensor network becomes a virtual array to steer a beam towards the receiver.

faces new challenges. Each node has in fact its own and independent local oscillator, with random initial phase as well as phase noise and carrier frequency inaccuracy, and sensor locations are typically unknown. In addition, nodes must agree upon a common message before implementing beamforming. The difference between a centralized and a distributed beamformer is schematically represented in Figure 1.2. The following issues must then be tackled:

- Carrier frequency synchronization: all the local oscillators must oscillate with the same carrier frequency in order to avoid as much as possible phase drift due to imperfect carrier synchronization.
- Carrier phase synchronization: each local oscillator has an unknown initial phase which has to be compensated for successful beam steering.
- Time synchronization: in order to successfully beamform a common message signal, nodes must share the same time reference.
- Message sharing: nodes must agree upon a common message signal which corresponds to the information to be relayed to the receiver.

Ideal beamforming weight computation for shaping a particular beampattern in space is thus quite challenging: even if there were a unique phase and frequency reference across the system, nodes should have to have Channel State Information (CSI), which, in a distributed set-up, may be unfeasible because of its excessive overhead. Moreover, even if all the sensors were somehow able to achieve perfect beamforming configuration, their local oscillators, having independent drifts, would

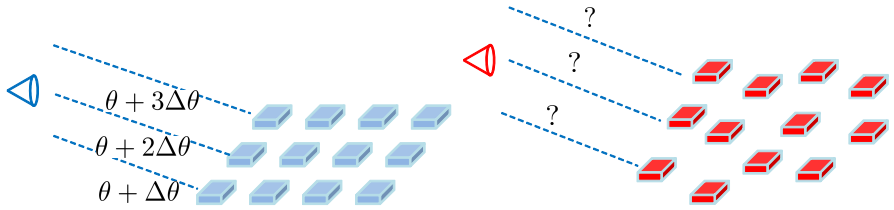


(a) Centralized Array (b) Distributed Array

Figure 1.2: A graphical representation of the difference between a centralized and a distributed array.

cause progressive misalignment of the signals, thus preventing them from maintaining the desired beampattern shape over time.

## 1.4 Distributed Arrays

Distributed beamforming has been studied in the context of relay Amplify and Forward (AF) networks and Multiple Input Single Output (MISO) architectures. Typically, in both cases, the main goal of the distributed antenna is to steer a directive beam in the direction of the receiver to achieve SNR and thus capacity gains, or directivity gains, and thus enhanced spatial filtering capabilities. In a relay set up the virtual array facilitates the communication of a source and a destination pair, hence the source broadcasts its message signal to the collaborating nodes, and differently, in a MISO architecture, nodes have to agree upon a common message before transmission. This can be done with consensus algorithms [29], or with ad hoc cross-layer schemes which aim at minimizing information sharing overhead specifically for collaborative beamforming [30–32]. Researchers have devoted many efforts to studying the performance of distributed arrays, in situations where the nodes have different degrees of CSI knowledge and different power constraints.

In the context of a source-destination pair with an AF multiple-relay network implementing single beam steering, authors in [33] focus on the case where there is perfect local CSI at the relays, at the receiver, and at the transmitter (when there is a direct link between transmitter and receiver). In addition, a per-node power constraint is considered, in order to take into account the fact that independent devices may have different battery requirements. This work presents a collaborative beamsteering protocol where the nodes not only adjust the phases of their transmissions, but also their transmit powers to optimize network performance. Follow-up work

considers the cases where nodes have knowledge of only second-order statistics [34], first-order and second-order channel statistics [35], or quantized information on the channels [36]. Authors in [37] consider imperfect CSI at the sender, and they design beamforming weights to maximize the worst-case SNR at the destination. Work in [32] then focuses on the case of multiple sources, and in [38] authors consider a threshold decode and forward relay network where the relays have multiple antennas.

In [39], a MISO network is considered, and minimization of average transmitted power is performed when full CSI at transmitters is available through a feedback channel. Also, optimal adaptive transmission strategies are developed and optimal quantizers are designed when the sensors only have quantized CSI, or when they have full local channel state information, but quantized CSI relative to the rest of the transmitters. Authors in [25] then show how DBF is beneficial for realizing spatial diversity, and they analyze a network with multiple sub-clusters of nodes that have to transmit different data streams to non-cooperating receivers, preventing undesired terminals from falling into their spot beams.

In [40], a signal reversing mechanism for beamforming weight computation is suggested. According to this scheme, the receiver sends a pilot to the network of nodes, and each sensor uses the reversed version of this beacon to modulate its message signal, in order to compensate the channel, which is assumed to be reciprocal. A practical experiment is also described to measure the beamforming gain obtained by a network of two sensors.

Authors of [41–43] study the impact of distributed beamforming on carrier-sense multiple access networks where collaborating nodes can give rise to the hidden beam problem, i.e., users that fall in a null direction of a beampattern shaped by other nodes might wrongly sense that the medium is free and transmit, creating unwanted interference. Interesting approaches are proposed to control the power of the side lobes in order to prevent this problem from arising, and to allow the network to implement collaborative beamforming thus benefiting from more energy-efficient communication.

The properties of average beampatterns created by nodes randomly distributed in space is studied thanks to the theory of random arrays [44–49].

The aim of the above-mentioned works is to derive strategies for distributed beamforming weight computation with different network constraints, different objectives, and different degrees of CSI, or to study the performance of distributed antennas, according to the random position of the sensors. The underlying assump-

tion, though, is that there is a common phase reference across the system, and that the frequency drift is negligible. Some of these works extend their results to the case of non-perfectly-synchronous nodes [27, 36], and they evaluate the impact of a certain degree of phase misalignment on network performance. However, these results are built upon the assumption that the collaborating nodes have agreed upon a unique phase and frequency reference, and possible performance degradation due to lack of synchronization are due to bounded phase offsets from the common reference. Hence, ad hoc phase and frequency synchronization algorithms are required for the network to behave as a collaborative antenna.

## 1.5 Overview on Distributed Phase Synchronization

This thesis focuses on the issue of distributed phase synchronization, considering that all the carriers have been locked to the same frequency. This can be achieved with ad hoc distributed frequency synchronization schemes, e.g. [50]. Clearly, in realistic scenarios, frequency synchronization can be achieved with a certain level of accuracy. Work in [51] investigates the effect of frequency mismatches on the performance of a distributed beamformer. This section provides an overview of the state of the art on distributed phase synchronization. Chapter 2 then presents the schemes we propose. Phase-alignment schemes can be classified as follows:

- Closed-loop methods: the synchronization procedure is driven by one-bit or full feedback from the receiver.

- Time-slotted round-trip methods: a beamforming configuration is achieved after bouncing across the network, in a time-slotted fashion, a pilot beacon sent from the receiver or from one of the source nodes.

- Node-selection procedures.

- Open-loop methods: the network synchronizes without the cooperation of the receiver.

- Blind methods: no synchronization is performed, but the natural phase drift of the oscillators is exploited to eventually achieve a desired beamforming configuration.

## Closed-loop Phase Synchronization

### One-bit feedback

In [1, 52–54] a closed-loop, distributed, and iterative phase synchronization procedure, called Random 1-Bit Feedback (R1BF) algorithm, is presented. Performance is evaluated in terms of the improvement of the Received Signal Strength (RSS), i.e., the intensity of the useful part of the aggregate signal at the receiver, as the distributed synchronization procedure unfolds. In other words, the aim of these algorithms is to enable the network to steer a beam in the desired direction in space by successively adjusting the phase of the transmitted signals according to the policy dictated by the algorithm. Clearly, the faster the received signals achieve coherence, the better in terms of energy consumption since less signaling is required for synchronization.

According to the R1BF algorithm, nodes apply, independently from one another and simultaneously, random phase adjustments to their signals. On the basis of one bit of feedback from the receiver, which informs the network if the set of random perturbations has improved or worsened the RSS, the nodes decide whether to maintain or discard the introduced phase shifts. This randomized process is carried out until the received phases achieve a desired level of coherence. Authors in [1] show that, for a wide variety of probability distribution functions (PDFs) for the phase adjustments, the procedure leads to asymptotic coherence with probability one. An analytical framework is provided in [55] to analyze the convergence of the R1BF algorithm by considering it as a random search algorithm.

The invention of this scheme triggered a considerable quantity of follow-up work. An extension for both phase and frequency synchronization is presented in [56], together with an experimental verification on 60-GHz wireless sensors. In [57] and [58], a signed variation of the R1BF algorithm is introduced to improve convergence: if nodes receive a negative feedback, they change the sign of the tested phase shifts and apply them before starting a new test. A further enhancement of this method is described in [59], where, in case of positive feedback, the nodes insist on applying the successful shift until the signal starts worsening again, and in case of negative feedback, they adopt the same strategy but by inverting the sign of the shift. In [60] this application is extended to a multiuser scenario, where $M$ separate clusters of nodes have to communicate with $M$ distinct receivers. In this work, distributed beampattern shaping is used to implement SDMA schemes: the network is divided

into $M$ sub-clusters of nodes that have to multiplex $M$ independent streams of data to $M$ non-cooperating receivers. A first attempt to incorporate the effect of Additive White Gaussian Noise (AWGN) on the random synchronization process was made in [61]. In this work, authors prove that the random procedure does not converge to 1 (which is the maximum normalized RSS), as the noiseless algorithm, but it converges to a value between $1/\sqrt{N}$, where $N$ is the number of nodes in the network, and 1. The value $1/\sqrt{N}$ corresponds to the normalized beamforming gain when all the nodes have uniformly distributed phases in $[0, 2\pi)$. New versions and improvements of R1BF are also contained in [62–65], and practical implementations have been proven to be possible, even on commodity hardware with low-quality oscillators [66].

A half duplex amplify and forward relay network is considered in [67]: an adaptive beamforming scheme based on predefined sets of deterministic perturbations of the beamforming weights driven by a one-bit feedback from the receiver is presented.

Authors in [68] analyze the problem of distributed beamforming from an information-theoretic point of view, providing a lower bound for the time required to achieve phase coherence at destination in a binary signaling case, where nodes can either flip or not their phases, on the basis of a one bit of feedback from the receiver.

### Full feedback

In [69], the received signal is considered as composed by a sum of complex signals, each one relative to the aggregate transmissions from a sub-cluster of nodes. The receiver estimates the magnitude and the phase of the signals relative to each cluster, and the objective is to align these signals in phase. As opposed to the R1BF algorithm, the feedback is based on the complex signal, and not only on the magnitude, and it is directed to subsets of nodes.

In [70] a closed-loop phase tracking routine based on Code Division Multiple Access is proposed to achieve coherent combining of signals transmitted from a cluster of distributed antennas. The receiver acts as the phase and frequency reference and sends a reference signal to the nodes. The nodes bounce this signal back, and the receiver calculates phase pre-compensation values to be fed back to the nodes. The effect of partitioning the transmitted energy between synchronization symbols and data packets is investigated, by observing its impact on the data bit error rate.

In [71], distributed transmit beamforming is evaluated in a state-space dynamic framework, where the effects of stochastic clock drift and of unpredictable kinematics

are taken into account during the tracking procedure which is driven by full feedback from the receiver. Numerical results show how near-ideal beamforming performance is obtained, as long as the period between successive training routines is sufficiently small.

### Time-slotted round-trip synchronization

A time-slotted round-trip procedure for carrier synchronization is presented, in various versions, in [72–75]. This scheme relies on the fact that if a beacon is sent from the receiver and bounced across the network of nodes before being sent back to the receiver itself, it will experience the same phase shift as if it covers the inverse route. Hence, all nodes forward to the receiver beacons that have been bounced across the network and that will all have experienced the same phase shift once they reach the receiver again. The time to synchronize is $2 \times N$ time slots, where $N$ is the number of nodes in the network, and this approach requires an extensive amount of signaling, which results in network power consumption. In this work, authors take into account phase and frequency estimation errors due to AWGN, as well as the effect of phase noise during beamforming. Regarding the latter impairment, they also quantify the amount of time during which the distributed beamformer provides an acceptable level of carrier phase alignment.

### Node-selection procedures

Node selection procedures that sort transmitters on the basis of their mutual phase alignment to efficiently create an array out of a useful subset of nodes are also analyzed in [76–79].

In [77], a virtual array is formed by selecting an appropriate subset of nodes in the network, whose signals, without having to be synchronized, are already sufficiently aligned to sum coherently at the receiver. In this case, the receiver is assumed to have global CSI, i.e., knowledge of all the channels relative to each node. The case of imperfect CSI due to noisy estimation is considered, and its impact is evaluated on the performance of the distributed beamformer for different SNR values.

### Open-loop Synchronization

When communication with the receiver is considered too costly with respect to intra-cluster communication among sensors, open-loop synchronization schemes allow for alignment procedures which do not involve exchange of signals with the receiver.

Open-loop methods are described, for example, in [50, 80]. In [50] a master-slave scheme is presented: the main idea is that a master node is elected in the distributed network of sensors, and all the cooperating devices have to lock to the master's reference carrier signal. The master broadcasts a reference beacon to all the slaves, and the slaves lock their local oscillators to this signal. This method is successful provided that the nodes are able to pre-compensate the phase mismatch of the received reference signal due to the phase response of the RF amplifiers, and to the propagation delay. The former is a fixed and precisely known offset, which can be corrected for. In order to compensate for the latter, calibration procedures are required. In [80], nodes exchange signals in a round-robin fashion to estimate their relative positions, provided that the receiver provides each node with coarse information relative to its positioning.

### Blind Approaches

Typically, in a distributed network, one of the main impairments for distributed beamforming is the oscillators' drift in time [81], which causes progressive carrier misalignment and consequent loss of coherence of the signals in the direction of the receiver. An interesting blind zero-feedback distributed beamforming is presented in [82, 83]. Here, the natural misalignment of the carriers is exploited to reach a suitable set of beamforming gains. Expression for the probability of alignment are derived for specific carrier offset distributions, and it is shown how the probability of alignment decreases as the size of the network increases.

# Chapter 2

# New Algorithms for Distributed Phase Synchronization

## 2.1 Our Contribution on Phase Synchronization

Part I of this thesis presents innovative distributed phase synchronization algorithms. Reduction of synchronization overhead with respect to R1BF has been the main driver of our approach, and we here present two closed-loop schemes, namely Deterministic Joint Activation (DJA) and Successive Deterministic Distributed Beamforming (SDDB) which rely on successive and deterministic phase update strategies to steer a maximum of radiation in the direction of the receiver. Nodes are entitled to apply to their signals one out of a choice of predefined phase adjustments, and the selection of the best shift is controlled by the receiver's feedback, which can be 1 or more bits. The difference between the two approaches is that, in case of DJA, all nodes repeatedly and jointly transmit beacons to the receiver while performing phase tests in a one by one fashion, and the receiver, by measuring the RSS of the cooperative transmission, informs each node, with one bit of feedback, whether the introduced phase adjustment has improved the quality of the signal or not. For SDDB, nodes, in turn, send pilot signals to the receiver which feeds back a quantized phase correction message to align each node's signal to a fixed local bias. As highlighted in [84], one of the main limitations of the R1BF is its slow convergence rate. Although its convergence to the maximum achievable gain has been proven in [1,55], the time length to reach signal alignment may be far too long in comparison with realistic network constraints. This means that the synchronization procedure itself not only introduces substantial latency, but burdens the network with an extensive

amount of signaling, which translates into precious energy consumption. We begin by showing how, at the expense of one extra bit of feedback, convergence of the R1BF can be improved. Then we show how, with our deterministic routines, at the price of a slight increase of network coordination, not only the synchronization latency is substantially shortened, but the power consumption is also drastically reduced. In the study of SDDB, we include the analysis of the effect of AWGN on the synchronization procedure. Surprisingly, given that the defeat of noise is one of the main drivers for DBF, all previous analyses of R1BF disregarded the impact of this impairment on the synchronization procedure. A very recent attempt to evaluate the effect of AWGN on the R1BF scheme has been proposed in [61], but this analysis does not quantify the impact of noise on the achievable gain of the algorithm.

## 2.2 General System Model and Assumptions

In the next sections, we will be discussing the R1BF algorithm from [1], and our deterministic schemes: DJA and SDDB. In this section, we present the general system model that is common to these approaches. We will then adapt this model to each particular algorithm in its corresponding section.

The following assumptions are made, in line with previous works on phase synchronization:

A1) Nodes are unaware of their own locations, of the position of the receiver, and of channel-state information (CSI).

A2) All devices are equipped with an isotropic antenna.

A3) All sensors transmit at the same power to ensure fairness in network power consumption.

A4) Since the receiver's distance is considered to be much greater than the radius of the network itself, path losses are considered to be the same for all nodes.

A5) There is no multipath and thus the effect of the channel amounts to a phase rotation, random and static for each node. This could represent, for instance, situations where the receiver is a satellite or an elevated cell site.

A6) All nodes are locked to the same carrier frequency $f_c$, and frequency drift is

considered negligible[1]. Hence, the phase shift of each local oscillator is also static and modeled as uniform in $[0, 2\pi)$.

A7) Sensors share a common time reference, i.e., time synchronization is present throughout the whole network.

In order to steer a beam towards the receiver, each transmitter should multiply its signal by an appropriate complex beamforming weight to compensate for both the channel rotation and the misalignment due to the local oscillator's phase offset. If each node had perfect knowledge of this phase compensation, the optimal beamforming weights could be applied and the signals would perfectly align in the target direction. In a distributed set up however, obtaining full CSI may not be feasible. To bypass this obstacle, we consider iterative closed-loop synchronization procedures where each transmitter can locally adjust the phase of its signal based on a low-rate feedback it receives from the destination. The phase adjustment is equivalent to multiplying the signal by a complex, unit-magnitude beamforming coefficient with a properly-selected phase. The type of feedback and the type of local phase adjustments depend on the chosen synchronization protocol.

Let $N_{\mathrm{a}}$ be the number of active devices in a given time-slot. The channel phase rotation and the phase offset of the local oscillator for node $i$ are absorbed into a single variable, $\psi_i$. In turn, the phase rotation that each transmitter has applied to its signal at time $t$ is denoted by $\phi_i[t]$. During synchronization, nodes transmit unmodulated carriers (beacons), so the complex signal at the receiver is given by

$$r(t) = e^{j2\pi f_c t} \sum_{i=1}^{N_{\mathrm{a}}} e^{j(\psi_i + \phi_i[t])} + n(t) \tag{2.1}$$

where $n(t)$ is a complex Gaussian random variable, with mean zero and variance $\sigma^2$, representing the noise at time $t$. The value of $N_{\mathrm{a}}$ is fixed throughout the synchronization.

After down conversion and sampling, at the end of time slot $m$ the resultant complex vector relative to the useful, i.e., noiseless, signal is

$$\mathcal{R}[m] = \sum_{i=1}^{N_{\mathrm{s}}[m]} e^{j(\psi_i + \phi_i[m])} \tag{2.2}$$

[1] A frequency offset will actually be present, and this translates into a maximum time window within which phase coherence can be assumed to be maintained. Loss of coherence has a detrimental effect on the beamforming gain, and this calls for re-synchronization. This thus becomes a requirement on maximum convergence time.

where $N_{\mathrm{s}}[m]$ is the number of nodes that have been involved in the synchronization procedure up to time slot $m$. The only component in this expression that is locally tunable by each transmitter is the phase of the beamforming weight. The RSS at the end of time slot $m$, given the superposition of $N_{\mathrm{s}}[m]$ carriers, is simply

$$|\mathcal{R}[m]| = \left| \sum_{i=1}^{N_{\mathrm{s}}[m]} e^{j(\psi_i + \phi_i[m])} \right|. \tag{2.3}$$

We define the RSS normalized to the total number of nodes $N$ in the network as

$$|\hat{\mathcal{R}}[m]| \triangleq \frac{|\mathcal{R}[m]|}{N} \tag{2.4}$$

and we dub it normalized RSS (NRSS). The NRSS is maximized when $\psi_i + \phi_i[m] = \Upsilon[m]$, $\forall i$, where $\Upsilon[m]$ is an arbitrary constant. The objective is to adjust $\phi_i[m]$ in order to obtain an optimal set of beamforming weights that result in received signal phases that are as close as possible to this condition of coherence.

## 2.3 Random 1-Bit Feedback Synchronization

The authors in [1] present a random procedure for phase synchronization, called R1BF, ignoring the noise term in (2.1). According to an iterative paradigm, at the beginning of each time slot, all sensors simultaneously apply a random and independent phase adjustment to their carriers. On the basis of a one-bit feedback from the receiver, they decide whether to maintain or discard the introduced phase shifts: the feedback is a *"keep"* signal if the set of phase adjustments has improved the RSS, or a *"discard"* signal otherwise. Assuming $\phi_i[m-1]$ is the best known carrier phase at the $i$th sensor at time slot $m$, each transmitter applies a random phase adjustment denoted as $\delta_i[m]$, taken from a predetermined PDF $f_{\Delta_i}(\cdot)$, striving for a potentially better phase. The applied phase increments are independent over time and across nodes. The tested phase for the $i$th node at time slot $m$ is then

$$\phi_i^{\mathrm{test}}[m] = \phi_i[m-1] + \Delta_i[m]. \tag{2.5}$$

The corresponding RSS, $|\mathcal{R}[m]|_{\mathrm{test}}$, is given by (2.3), replacing $\phi_i[m]$ with $\phi_i^{\mathrm{test}}[m]$ and $N_{\mathrm{s}}[m]$ with $N$. The receiver measures $|\mathcal{R}[m]|_{\mathrm{test}}$ and sends a feedback signal indicating whether the introduced phase shifts have improved the quality of the signal or not, i.e., if $|\mathcal{R}[m]|_{\mathrm{test}}$ is greater or smaller than $|\mathcal{R}[m-1]|$, which is the best value for the RSS up to time slot $m$. The update process for $\phi_i[m]$ can be

summarized as follows:

$$\phi_i[m] \;=\; \begin{cases} \phi_i^{\text{test}}[m], & |\mathcal{R}[m]|_{\text{test}} > |\mathcal{R}[m-1]| \\ \phi_i[m-1], & |\mathcal{R}[m]|_{\text{test}} \leq |\mathcal{R}[m-1]| \end{cases} \tag{2.6}$$

The value for the record of the best observed RSS is also updated as

$$|\mathcal{R}[m]| = \max\left(|\mathcal{R}[m]|_{\text{test}}, |\mathcal{R}[m-1]|\right) \tag{2.7}$$

This procedure is iterated and stops only once the RSS has reached a particular threshold value. Phase synchronization is thus achieved in a completely distributed fashion. No network coordination is required, and the receiver only has to estimate the strength of the aggregate of all the signals.

In [1], authors develop an analytical framework to characterize the average behavior of the NRSS as R1BF takes place. This elegant analysis considers the setting described in Section 2.2, where carriers are synchronized in frequency, with constant (but unknown) phase offsets between transmitters, and constant (but unknown) channel gains. The distributed random adaptation of the phases is shown to converge to coherence with probability one, for a vast range of perturbation distributions, and the dynamics of the algorithm are established. The latter result is based on the Central Limit Theorem to show that when the number of transmitters is large enough, the effect of the phase perturbations translates into an additive Gaussian perturbation on the resultant signal, and on the Gibbs conditioning principle of statistical mechanics, which allows for deriving a probability distribution that is plausibly applicable to the received phases, under the feedback algorithm. This analysis, however, completely disregards the impact of noise in the convergence.

## 2.4 Random 2-Bits Feedback Synchronization

In [1], authors show that the convergence rate of the R1BF procedure can be maximized by optimizing the variance of the distribution of the phase shifts $f_{\Delta_i}(\cdot)$. It is in fact shown that the convergence of the algorithm only depends on the variance of this distribution, and not on the type of distribution itself. An expression for the optimal value of variance is provided, which depends on the value of NRSS. Hence, optimal convergence rate can be achieved only if the nodes are able to fine tune this parameter at each iteration. This would though require soft feedback from the receiver.

In order to improve the convergence of the R1BF algorithm, but without a drastic increase in the rate of the feedback, we propose a 2-bits feedback scheme, and we denote it with R2BF. With two bits of feedback the nodes can acquire information not only on the increase or decrease of the RSS, but also on its quality. In particular, it is useful to spend the extra bit to refine the RSS increase information:

00 : RSS decreased.

01 : RSS increased and *far* from its maximum.

10 : RSS increased and *half way* from its maximum.

11 : RSS increased and *close* to its maximum.

Obviously the terms *far*, *half way*, and *close* must correspond to specific intervals of the RSS dynamic range. The receiver is assumed to have a way to estimate the maximum achievable RSS in order to be able to provide this feedback. On the basis of this additional information, nodes can take action by adjusting the variance of the distribution of the random phase shifts in a predefined set of three values. As also shown in [1], initially, when nodes start the synchronization process and the RSS is typically far from its maximum, high values of variance allow large phase jumps and let nodes search for the best phase shift in a wider range. As the RSS increases and becomes closer to its maximum, a smaller variance allows finer phase jumps in order not to scatter the received phasors away from their positions (possibly decreasing the RSS) and to search for the best phase value in a smaller range. We consider $\Delta_i$ to be uniformly distributed in $[-\pi/\beta, +\pi/\beta]$ where:

$\beta = \beta_1$ if $\text{RSS} < \xi_1$

$\beta = \beta_2$ if $\xi_1 \leq \text{RSS} < \xi_2$

$\beta = \beta_3$ if $\xi_2 \leq \text{RSS} < \xi_3$

and parameters $\xi_i$ are predefined thresholds, which are used when the RSS increases. The $\xi_3$ threshold is not strictly necessary but it is used as a stopping criterion. We denote this procedure as the R2BF algorithm. Figure 2.1 compares the convergence of R1BF and R2BF through Monte Carlo simulations ($10^5$ trials) for a network of $N = 100$ nodes. Different NRSS curves are depicted for R1BF corresponding to $\beta$ being 4, 20, and 40, respectively. For R2BF, parameters $\beta_1$, $\beta_2$, and $\beta_3$ are set to 4, 7, 12, respectively. As can be seen, the NRSS curve relative to R2BF always lies

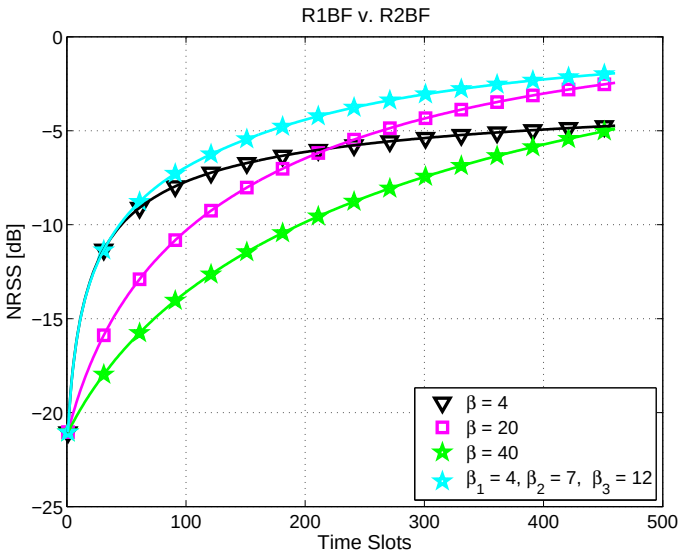


Figure 2.1: R1BF compared to R2BF via Monte-Carlo simulations, $N = 100$.

above the R1BF curve, showing that simply increasing the feedback by one bit is beneficial for the random synchronization procedure.

## 2.5 Deterministic Joint Activation

The improvement in terms of convergence brought by R2BF may not be enough for practical applications. Aiming at even faster convergence, DJA imposes tighter control on phase trajectories. To exemplify the concept, we begin by an ideal case with purely soft feedback. The receiver, being able to estimate each carrier separately, could in fact feedback the information relative to exact phase rotation each node should apply to its signal in order to achieve perfect alignment with the other carriers at destination. Although this algorithm reaches optimal performance, ideal soft feedback may be unfeasible in a distributed set up, and even a quantized version may require too much overhead. We therefore introduce simplified versions which follow a similar philosophy, but with a complexity comparable to the random solutions, i.e. a single bit. Each node is entitled to apply one phase shift, out of a predefined deterministic set of possible values, which depends on the chosen resolution. We identify this set as

$$\mathcal{S}_K = \left\{ k \times \frac{2\pi}{K},\ k = 0, \ldots, K-1 \right\} \tag{2.8}$$

where $K$ is the number of possible phase shifts, assumed to be a power of two, i.e., $K = 2^b$ where $b$ is the number of bits available for feedback. Alternatively, we can construct $\mathcal{W}_K$, the set of all possible beamforming weights for a given $K$, as follows:

$$\mathcal{W}_K \triangleq \left\{ w_k = e^{j\, k\frac{2\pi}{K}},\ k = 0, \ldots, K-1 \right\}. \tag{2.9}$$

The idea is to select the best rotation as the one that allows to improve as much as possible the RSS. This is the fundamental principle that lies beneath the deterministic approach.

The following steps summarize the flow of the deterministic algorithm:

- All nodes transmit to the receiver during the initialization time slot.
- The receiver measures the initial RSS, and stores it as $|\mathcal{R}[0]|$.

The following steps are carried out for each node in the network:

- Node $i$ rotates its signal by $k2\pi/K$ as allowed by $\mathcal{S}_K$ (the first test is for $k = 1$).
- All nodes transmit to the receiver.
- The receiver compares the new RSS value with the best value of RSS stored up to that moment, and if the rotation of node $i$ has improved the quality of the RSS, the receiver sends a positive feedback and memorizes the new RSS as the best possible value; otherwise the feedback is negative and no action is taken.
- These three steps have to be repeated for the shifts in $\mathcal{S}_K$ for $k = 1, \ldots, K-1$.
- At the end of all the possible phase tests, on the basis of the received feedback, node $i$ decides which phase shift should be finally applied to its signal.

Figure 2.2 provides an illustrative representation of how the DJA algorithm works. Figure 2.3 represents a comparison, through Monte Carlo simulations ($10^5$ trials) between DJA and R1BF. After $1 + (K-1) \times N$ time slots, i.e., the time required for all the nodes to perform their phase tests, the DJA algorithms stop, whereas R1BF continues to run until all the phases reach perfect alignment, or until a stopping criterion, defined by the specifics of the application, is verified. As can be seen, DJA offers a much faster convergence with respect to R1BF. After only $N$ time slots, more than 60% of the maximum possible gain is achieved, and after $3 \times N$ time slots the NRSS is within 1 dB away from its maximum. R1BF needs more than double the time to reach the gains achieved by DJA with $K = 2$, and $K = 4$, respectively.

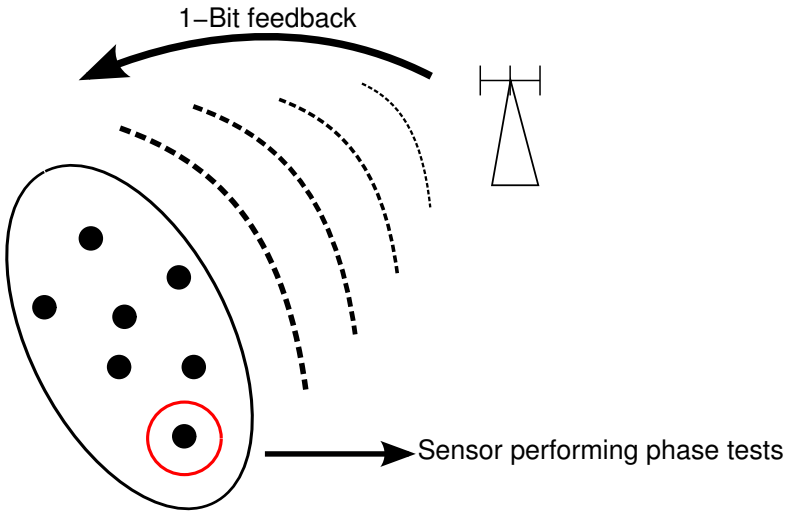


Figure 2.2: A schematic representation of how the DJA algorithm is performed.

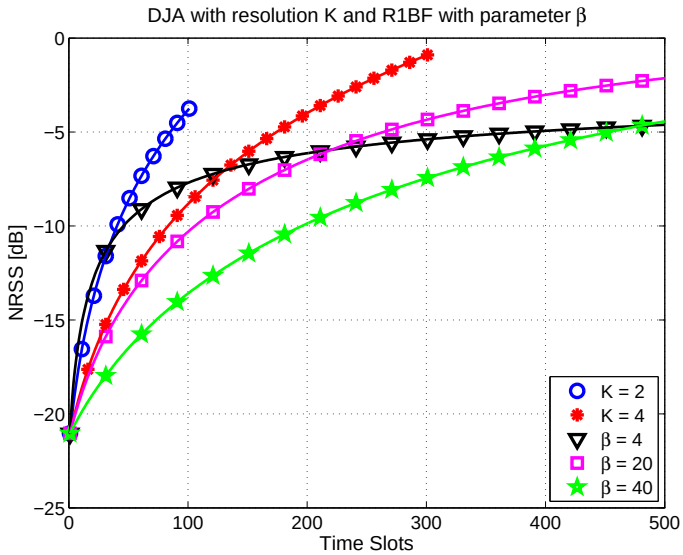


Figure 2.3: R1BF compared to DJA via Monte-Carlo simulations, $N = 100$.

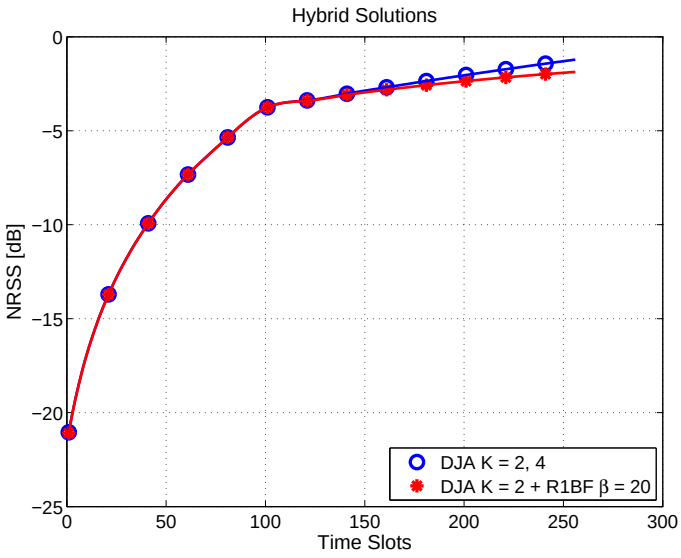


Figure 2.4: Two Hybrid solutions for phase synchronization, evaluated via Monte-Carlo simulations, $N = 100$.

## 2.6 The Hybrid Approach

The DJA approach shows a steep growth rate, but it is limited by an NRSS ceiling. Therefore, a further idea is to combine in sequence two different algorithms, such as a deterministic one and a random one, or two deterministic ones. We can define this way of proceeding as a hybrid approach. It is possible to create many combinations. We propose, as an example, the two following ones. DJA with $K = 2$ followed by R1BF: the random approach aims at improving the NRSS that the deterministic algorithm is able to achieve in $N$ time slots. This can be interpreted as a fast coarse synchronization (phasors can only be rotated by $\pi$) followed by a finer one, given by R1BF with $\beta = 20$. DJA with $K = 2$ followed by DJA with $K = 4$: the second stage aims to improve the NRSS that the first approach is able to achieve in $N$ time slots. This method can also be interpreted as the binding of a coarse synchronization with a finer one. Figure 2.4 depicts Monte Carlo curves ($10^5$ trials) relative to these two hybrid approaches, and it shows how the NRSS achieved by DJA with $K = 2$ can be considerably improved, at the expense of a wider time frame allocated for synchronization.

## 2.7 Time-Varying Channel

This section focuses on the evaluation of the performance of R1BF, R2BF, and DJA in a time-varying scenario, where the effect of signal propagation is subject to time-dependent fluctuations. Hence, assumption A5 in Section 2.2 does not hold any more, but a new channel model is introduced. We show through Monte-Carlo simulations how R2BF and DJA perform with respect to R1BF in these conditions. Here, channel fluctuations are time-dependent, and cause the transmitted signals to loose their alignment over time. The received signal quality is then subject to deterioration, and this must be taken into account throughout the course of the synchronization procedure. The time-varying channel model we use is the one described in [52], and we adapt our algorithms to these new time-varying conditions. We compare the synchronization procedures we propose with the random solution in [52], which is an adaptation of R1BF to time-varying channel conditions, and show how our DJA approach outperforms the random one. Performance is evaluated not only in terms of RSS growth at the receiver, as in the static case, but also in terms of the capability of the algorithm to counteract misalignment over time. We show how our deterministic methods prove to have very good tracking capabilities with respect to the random approach, since they allow for much faster convergence. The faster the RSS grows at the receiver, the more efficient the synchronization process is, since less signaling, and thus less energy expense, is required for the nodes to correctly align their phases.

We here comply to all the assumptions relative to system model described in Section 2.2, except for assumption A5 relative to the channel phase effect. In Section 2.2 in fact, the effect of the channel is considered to be static, but we now consider it to be subject to random fluctuations. We use the channel drift model suggested in [52], which is a random walk with non Gaussian increments. The channel phase response for transmitter $i$ at time slot $m$ is modeled as follows:

$$\psi_i[m] = \psi_i[m-1] + D_i[m]. \tag{2.10}$$

The drift process $D_i[m]$ is modeled as independent and identically distributed across sensors, stationary and uncorrelated in time, with a distribution $f_{D_i}(\cdot)$ which is considered uniform in $[-\pi/\alpha, +\pi/\alpha]$. The relation to practical cases depends on the value attributed to $\alpha$.

If the channel fluctuates, received phases are prone to misalignment over time, thus the best transmitted phase must also be tuned to maintain acceptable signal

quality at destination. The RSS, in fact, will tend to decrease on average if no measure is taken to counteract phase drift due to channel variations. In [52], the R1BF algorithm is adapted to this dynamic scenario and the procedure takes place as follows:

1) At time slot $m-1$, transmitters are aware of the best introduced beamforming phase rotation $\phi_i[m-1]$, and meanwhile the receiver keeps an estimate $\mathcal{E}_{\text{best}}[m-1]$ of the best achievable RSS. The RSS in fact has random fluctuations due to channel drift, so the receiver can only estimate its value.

2) At time slot $m$ each transmitter generates the random phase shift $\Delta_i[m]$, and applies the phase rotation to its signal so that $\phi_i^{\text{test}}[m] = \phi_i[m-1] + \Delta_i[m]$, as shown in (2.5). Thus, the received phase, in the presence of the time-varying channel drift, becomes:

$$\phi_i[m-1] + \psi_i[m-1] + \Delta_i[m] + D_i[m]. \tag{2.11}$$

3) The receiver measures the RSS, $|\mathcal{R}[m]|_{\text{test}}$, with the received phase represented in (2.11) and broadcasts to the nodes a single bit of feedback that is set to 1 if the RSS in the current time slot is better than the estimated best RSS $\mathcal{E}_{\text{best}}[m-1]$, and 0 otherwise.

4) If the feedback bit is 1, $\mathcal{E}_{\text{best}}[m]$ is updated with the new measured value of RSS, $|\mathcal{R}[m]|_{\text{test}}$, and transmitters update their best phase adjustment $\phi_i[m]$ accordingly; if the feedback bit is 0, the receiver multiplies $\mathcal{E}_{\text{best}}[m-1]$ by a factor $q < 1$ to reflect the expected signal deterioration due to the channel behavior, and nodes discard the applied phase shifts $\Delta_i[m]$.

5) This process is re-iterated in the following time slots.

The received phases are subject to two different kinds of variations: the ones applied by the transmitters, and the unknown time-varying channel responses. The update procedure can be expressed as follows:

$$\begin{aligned}
\mathcal{E}_{\text{best}}[m] &= \begin{cases} |\mathcal{R}[m]|_{\text{test}}, & |\mathcal{R}[m]|_{\text{test}} > \mathcal{E}_{\text{best}}[m-1] \\ q\,\mathcal{E}_{\text{best}}[m-1], & \text{otherwise} \end{cases} \\
\phi_i[m] &= \begin{cases} \phi_i^{\text{test}}[m], & |\mathcal{R}[m]|_{\text{test}} > \mathcal{E}_{\text{best}}[m-1] \\ \phi_i[m-1], & \text{otherwise} \end{cases}
\end{aligned} \tag{2.12}$$

Clearly this tracking version of R1BF does not converge to a precise value of RSS, but it reaches a dynamic steady state, where the tendency of the channel drift is compensated by the phase adjustments, applied to preserve coherence.

Figure 2.5 displays a comparison between the R1BF and the R2BF algorithms via Monte-Carlo ($10^5$ trials). A network of $N = 100$ nodes is considered, their initial phases before synchronization are uniformly distributed in $[-\pi, +\pi]$, and parameter $q$ is set to be 0.9. The distribution of the applied random shifts is uniform in $[-\pi/\beta, +\pi/\beta]$, and for R1BF parameter $\beta$ is set to be 20, whereas for R2BF it can have the three following values: 5, 10, 25, which correspond to the NRSS being below 20% of its maximum, between 20% and 50%, and above 50%, respectively. The distribution of the channel drift is uniform in $[-\pi/\alpha, +\pi/\alpha]$, and $\alpha$ is set to 20. As can be seen from the graph, a wider variance for the applied phase shifts in the initial stage of the algorithm provides a better NRSS growth rate.

Figures 2.6 and 2.7 represent the behavior of the R1BF and the R2BF algorithms via Monte-Carlo ($10^5$ trials) for different variances of the distribution of the channel drift. Parameter $\beta$ is set as for Figure 2.5. As can be seen, both approaches seem to have a ceiling for the NRSS, which sets the performance limit in the presence of channel drift. The R1BF appears to be more robust to channel drift. This is probably due to the fact that R2BF never actually uses the value 25 for parameter $\beta$, since the NRSS never goes beyond 30% of its maximum. Hence, the algorithm keeps using a wide variance for the distribution of the random phase adjustments, which does not prove to have a good behavior in counteracting channel phase variations.

We adapted the DJA algorithm in order for it to face time-varying conditions. The two following steps are carried out during initialization:

- All nodes transmit to the receiver.
- The receiver measures the RSS, and stores it as $\mathcal{E}_{\text{best}}[0]$.

All the nodes then carry out the following procedure, which is described for a generic node:

1) Node $i$ rotates its signal by a particular angle allowed by the chosen set of phase shifts, $\mathcal{S}_K$, defined in (2.8).
2) All nodes transmit to the receiver at time slot $m$.
3) The receiver compares the RSS with $\mathcal{E}_{\text{best}}[m-1]$, and if the introduced rotation at node $i$ has improved the quality of the RSS, the receiver sends a positive

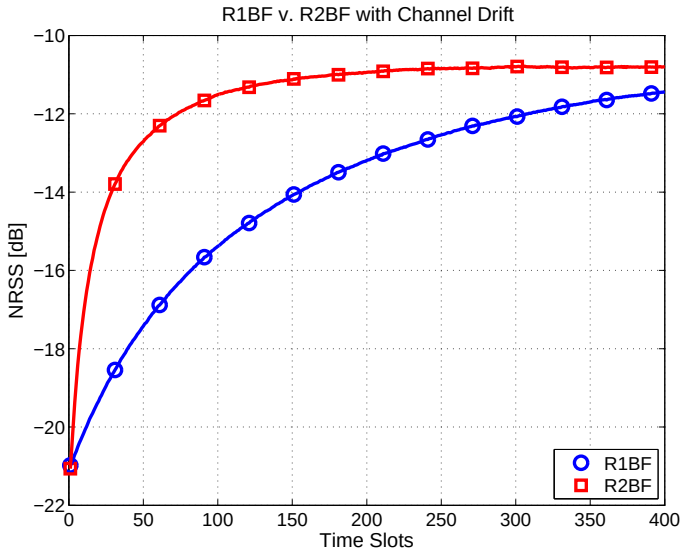


Figure 2.5: Comparison between R1BF and R2BF in presence of a time-varying channel drift, with parameter $\alpha = 20$. Parameter $\beta$ is set to 20 for R1BF, whereas it is set to be 5, 10, 25 for R2BF according to the NRSS achieved value. $N = 100$.

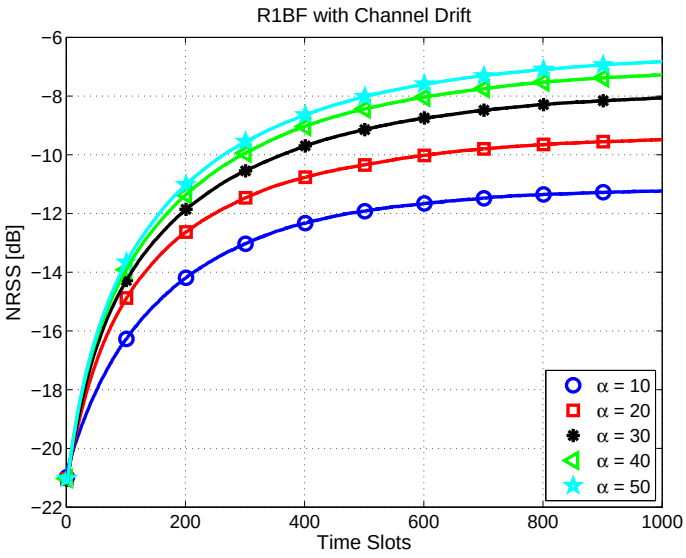


Figure 2.6: R1BF in presence of a time-varying channel drift, with different values for parameter $\alpha$. Parameter $\beta$ is set to 20, and $N = 100$.

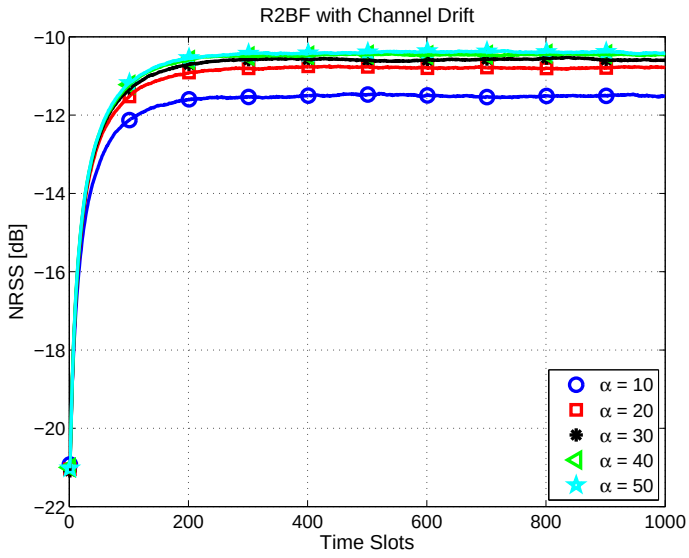


Figure 2.7: R2BF in presence of a time-varying channel drift, with different values for parameter $\alpha$. Parameter $\beta$ is set to be 5, 10, 25, and $N = 100$.

feedback and memorizes as $\mathcal{E}_{\text{best}}[m]$ the current RSS; otherwise the feedback is negative and no action is taken.

- Steps 1, 2, 3, have to be repeated for the shifts in $\mathcal{S}_K$ corresponding to $k = 1, \ldots, K-1$.
- At the end of all the possible phase tests, on the basis of the received feedback, node $i$ decides which phase shift should be applied.
- If none of the phase shifts is to be performed, i.e. the feedback has always been 0, the receiver multiplies $\mathcal{E}_{\text{best}}[m-1]$ by $q$, to estimate signal deterioration due to the time-varying channel conditions.

This procedure can be iterated over time, to counteract misalignment due to channel drift.

Figure 2.8 depicts the NRSS growth in time for the random approaches and the deterministic approaches in a time frame of $10^3$ time slots. Monte-Carlo simulations have been run with $10^5$ iterations. As already stated in the previous section, the simulation scenario is built considering a network of $N = 100$ nodes whose initial phases are uniformly distributed in $[-\pi, \pi]$. This configuration yields an initial value for the NRSS, which of course is very low since carriers are far from being coherent. In the DJA case, as the algorithm starts, in every time slot the effect of the channel

drift affects each carrier, whereas the phase rotation due to the beamforming weight is applied to one vector at a time (in particular, the one which corresponds to the node that is going through the phase testing procedure). On the receiver side, the RSS is measured at each time slot, and the stored RSS value is updated according to the strategy described above for DJA adapted to a time-varying scenario. On the basis of the feedback, the node chooses the appropriate shift from the set of possible ones. Parameter $q$ is set to 0.9, and, as stated before, the distribution of the channel drift $f_{D_i}(\cdot)$ is modeled for each channel as uniform in $[-\pi/\alpha+\pi/\alpha]$, with $\alpha = 20$. The DJA algorithm has a predefined length in time, which corresponds to the number of time slots needed for all the transmitters to perform the phase shifts. It is then necessary to re-iterate each of these algorithms to keep track of channel variations, and possibly counteract phase misalignment.

As can be seen, in these conditions random methods are not capable of raising the RSS above a certain threshold, which, for the chosen parameters, corresponds roughly to 30% of its maximum. This behavior has slight dependence on the variance of the distribution of the channel phase shifts, as depicted in Figure 2.6 and Figure 2.7. This leads us to the conclusion that random methods are not appropriate for a time-varying scenario. On the contrary, deterministic phase updates allow for much greater value of NRSS to be achieved. Precisely, as the number of possible phase shifts grows, the maximum achievable NRSS grows as well. This makes sense, since it means that each transmitter can choose among a wider range of phase adjustments for its carrier. Although, a richer set of available phase adjustments also yields to an increase in time for synchronization. As an example, DJA with $K = 2$ reaches approximately 38% of the maximum NRSS in 100 time slots (which is the time needed for all the nodes to complete one synchronization round), and DJA with $K = 4$ achieves more than 50% of the maximum in 300 time slots (which is the time needed to complete one synchronization round). A trade-off is then required between time for carrier alignment, and maximum achievable NRSS.

Deterministic methods as well have an NRSS ceiling. In fact, after a certain number of iterations, the achieved level of NRSS tends to stabilize. This means that the algorithm has reached some form steady state, and it can only compensate the drifts without excessively improving received signal quality. We then propose a variation of DJA with $K = 2$, with the objective of seeking an improvement in terms of maximum achievable NRSS. We chose $K = 2$ to start with, since it has the steepest growth rate, and the lowest NRSS ceiling. We introduce successive

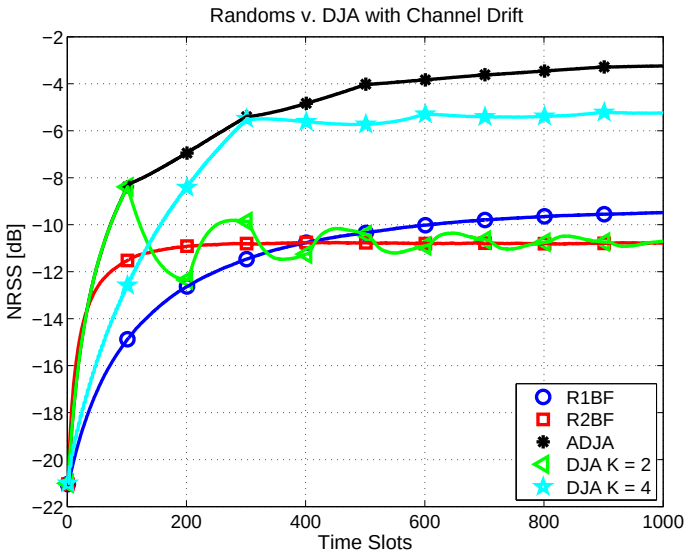


Figure 2.8: R2BF in presence of a time-varying channel drift, with different values for parameter $\alpha$. Parameter $\beta$ is set to be 5, 10, 25, and $N = 100$.

stages of finer synchronization with increasing $K$, which becomes: $\{4, 8, 16\}$. Each of these advanced synchronization stages is run twice, i.e. the advanced algorithm is iterated twice for each value of $K$. The testing procedure is still the one described above for the deterministic algorithms, adapted to a time-varying channel. This method proves to have very good performance in terms of time-varying tracking of the channel, and of NRSS improvement in time, as shown in Figure 2.8. We call this method Advanced DJA (ADJA). In fact, it allows for a very steep NRSS growth in its initial stage, and, although the steepness of the curve decreases as successive stages take over, still a continuous improvement of the NRSS is detected in the observed time frame of $10^3$ time slots. Also, during the first 300 time slots, the NRSS achieved is always greater than the one achieved with the rest of the algorithms, and at that point in time it reaches approximately 53% of the maximum value of NRSS.

## 2.8 Successive Deterministic Distributed Beamforming

We here introduce our new energy-efficient phase synchronization procedure, which we denote as Successive Deterministic Distributed Beamforming (SDDB). The power consumption due to signaling for phase alignment is drastically reduced with respect to R1BF and to previous deterministic solutions. In this algorithm, sensors transmit

successively and independently from one another and the receiver is thereby able to estimate each node's signal separately. Each sensor only wakes up during its assigned time slot to perform synchronization, while all the others remain in power-saving mode. The goal for the receiver is to align the useful part of each received signal as closely as possible to an arbitrary phase bias. Without loss of generality, we can set this phase bias to be zero. The objective of the receiver is then to align the signals of all nodes to the real axis. The procedure stops after $N$ slots, i.e., when all nodes have synchronized. Ideally, if an infinite number of bits were available for the feedback, the receiver could inform each node which exact phase shift to apply to align perfectly to the real axis. We will show that, in the absence of noise, with as few as two bits of feedback (i.e., with four possible phase shifts), beamforming gains within 1 dB of the maximum can be achieved. As mentioned earlier, this approach drastically reduces the power consumption for the training procedure with respect to R1BF and to previous deterministic solutions. In the latter cases, in each time slot, $N_{\mathrm{a}} = N$, i.e., all sensors are always active and transmitting beacons. These schemes potentially allow for cooperative transmission of information even during the synchronization procedure, and they are potentially more adaptive to time-dependent phase drift due to channel variations or oscillator dynamics, but have larger energy overhead. In SDDB, the synchronization stage and the cooperative transmission stage are disjoint, but $N_{\mathrm{a}} = 1$ in each time slot, meaning that network power consumption per time slot is reduced by a factor of $N$.

Each node is entitled to apply one phase shift, out of the predefined deterministic set of possible values, defined in (2.8), and which corresponds to the set of all possible beamforming weights for a given $K$, defined in (2.9).

Without loss of generality, we can assume that nodes get activated in the same order as their assigned index, i.e., at time slot $m$, the $m$th node is the active node transmitting its beacon to the receiver. The receiver then observes

$$r[m] = e^{j\psi_m} + n[m] \tag{2.13}$$

which is the down-converted and sampled version of the received signal defined in (2.1), when $N_{\mathrm{a}} = 1$. Since we are focusing on the feedback decision in one particular time slot, which is independent from all other time slots, for simplicity of notation we drop the index $m$. Denoting the useful part of the complex received signal by $v$, the received signal $r$ can be rewritten as

$$r = v + n. \tag{2.14}$$

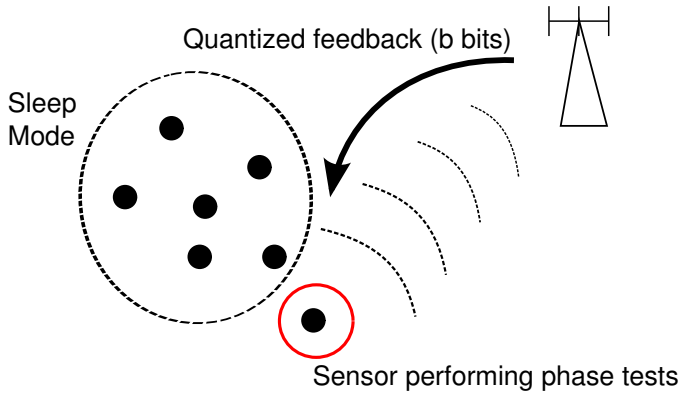


Figure 2.9: Illustrative representation of how SDDB performs. The receiver estimates the complex signal of one node at a time while the rest of the network remains in power saving mode.

For a given feedback rate, $b$, the phase space is divided into $K = 2^b$ regions. Let $D_k$ denote the $k$th region corresponding to all the phase values in $[\angle w_k - \pi/K \ , \ \angle w_k + \pi/K)$, where $\angle w_k = 2\pi k/K$ as defined in (2.9). If $r$ falls within $D_k$, the transmitted signal should be multiplied by $w_k^*$ in order to be rotated back towards the real axis. The receiver will then send $b$ bits of feedback, communicating the phase shift that has to be applied to the node's signal. Thus, the phase rotation, $\phi$, that the sensor should apply to its signal will have one of the values contained in $\mathcal{S}_K$, as given in (2.8). The new received phase for the synchronized node will then be:

$$\tilde{\psi} \triangleq \psi + \phi \tag{2.15}$$

where $\phi = -\angle w_k$. At the end of the synchronization procedure, when all the $N$ nodes have been synchronized, the final NRSS, according to (2.3) and (2.4), can be written as

$$|\hat{\mathcal{R}}_{N,K}| = \frac{1}{N}\left|\sum_{i=1}^{N} e^{j\tilde{\psi}_i}\right| \tag{2.16}$$

where the phases $\tilde{\psi}_i$ are the received phases after synchronization. Figure 2.9 is a schematic representation of the SDDB algorithm.

## 2.9 Analysis of the SDDB Algorithm

### 2.9.1 Noiseless Scenario

If the noise is negligible, $v$ can be estimated exactly. For a given $K$, the optimum beamforming weight $\hat{w}_k$ out of the set in (2.9) is

$$\hat{w}_k = \underset{w_k \in \mathcal{W}_K}{\arg\min} \|v - w_k\|^2. \tag{2.17}$$

For $K = 4$, this is graphically illustrated in Figure 2.10(a), where region boundaries are marked with dashed lines. In Figure 2.10(a), $v$ falls in $D_1$, hence $w_1$ will be chosen and $\phi = -\pi/2$. Without noise, the synchronized phases $\tilde{\psi}_i$ are independent and uniform in $D_0$, i.e., in $[-\pi/K, +\pi/K)$. This is because the unsynchronized phases $\psi_i$ are uniform in $[0, 2\pi)$ and the decision in (2.17) is noiseless, hence all the nodes will receive the correct information relative to their beamforming weight. This will then lead their synchronized phases to be uniformly distributed around the bias and to yield the best achievable NRSS for a given $K$. The performance is limited exclusively by the resolution $K$, and it is therefore of interest to characterize how the NRSS behaves as a function thereof. The following result informs of that behavior.

**Proposition 1** *In the absence of noise, the expected value of the NRSS behaves as*

$$\mathbb{E}\left[|\hat{\mathcal{R}}_{N,K}|\right] = 1 - \left(1 - \frac{1}{N} + \frac{1}{N^3}\right)\frac{\pi^2}{6K^2} + o\left(\frac{1}{K^2}\right). \tag{2.18}$$

Proof: *See Appendix B.*

Taking advantage of the fact that the number of nodes is typically large, we can further derive a lower bound on $\mathbb{E}[|\hat{\mathcal{R}}_{N,K}|]$ that is very tight for values of $N$ of interest and exact for $N \to \infty$.

**Proposition 2** *In the absence of noise, the expected value of the NRSS satisfies*

$$\mathbb{E}\left[|\hat{\mathcal{R}}_{N,K}|\right] \geq \mathbb{E}\left[\Re(\hat{\mathcal{R}}_{N,K})\right] \tag{2.19}$$

$$= \frac{K}{\pi}\sin\left(\frac{\pi}{K}\right) \tag{2.20}$$

*where* $\Re(\cdot)$ *denotes real part.*

Proof: *See Appendix B.*

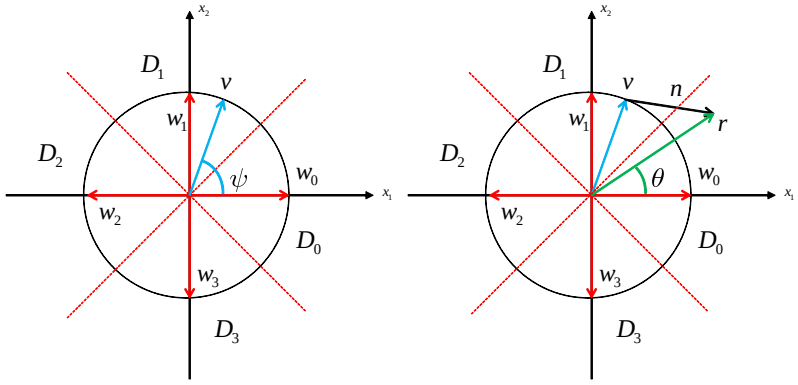


(a) $K = 4$ without noise. (b) $K = 4$ with noise.

Figure 2.10: Example of phase quantization: using $\mathcal{S}_K$ is equivalent to quantizing the phase space in $K$ regions.

Indeed, since without noise the synchronized angles are uniformly distributed around zero, the corresponding imaginary parts cancel out as $N \to \infty$.

Figure 2.11 compares the NRSS obtained through Monte-Carlo simulation for increasing $K$, with its expansion in Proposition 1 and with the lower bound in Proposition 2. A number of $10^5$ Monte-Carlo iterations has been considered to obtain the average NRSS for different values of $K$. As can be seen, the lower bound is very tight already for $N = 100$. Figure 2.12 illustrates the tightness of the lower bound in Proposition 2 with $K = 2$, which is the worst case. Since we have shown that the tightness increases with both $K$ and $N$, the bound becomes in fact exact if either of them grows without bound. The plot in Figure 2.12 represents the achievable gain as a function of $N_\mathrm{s}$, i.e., the number of synchronized nodes. This shows what the achievable normalized gain would be if $N_\mathrm{s}$ nodes were transmitting, and it is obtained by multiplying (2.20) by $N_\mathrm{s}/N$.

Next, the second raw moment of $|\hat{\mathcal{R}}_{N,K}|$ is characterized.

**Proposition 3** *In the absence of noise,*

$$\mathbb{E}\left[|\hat{\mathcal{R}}_{N,K}|^2\right] = \frac{1}{N} + \frac{N-1}{N}\left(\frac{K}{\pi}\right)^2 \sin^2\left(\frac{\pi}{K}\right). \tag{2.21}$$

Proof: *See Appendix C.*

Using Proposition 3, the variance of $|\hat{\mathcal{R}}_{N,K}|$ can be easily established.

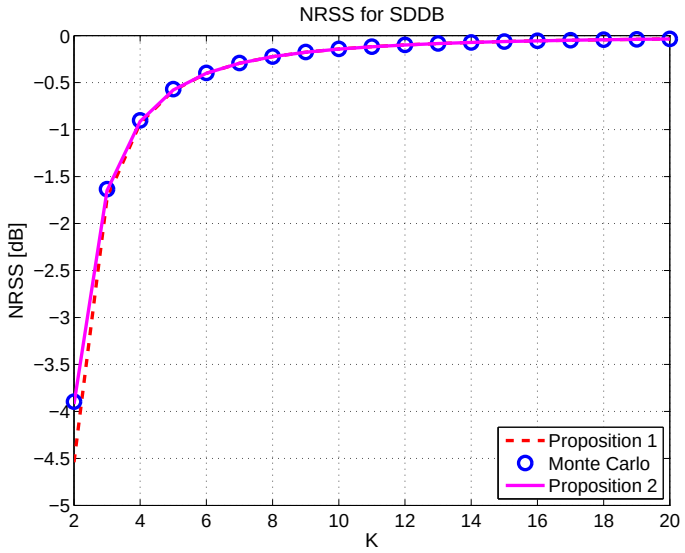


Figure 2.11: Achievable NRSS with SDDB in noiseless conditions, with $N = 100$, as a function of $K$: Monte-Carlo simulation results compared with the analytical expressions in Propositions 1 and 2.

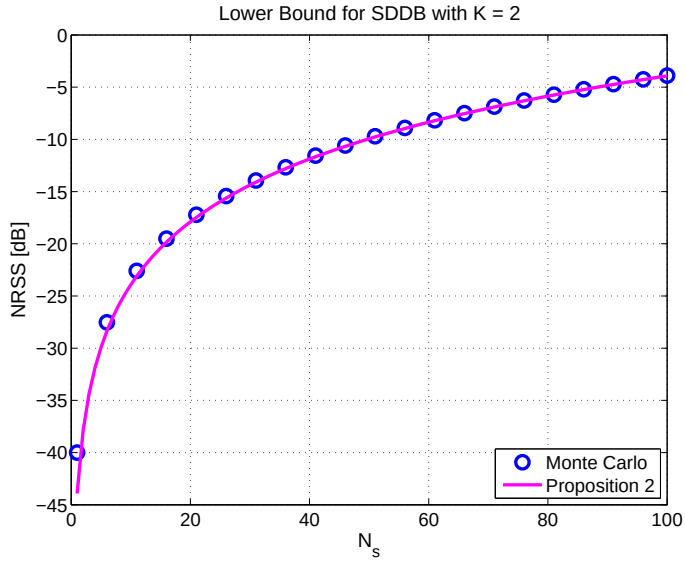


Figure 2.12: Lower bound for the achievable NRSS for SDDB when $K = 2$; expression (2.20) is used; $N = 100$.

### 2.9.2 Impact of Noise

When the noise term in (2.14) is not negligible, the receiver will have to choose $w_k$ based on the noisy received signal, $r$, as follows:

$$\hat{w}_k = \arg\min_{w_k \in \mathcal{W}_K} \|r - w_k\|^2. \tag{2.22}$$

However, since the actual goal of the receiver is aligning $v$, the useful part of $r$, there will be a non-zero probability of making an incorrect decision. Choosing a wrong phase shift will not yield the optimum NRSS that is achievable for a given $K$.

#### Achievable NRSS for Finite $K$

Let us first investigate the effect of noise on the NRSS when $K$ is finite, which corresponds to the practical cases of constrained capacity on the feedback link. Invoking the polar representation

$$r = Ae^{j\Theta} \tag{2.23}$$

the decision in (2.22) now depends exclusively on $\Theta$. If $\Theta$ falls within $D_k$, the signal for the node in question will be multiplied by $w_k^*$. Clearly, this can lead to a wrong decision, as shown in Figure 2.10(b). Due to the noise, therefore, the synchronized phases are no longer uniformly distributed and are not even necessarily within $D_0$. In this case, the distribution of the synchronized phases and, as a result, the NRSS will depend on the received SNR. We define the per-node SNR as

$$\gamma \triangleq \frac{1}{\sigma^2} \tag{2.24}$$

and denote the SNR-dependent normalized resultant by $\hat{\mathcal{R}}_{N,K,\gamma}$. The result that follows is a counterpart to Proposition 2, but with noise accounted for. As in the noiseless case, the bound is tight for values of $N$ of interest and exact for $N \to \infty$.

**Proposition 4** *In the presence of noise,*

$$\mathbb{E}\left[|\hat{\mathcal{R}}_{N,K,\gamma}|\right] \geq \frac{K}{2\pi} \int_{-\frac{\pi}{K}}^{+\frac{\pi}{K}} \sum_{k=0}^{K-1} \cos\left(\psi' - k\frac{2\pi}{K}\right) p_{D_k|\psi=\psi'}\, d\psi' \tag{2.25}$$

*where $p_{D_k|\psi=\psi'}$ is the probability that $\Theta$ falls within $D_k$ conditioned to $\psi$ being $\psi'$, namely*

$$p_{D_k|\psi=\psi'} = Prob\{\Theta \in D_k | \psi = \psi'\} = \int_{k\frac{2\pi}{K}-\frac{\pi}{K}}^{k\frac{2\pi}{K}+\frac{\pi}{K}} f_{\Theta|\psi=\psi'}(\theta) d\theta \tag{2.26}$$

*where*

$$f_{\Theta|\psi=\psi'}(\theta) = \frac{1}{2\pi} e^{-\gamma} \left\{ 1 + 2e^{\gamma \cos^2(\theta-\psi')} \sqrt{\gamma\pi} \cos(\theta - \psi') \left[ 1 - \mathcal{Q}\left( \sqrt{2\gamma} \cos(\theta - \psi') \right) \right] \right\} \tag{2.27}$$

*with* $\mathcal{Q}(\cdot)$ *the Gaussian Q-function*

$$\mathcal{Q}(x) \triangleq \frac{1}{\sqrt{2\pi}} \int_x^{+\infty} e^{-\frac{z^2}{2}} dz. \tag{2.28}$$

Proof: *See Appendix D.*

For $\gamma \to \infty$, the right-hand-side of (2.27) becomes a delta function at $\theta = \psi'$ which reduces (2.25) to the noiseless expression in Proposition 2 and, as mentioned at that point, the performance becomes limited only by the finite granularity $K$.

Particularly insightful is the analysis in the low- and high-SNR regimes. The former is representative of the conditions in which an actual sensor network necessitating of distributed beamforming might have to operate, and the latter serves as a bridge to the noiseless results presented earlier.

**Proposition 5** *At low SNR,*

$$\mathbb{E}\left[ |\hat{\mathcal{R}}_{N,K,\gamma}| \right] \geq \sqrt{\frac{\gamma}{\pi}} \frac{K}{2} \sin\left( \frac{\pi}{K} \right) + o(\gamma). \tag{2.29}$$

*Proof:* See Appendix D.

Figure 2.13 exemplifies the lower bound for the achievable NRSS in the presence of noise for $K = 2$; the exact expression in (2.25) is represented, together with its low- and high-SNR expansions respectively (2.29) and (2.20). Figure 2.14 presents the same result for $K = 4$. In both figures, the curve obtained through Monte-Carlo simulation is also represented. The average NRSS is considered for different values of SNR, ranging from $-15$ to $+20$ dB. Except for very low SNR, the bound is very tight. Figure 2.15 compares the lower bound with Monte-Carlo curves ($10^5$ trials) obtained with different values of nodes in the network, $N$, more specifically for $N = 20$, 50, 100, and for $K = 2$. As can be seen, for values of SNR of relevance, such as the interval $[-5, +5]$ dB, the bound appears to be tight even for small $N$ and small $K$. Clearly, the bound becomes more accurate as the number of nodes in the network increases. Figure 2.16 represents angular histograms for different values of SNR, and for $K = 2$. When the SNR is low, the phases remain spread out because of the high probability with which noise prevents the receiver from reporting the correct feedback. At high SNR, in contrast, the final distribution is fairly uniform over the correct slice of the plane (for $K = 2$).

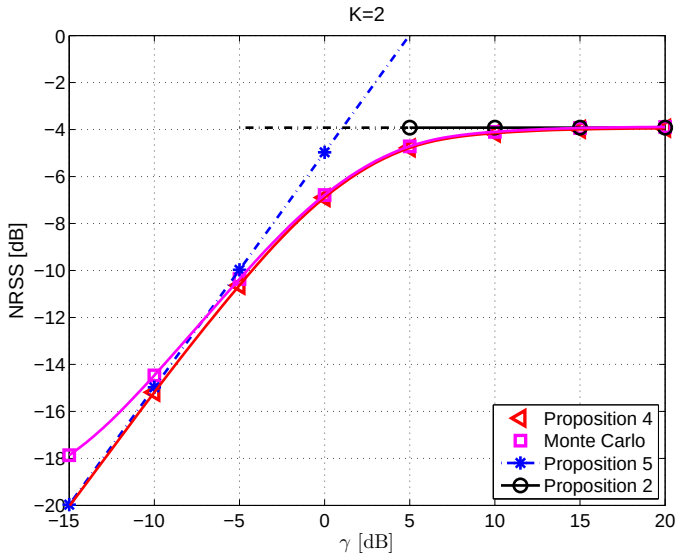


Figure 2.13: Lower bound for the achievable NRSS for SDDB for $K = 2$ as a function of the SNR with its approximations for $\gamma \to 0$, shown in (2.29) and $\gamma \to \infty$, shown in (2.20); the curve obtained through simulation is also represented, with $10^5$ Monte-Carlo iterations; $N = 100$.

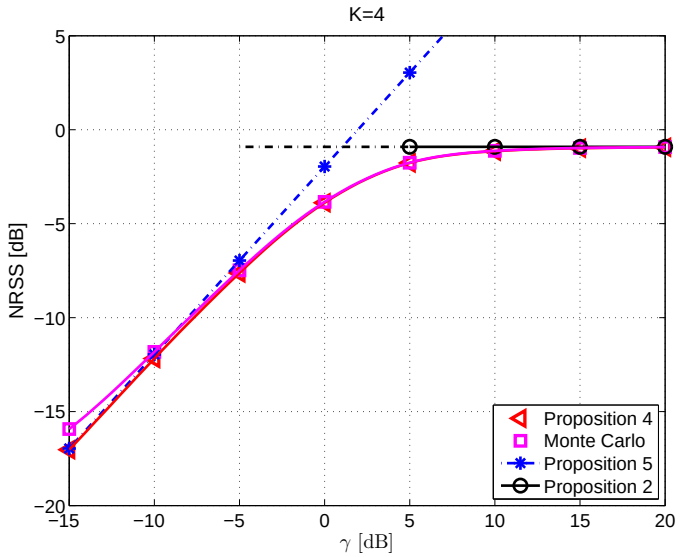


Figure 2.14: Lower bound for the achievable NRSS for SDDB for $K = 4$ as a function of the SNR with its approximations for $\gamma \to 0$, shown in (2.29) and $\gamma \to \infty$, shown in (2.20); the curve obtained through simulation is also represented, with $10^5$ Monte-Carlo iterations; $N = 100$.

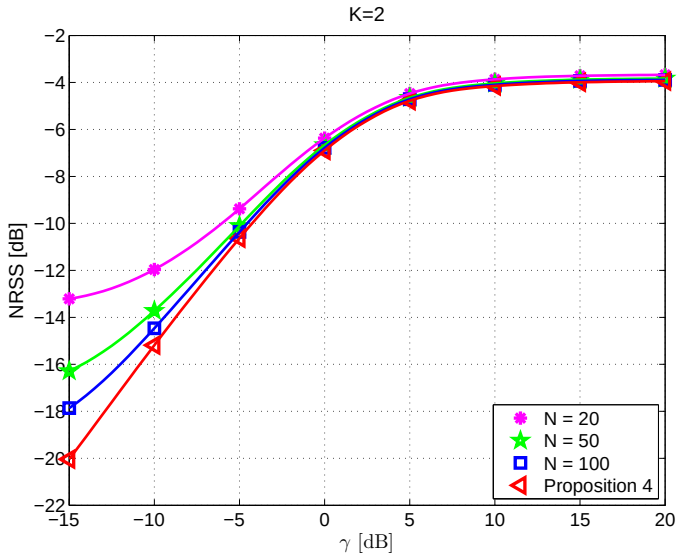


Figure 2.15: Lower bound for the achievable NRSS for SDDB with $K = 2$ as a function of the SNR compared with Monte-Carlo simulations ($10^5$ trials) with different values of $N$.

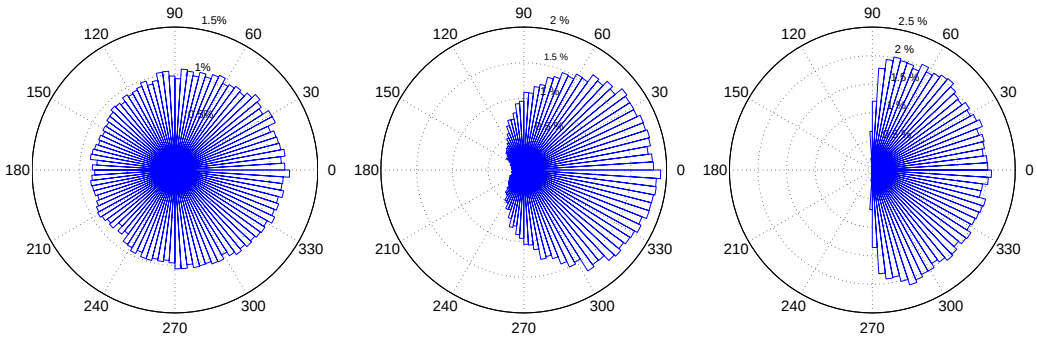

(a) SNR $= -20$ dB (b) SNR $= 0$ dB (c) SNR $= +20$ dB

Figure 2.16: Angular histograms for SDDB with resolution $K = 2$ for different SNR values.

As can be appreciated, the combination of the low- and high-SNR expressions is valid over a fairly wide range of SNRs.

### Achievable NRSS for $K \to \infty$

With infinite resolution, the regions $D_k$ collapse to punctual real phase values. There is no constraint on the capacity of the feedback link and thus the performance is limited exclusively by noise. As it turns out, this limiting behavior is approached closely with modest values of $K$, which reinforces the value of the resulting expressions.

**Proposition 6** *The expected value of* $|\hat{\mathcal{R}}_{N,\infty,\gamma}|$ *satisfies*

$$\mathbb{E}\left[|\hat{\mathcal{R}}_{N,\infty,\gamma}|\right] \geq \frac{e^{-\gamma/2}}{2}\sqrt{\pi\gamma}\left(I_0\left(\frac{\gamma}{2}\right) + I_1\left(\frac{\gamma}{2}\right)\right) \tag{2.30}$$

*where* $I_0(\cdot)$ *and* $I_1(\cdot)$ *are the modified Bessel functions of first kind of order* 0 *and* 1*, respectively.*

Proof: *See Appendix E.*

The low- and high-SNR behaviors with noise and infinite resolution are obtained by expanding Proposition 6. At low SNR, the right-hand side of (2.30) behaves as

$$\frac{\sqrt{\pi\gamma}}{2} + o\left(\gamma^2\right) \tag{2.31}$$

while, at high SNR, it behaves as

$$1 + (1 + e^{-\gamma})\, O\left(\frac{1}{\gamma}\right). \tag{2.32}$$

Figure 2.17 compares (2.30), (2.31), (2.32), and the curve obtained through Monte-Carlo simulation. The lower bound for the achievable NRSS is plotted as a function of the SNR. It can be seen that (2.31) closely matches (2.30) below roughly $-5$ dB while (2.32) closely matches it above roughly 5 dB.

## 2.10 Performance Comparison: Random v. Deterministic

In this section, we compare the random and the SDDB approaches both without and with noise. The curves again are the result of Monte-Carlo simulation campaigns with $10^5$ iterations. A network of $N = 100$ nodes is considered, and the initial phases prior to synchronization are modeled as uniform in $[0, 2\pi)$.

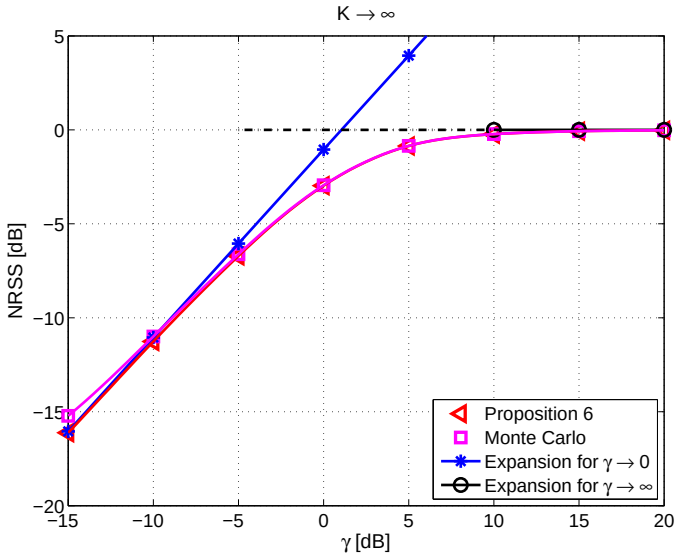


Figure 2.17: Achievable NRSS for SDDB when $K \to \infty$ as a function of the SNR expressed in (2.30), and its approximations for $\gamma \to 0$, expressed in (2.31), and $\gamma \to \infty$, expressed in (2.32); the curve obtained through simulation is also represented, with $10^5$ Monte-Carlo iterations; $N = 100$.

### 2.10.1 Noiseless Scenario

In Figure 2.18, the noiseless performance of the random algorithm (R1BF, cf. Section 2.3), is illustrated in terms of the NRSS improvement over time. A window of 450 time slots is considered. The distribution for the random shifts $f_{\Delta_i}(\cdot)$ is uniform in $[-\pi/\beta, +\pi/\beta]$ for every $i$, and the curves for distinct values of $\beta$ are shown. As can be seen, a larger variance allows for a very rapid NRSS increase in the initial stages, but at the price of a slow eventual convergence. In contrast, smaller variances yield a very low initial growth rate, in return for faster convergence as the NRSS approaches its maximum. Authors in [1] show how an adaptive behavior improves convergence. In this case, nodes can adjust the variance of the distribution, optimizing it at each iteration according to the NRSS value. But this approach is practically unfeasible since it would require the nodes to have full knowledge of the NRSS at each step, and thus the receiver to send a much higher-rate feedback. By considering the variance of this distribution to be fixed, we relate to a more practical and realistic case.

Figure 2.19 is related to SDDB without noise (cf. Section 2.9.1), presenting the NRSS as a function of the number of activated and synchronized devices, $N_s[m]$,

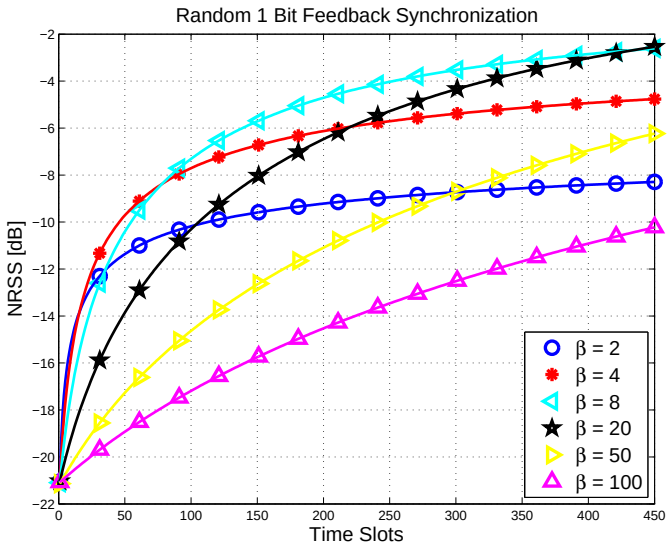


Figure 2.18: NRSS for R1BF without noise, with $N = 100$, and $f_{\Delta_i}(\cdot)$ uniform in $[-\pi/\beta, +\pi/\beta]$ for every $i$.

as given in (2.4). The plot can also be interpreted as a function of time, since nodes are synchronized successively (one per time slot) and thus the curves indicate the NRSS that would be attained by the activated nodes after a certain number of rounds. The first value of each curve corresponds to a single-node transmission, and the last value ($N_s[m] = N$) is the NRSS achieved when the complete network is beamforming. The different curves correspond to different resolutions, $K$. When the receiver can only send one bit of feedback ($K = 2$), the achievable NRSS is 4 dB away from the maximum achievable value. When $K = 4$, the attainable NRSS is within 1 dB of the maximum. As $K$ increases even further, the improvement becomes minute. Hence, the most relevant cases are $(i)$ $K = 2$, when the feedback rate is 1 bit and a fair comparison with R1BF is possible, $(ii)$ $K = 4$, which shows that simply adding one more feedback bit, SDDB yields very high gains after only $N$ time rounds, and $(iii)$ $K \to \infty$, which approximates well all the remaining values of $K$.

Figure 2.20 presents a noiseless comparison between R1BF and SDDB. The graph depicts the NRSS as a function of time (for SDDB, recall, the NRSS at a given time slot $m$ indicates the NRSS achieved by $m$ synchronized nodes). The R1BF curves correspond to different values of $\beta$, and the curves for SDDB represent the cases $K = 2$ and $K = 4$. During the first time slot, all the unsynchronized nodes in R1BF yield an initial normalized gain of $1/\sqrt{N}$. For SDDB, in turn, the initial gain corresponds

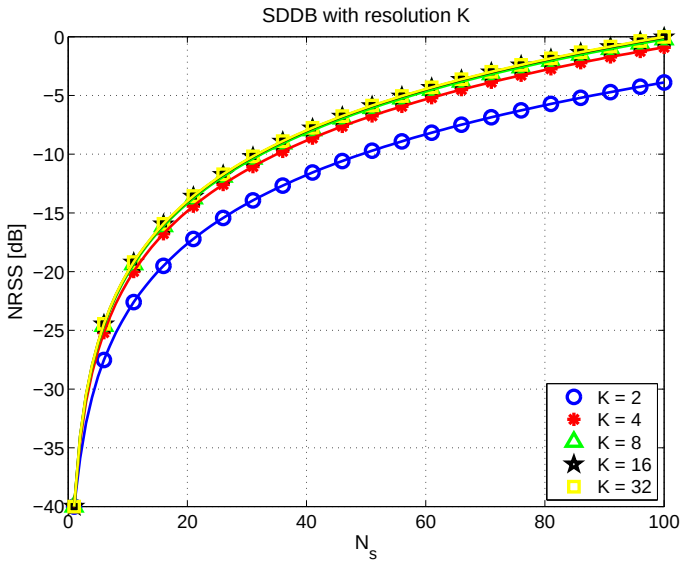


Figure 2.19: NRSS for SDDB without noise, parametrized by $K$; $N = 100$.

to a single-node transmission. With one bit of feedback, SDDB starts outperforming R1BF after 50 time slots and it becomes roughly 4 dB better after 100 slots. This comparison is for $\beta = 4$, which is the best choice for R1BF in this time frame. This improvement comes with an increase of network coordination with respect to R1BF. Nodes in fact have to be indexed and they must transmit in a predefined order. Indexing can be done once, when the network is deployed. Transmitting in turn can be achieved with a token passing mechanism, or the feedback itself could trigger the progressive awakening of each sensor. At the price of an extra feedback bit, SDDB starts outperforming R1BF after only 30 time slots, becoming roughly 8 dB better after 100 time slots. In addition, recall, SDDB has an $N$-fold power saving factor per time slot. A time frame of an order of magnitude larger is required for R1BF to achieve gains comparable to the ones achieved by SDDB in 100 time slots. As mentioned in Section 2.2, in practical scenarios the phase of each local oscillator drifts over time, causing progressive carrier misalignment and consequent loss in terms of beamforming gain. Both oscillator dynamics and frequency mismatches due to imperfect carrier synchronization have to be taken into account and properly modeled to identify the time interval within which quasi-static oscillators' phase can be assumed, identified as Oscillators' Coherence Time (OCT). The OCT interval then determines the rate of periodic phase re-synchronization in order to maintain tracking, according to the level of tolerance of the application. The problem of

modeling phase drift has been studied, for example, in [50] and [74]. In both these works, the drift is modeled as a non-stationary Gaussian process with zero mean and a time-dependent variance. For instance, in [74] the time-dependent variance of the drift $\sigma_{\mathrm{d}}^2(t)$ is expressed as $\sigma_{\mathrm{d}}^2(t) = c\Delta t$, where $c$ is a parameter dependent on the physical properties of the local oscillator and is measured in $\mathrm{rad}^2 \times \mathrm{Hz}$, and $\Delta t$ is the considered time frame in seconds. This model is based on the work in [85]. As stated in [74], for low-cost radio-frequency oscillators, parameter $c$ ranges from 1 to 20 $\mathrm{rad}^2 \times \mathrm{Hz}$. Taking $c = 10$ as the typical drift parameter, for a network of $N = 100$ nodes, it can be verified that the beamforming gain experiences a 5 dB decrease with respect to the value achieved after phase synchronization, in a time frame of 100 ms. Clearly signals continue experiencing misalignment during the synchronization procedure itself, hence, reduction of convergence time is mandatory, and this is exactly the issue we address in this work. Moreover, when phase drift is severe, or when the size of the network is so large that carrier synchronization requires long time spans, adaptive tracking methods can be employed, such as DJA, described in Section 2.5, which have been proven to be very robust against channel drift. Since the statistics of the phase drift are known, ad hoc phase re-alignment routines can be tailored to the application requirements. These are all very interesting points that pave the way for future developments of this work.

### 2.10.2 Noisy Scenario

Figure 2.21 represents a comparison (through simulation) between the R1BF and SDDB schemes when the SNR is low, specifically 0 dB, which corresponds to $\sigma^2 = 1$, in a time frame of 100 time slots. As in the noiseless case, SDDB outperforms R1BF, although the gap between them is somewhat smaller. Still, in order for R1BF to achieve a gain comparable to what SDDB achieves in 100 time slots, a time frame of an order of magnitude longer is required. The R1BF curves are for $\beta = 4$, 10, 20, respectively, whereas the SDDB curves are for $K = 2$ and $K = 4$. After 80 slots, SDDB with one feedback bit starts outperforming R1BF with $\beta = 4$, which is the best performing one, and the gap is roughly 2 dB. With two bits of feedback, the crossover occurs after less than 50 slots and the final gap increases to roughly 5 dB.

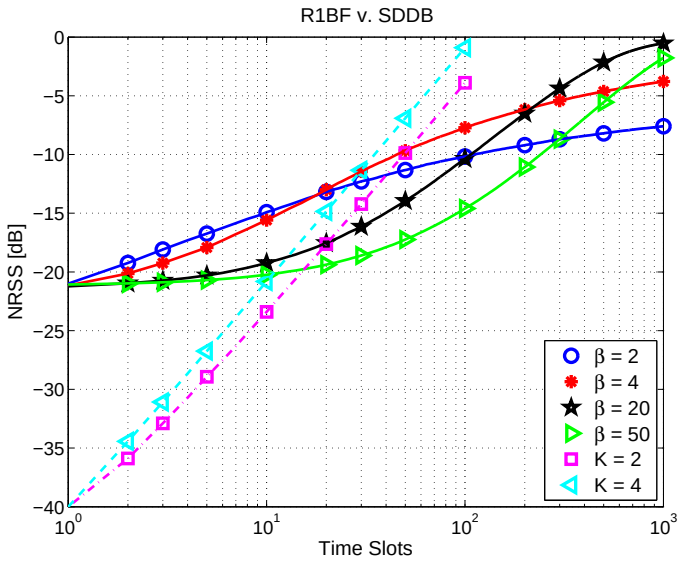


Figure 2.20: Noiseless comparison between R1BF and SDDB, with different shift distributions for R1BF ($f_{\Delta_i}(\cdot)$ uniform in $[-\pi/\beta, +\pi/\beta]$ for every $i$), and $K = 2,\ 4$ for SDDB; $N = 100$.

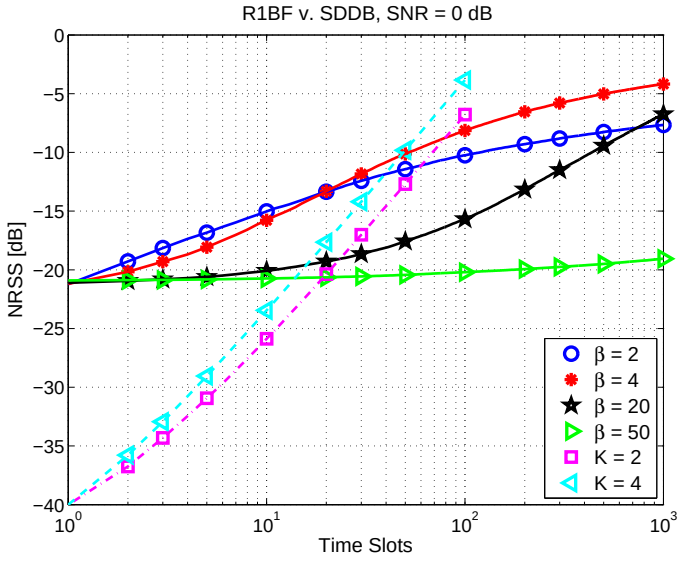


Figure 2.21: Simulated comparison between R1BF and SDDB in the presence of noise; $f_{\Delta_i}(\cdot)$ uniform in $[-\pi/\beta, +\pi/\beta]$ for every $i$; $N = 100$.

## 2.11 SDDB with Fading

In this section we consider the case where the signals from each sensor do not arrive with equal gain at the receiver. This happens when, for instance, the signals experience multipath. More specifically, we rewrite (2.2) as

$$\mathcal{R}[m] = \sum_{i=1}^{N_s[m]} G_i e^{j(\psi_i + \phi_i[m])} \tag{2.33}$$

where the effect of the channel results, as before, in a static phase rotation, $\psi_i$, uniform in $[0, 2\pi)$, and in a gain $G_i$. We assume all the $G_i$ are independent and identically distributed random variables, and their distribution is a Rayleigh PDF with parameter $p$:

$$f_G(g) = \frac{g}{p^2} e^{-\frac{g^2}{2p^2}} \tag{2.34}$$

Expression (2.13), i.e. the signal received at time slot $m$, relative to one of the nodes of the network, thus becomes:

$$r[m] = Ge^{j\psi_m} + n[m] \tag{2.35}$$

where, as stated before, $n[m]$ is complex AWGN with variance $\sigma^2$.

In a more compact form, expression (2.14) becomes

$$r = Gv + n. \tag{2.36}$$

As explained in Section 2.8, for a given feedback rate, $b$, the phase space $[0, 2\pi)$ is divided into $K = 2^b$ regions. Let $D_k$ denote the $k$th region corresponding to all the phase values in $[\angle w_k - \pi/K \ , \ \angle w_k + \pi/K)$, where $\angle w_k = 2\pi k/K$ as defined in (2.9). If $r$ falls within $D_k$, the transmitted signal should be multiplied by $w_k^*$ in order to be rotated back towards the real axis. The receiver will then send $b$ bits of feedback, communicating the phase shift that has to be applied to the node's signal. Thus, the phase rotation, $\phi$, that the sensor should apply to its signal will have one of the values contained in $\mathcal{S}_K$, as given in (2.8). The new received phase for the synchronized node will then be $\tilde{\psi}$, defined in 2.15.

At the end of the synchronization procedure, when all the $N$ nodes have been synchronized, the final NRSS can be written as

$$|\hat{\mathcal{R}}_{N,K,\gamma,p}| = \frac{1}{N} \left| \sum_{i=1}^{N} G_i e^{j\tilde{\psi}_i} \right| \tag{2.37}$$

where $\hat{\mathcal{R}}_{N,K,\gamma,p}$ denotes the NRSS in the presence of noise and fading.

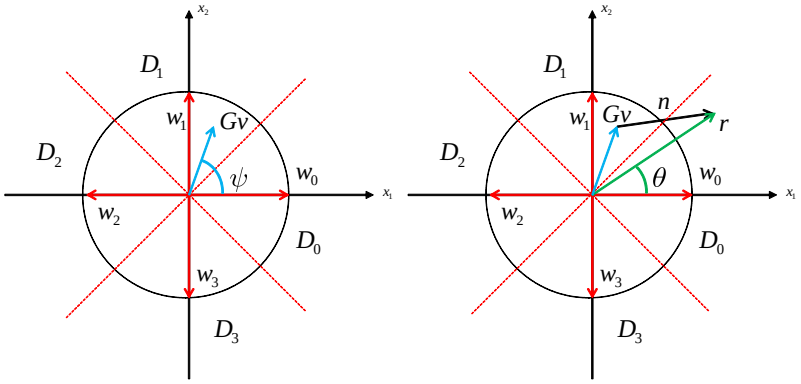


(a) $K = 4$ with fading, without noise. (b) $K = 4$ with fading and noise.

Figure 2.22: Example of phase quantization: using $\mathcal{S}_K$ is equivalent to quantizing the phase space in $K$ regions.

### 2.11.1 Noiseless Scenario

If the noise is negligible, $Gv$ can be estimated exactly. For a given $K$, the optimum beamforming weight out of the set in (2.9) is

$$\hat{w}_k = \arg\min_{w_k \in \mathcal{W}_K} \|Gv - w_k\|^2. \tag{2.38}$$

For $K = 4$, this is graphically illustrated in Figure 2.22(a), where region boundaries are marked with dashed lines. In Figure 2.22(a), $Gv$ falls in $D_1$, hence $w_1$ will be chosen and $\phi = -\pi/2$. Without noise, the synchronized phases $\tilde{\psi}_i$ are independent and uniform in $D_0$, i.e., in $[-\pi/K, +\pi/K)$. This is because the unsynchronized phases $\psi_i$ are uniform in $[0, 2\pi)$ and the decision in (2.38) is noiseless, hence all the nodes will receive the correct information relative to their beamforming weight. This will then lead their synchronized phases to be uniformly distributed around the bias and to yield the best achievable RSS for a given $K$, and a given fading distribution. The performance is limited exclusively by the resolution $K$ and by the fading, and it is therefore of interest to characterize how the NRSS behaves as a function thereof. We here denote $\hat{\mathcal{R}}_{N,K,p}$ as the noiseless $K$- and fading-dependent resultant signal. The following results informs of that behavior.

Taking advantage of the fact that the number of nodes is typically large, we can derive a lower bound on $\mathbb{E}[|\hat{\mathcal{R}}_{N,K,p}|]$ that is very tight for values of $N$ of interest and exact for $N \to \infty$.

**Proposition 7** *In the absence of noise, and in the presence of fading, the expected*

*value of the NRSS satisfies:*

$$\mathbb{E}\left[|\hat{\mathcal{R}}_{N,K,p}|\right] \geq \mathbb{E}[\Re(\hat{\mathcal{R}}_{N,K,p})] \tag{2.39}$$

$$= \mathbb{E}[G]\frac{K}{\pi}\sin\left(\frac{\pi}{K}\right) \tag{2.40}$$

Proof*: See Appendix F.*

Indeed, since without noise the synchronized angles are uniformly distributed around zero, the corresponding imaginary parts cancel out as $N \to \infty$.

**Proposition 8** *In the absence of noise and in the presence of fading, the expected value of the NRSS behaves as:*

$$\mathbb{E}[|\hat{\mathcal{R}}_{N,K,p}|] = \mathbb{E}[G] - \frac{\pi^2}{6K^2}\left(\mathbb{E}[G] - \frac{1}{N}\frac{\mathbb{E}[G^2]}{\mathbb{E}[G]} + \frac{1}{N^2}\left(\frac{\mathbb{E}[G^3]}{\mathbb{E}^2[G]} - \frac{\mathbb{E}^2[G^2]}{\mathbb{E}^3[G]}\right) - \frac{1}{N^3}\frac{\mathbb{E}[G^4]}{\mathbb{E}^3[G]}\right) + o\left(\frac{1}{K^2}\right). \tag{2.41}$$

Proof*: See Appendix F.*

Figure 2.23 compares the NRSS obtained through Monte-Carlo simulation for increasing $K$, with the results relative to Propositions 7 and 8. A number of $10^5$ Monte-Carlo iterations has been considered to obtain the average NRSS for different values of $K$, and $p$ has been set to be $1/\sqrt{2}$. As can be seen, the lower bound is very tight already for $N = 100$.

### 2.11.2 Fading with Noise

When the noise term in (2.36) is not negligible, the receiver will have to choose $w_k$ based on the noisy received signal, $r$, as expressed in (2.22).

However, since the actual goal of the receiver is aligning $Gv$, the noiseless part of $r$, there will be a non-zero probability of making an incorrect decision. Choosing a wrong phase shift will not yield the optimum NRSS that is achievable for a given $K$, and a given $p$.

#### Achievable NRSS for Finite $K$

The case of finite $K$ corresponds to the cases of constrained capacity on the feedback link. The decision in (2.38) now depends exclusively on $\Theta$, which is the phase of $r$, as shown in (2.23). If $\Theta$ falls within $D_k$, the signal for the node in question

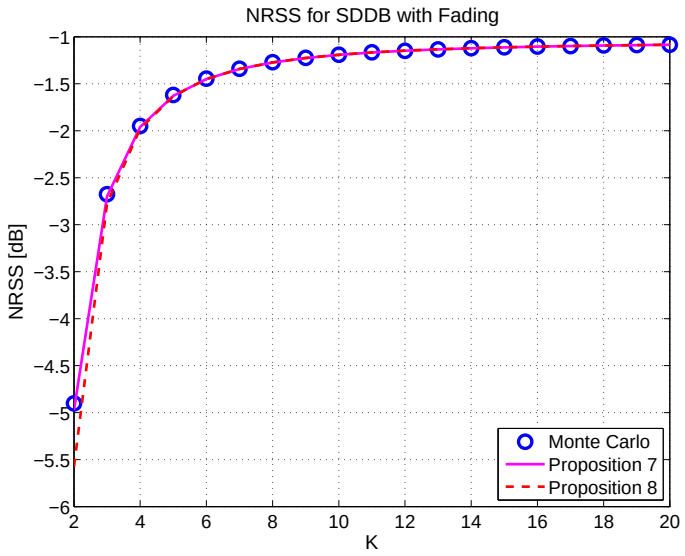


Figure 2.23: Achievable NRSS with SDDB in noiseless conditions with fading (Rayleigh parameter $p = 1/\sqrt{2}$), with $N = 100$, as a function of $K$: Monte-Carlo simulation results compared with the analytical expressions in Propositions 7 and 8.

will be multiplied by $w_k^*$. Clearly, this can lead to a wrong decision, as shown in Figure 2.22(b). Due to the noise, therefore, the synchronized phases are no longer uniformly distributed and are not even necessarily within $D_0$. In this case, the distribution of the synchronized phases and, as a result, the NRSS will depend on the received SNR. We recall the per-node SNR definition in (2.24) and we denote the SNR- and fading-dependent normalized resultant by $\hat{\mathcal{R}}_{N,K,\gamma,p}$. The result that follows is a counterpart to Proposition 7, but with noise accounted for. As in the noiseless case, the bound is tight for values of $N$ of interest and exact for $N \to \infty$.

**Proposition 9** *In the presence of noise,*

$$\mathbb{E}\left[|\hat{\mathcal{R}}_{N,K,\gamma,p}|\right] \geq \frac{K}{2\pi} \int_{-\frac{\pi}{K}}^{+\frac{\pi}{K}} \int_{0}^{+\infty} \sum_{k=0}^{K-1} g \cos\left(\psi' - k\frac{2\pi}{K}\right) \cdot f_G(g) p_{D_k|\psi=\psi',G=g} \, d\psi' dg \tag{2.42}$$

*where $p_{D_k|\psi=\psi',G=g}$ is the probability that $\Theta$ falls within $D_k$ conditioned to $\psi$ being $\psi'$, and to $G$ being $g$ namely*

$$p_{D_k|\psi=\psi',G=g} = Prob\{\Theta \in D_k | \psi = \psi', G = g\} = \int_{k\frac{2\pi}{K}-\frac{\pi}{K}}^{k\frac{2\pi}{K}+\frac{\pi}{K}} f_{\Theta|\psi=\psi',G=g}(\theta) d\theta \tag{2.43}$$

*where*

$$f_{\Theta|\psi=\psi',G=g}(\theta) = \frac{1}{2\pi} e^{-\gamma g^2} \Big\{ 1 + 2e^{\gamma g^2 \cos^2(\theta-\psi')} \sqrt{\gamma\pi} g \cos(\theta-\psi') \Big[ 1 - \mathcal{Q}\left( \sqrt{2\gamma} g \cos(\theta-\psi') \right) \Big] \Big\} \tag{2.44}$$

Proof*: See Appendix G.*

For $\gamma \to \infty$, the right-hand-side of (2.44) becomes a delta function at $\theta = \psi'$ which reduces (2.42) to the noiseless expression in Proposition 7 and, as mentioned at that point, the performance becomes limited only by the finite granularity $K$, and by fading.

We now proceed with the analysis in the low-SNR regime.

**Proposition 10** *At low SNR,*

$$\mathbb{E}\left[ |\hat{\mathcal{R}}_{N,K,\gamma,p}| \right] \geq \sqrt{\frac{\gamma}{\pi}} K p^2 \sin\left(\frac{\pi}{K}\right) + o(\gamma) \tag{2.45}$$

Proof*: See Appendix H.*

Figure 2.24 exemplifies the lower bound for the achievable NRSS in the presence of noise and fading for $K = 2$ and $p = 1/\sqrt{2}$; the exact expression in (2.42) is represented, together with its low- and high-SNR expansions respectively (2.45) and (2.40). Figure 2.25 presents the same result for $K = 4$. In both figures, the curve obtained through Monte-Carlo simulation is also represented. The average NRSS is considered for different values of SNR, ranging from $-15$ to $+20$ dB. Except for very low SNR, the bound is very tight. As can be appreciated, the combination of the low- and high-SNR expressions is valid over a fairly wide range of SNRs.

### Achievable NRSS for $K \to \infty$

With infinite resolution, the regions $D_k$ collapse to punctual real phase values. There is no constraint on the capacity of the feedback link and thus the performance is limited exclusively by noise and fading. As stated in Section 2.9.2, this limiting behavior is approached closely with modest values of $K$, which reinforces the value of the resulting expressions.

**Proposition 11** *The expected value of* $|\hat{\mathcal{R}}_{N,\infty,\gamma,p}|$ *satisfies:*

$$\mathbb{E}\left[ |\hat{\mathcal{R}}_{N,\infty,\gamma,p}| \right] \geq \int_0^\infty \int_{-\pi}^{+\pi} g \cos\theta \, f_{\Theta|G=g}(\theta|G=g) d\theta dg \tag{2.46}$$

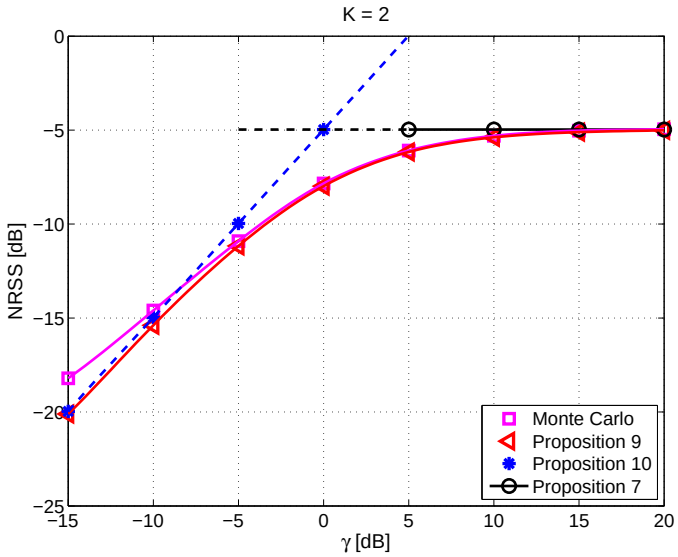


Figure 2.24: Achievable NRSS with SDDB ($K = 2$) with noise and fading (Rayleigh parameter $p = 1/\sqrt{2}$), with $N = 100$, as a function of the SNR: Monte-Carlo simulation results compared with the analytical expressions in Propositions 7, 9, and 10.

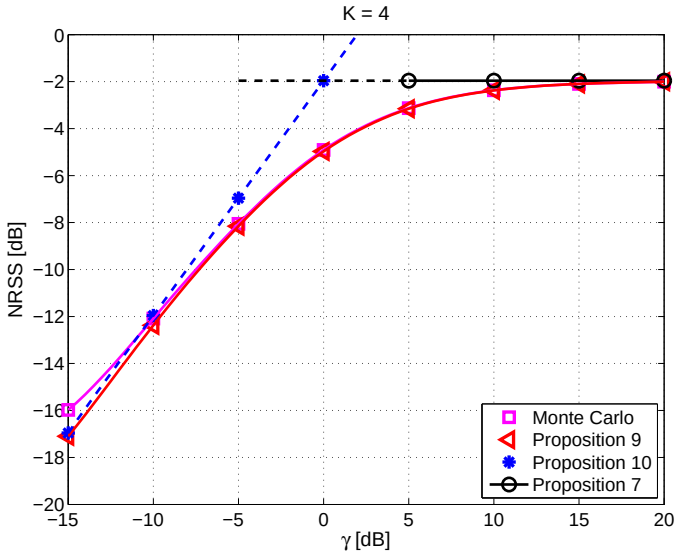


Figure 2.25: Achievable NRSS with SDDB ($K = 4$) with noise and fading (Rayleigh parameter $p = 1/\sqrt{2}$), with $N = 100$, as a function of the SNR: Monte-Carlo simulation results compared with the analytical expressions in Propositions 7, 9, and 10.

*where*

$$f_{\Theta|G=g}(\theta|G=g) = \frac{1}{2\pi} e^{-g^2\gamma} \left[ 1 + e^{g^2\gamma\cos^2\theta} 2g\sqrt{\pi\gamma}\cos\theta \Big( 1 - \mathcal{Q}\left( \sqrt{2\gamma} g \cos\theta \right) \Big) \right] \tag{2.47}$$

Proof*: See Appendix I.*

**Proposition 12** *At low SNR, the NRSS behaves as follows:*

$$\mathbb{E}\left[ |\hat{\mathcal{R}}_{N,\infty,\gamma,p}| \right] \geq \sqrt{\gamma\pi} p^2 + o(\gamma). \tag{2.48}$$

Proof*: See Appendix I.*

**Proposition 13** *At high SNR, the NRSS behaves as follows:*

$$\mathbb{E}\left[ |\hat{\mathcal{R}}_{N,\infty,\gamma,p}| \right] \geq \mathbb{E}[G]. \tag{2.49}$$

Proof*: This derives from taking the limit for* $K \to \infty$ *of* (F.7)

Figure 2.26 compares (2.46), (2.48), (2.49), and the curve obtained through Monte-Carlo simulation. The achievable NRSS is plotted as a function of the SNR. It can be seen that (2.48) closely matches (2.46) below roughly $-5$ dB while (2.49) closely matches it above roughly 5 dB.

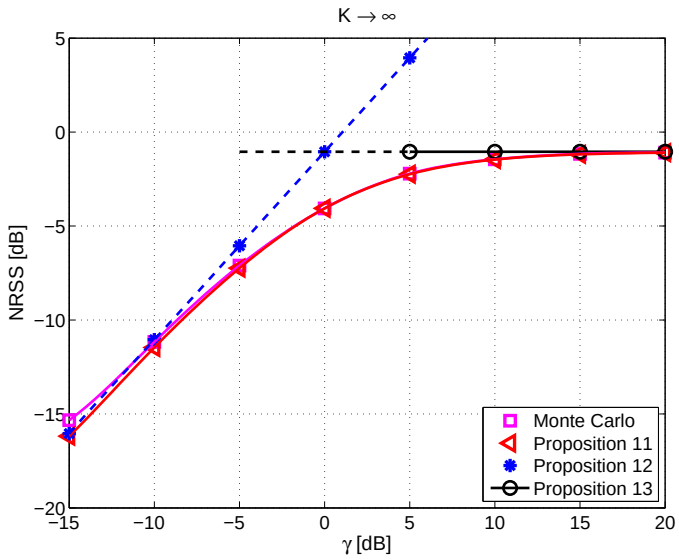


Figure 2.26: Achievable NRSS with SDDB ($K \to \infty$) with noise and fading (Rayleigh parameter $p = 1/\sqrt{2}$), with $N = 100$, as a function of the SNR: Monte-Carlo simulation results compared with the analytical expressions in Propositions 11, 12.

## 2.12 Upper Bound for R1BF

The objective of this section is to find an upper bound for the NRSS achieved with R1BF, and modeled in [1]. The aim is to find a function of time that upper bounds the performance of R1BF, which is described with a recursive function in [1]. Ultimately, a comparison with expression (2.20) is provided. This comparison is made without considering AWGN, since the study in [1] is based on a noiseless model.

In [1], R1BF is analyzed by means of stochastic approximation theory [86]:

- A recursive expression characterizes the average behavior of the NRSS at every iteration of the algorithm: the NRSS at time slot $m$ is the NRSS at time slot $m-1$ plus an increment which depends on the NRSS at time slot $m-1$. An expression for the increment is provided, and this model very closely approximates the Monte-Carlo simulations of the algorithm, for different numbers of nodes in the network, and different statistics of the random phase adjustments.
- The rate of convergence depends on the variance of the distribution of the random phase shifts (not on the type of the distribution itself).
- The value of the variance of the random shifts is optimized so that the average increase at every time slot is maximized. An expression (which depends on the NRSS) for the optimized value of variance is provided.

We here derive a function of time which upper bounds the curve obtained with the recursive evolution of the NRSS for the R1BF algorithm, in the case where the variance of the distribution of the random phase shifts is fixed throughout the whole synchronization process. This is the more realistic condition in which a sensor network would actually be operating, since tuning this variance requires a richer feedback, being this parameter NRSS-dependent. We now describe the way we derive the upper bound for the NRSS obtained with R1BF, and we provide evidence of the fact that it upper bounds the recursive function, although the rigorous proof of this claim is still not quite complete.

The following points summarize the key steps of our analysis:

- Firstly, we provide an upper bound for the first NRSS increment which, when added to the initial value of NRSS, provides the NRSS at time slot 1. The first NRSS increment is the maximum one (the curve representing the average normalized NRSS increase is in fact concave).

- Using this upper bound, we solve a second order non homogeneous differential equation to find a function of time which upper bounds the recursive NRSS function.
- The result of the second order differential equation is a tangent function. We then define the upper bound as the tangent function up to its saddle point, which is its concavity region, and from that point in time on, we define it as a properly defined straight line, to maintain the concavity of the curve.

The system model is the one described in Section 2.2, but with noise not accounted for, and the R1BF synchronization procedure of [1] is illustrated in Section 2.3. For simplicity, we here adopt the notation used in [1], by denoting with the symbol $y_m$ the NRSS at time slot $m$. By using (2.3) and (2.4), $y_m$ can be written as:

$$y_m = \frac{1}{N}\left|\sum_{i=1}^{N} e^{j(\Phi_i[m])}\right|. \tag{2.50}$$

since here $N_s[m] = N$, and where $\Phi_i[m] \triangleq \psi_i + \phi_i[m] - \psi_0[m]$, being $\psi_0[m]$ the angle of the complex resultant at time slot $m$. For convenience, authors in [1] work with rotated phases: each phase is de-rotated by $\psi_0[m]$, so that the resultant always lies on the real axis. This shift has no impact on the NRSS dynamics.

The behavior of the NRSS is modeled, according to stochastic approximation theory, as follows:

$$y_{m+1} \triangleq y_m + h_m(y_m) \qquad \text{with} \qquad y_0 = \frac{1}{\sqrt{N}} \tag{2.51}$$

where $h_m(y_m)$ denotes the increment which depends on the NRSS at time slot $m$. The expected increment of the NRSS is given by the following analytical expression:

$$h_m(y_m) = \sigma_{\Re}[m] i\left(\frac{y_m(1-\chi_m)}{\sigma_{\Re}[m]}\right) \tag{2.52}$$

where:

$$i(x) \triangleq \frac{1}{\sqrt{2\pi}} e^{-\frac{x^2}{2}} - x\mathcal{Q}(x) \tag{2.53}$$

and where:

$$\mathcal{Q}(x) = \int_x^{\infty} \frac{1}{\sqrt{2\pi}} e^{-\frac{t^2}{2}} dt \tag{2.54}$$

is the complementary cumulative distribution of a standard Gaussian random variable. $\sigma_{\Re}[m]$ represents the mean deviation in the NRSS because of the random perturbations $\Delta_i[m]$ applied at time slot $m$, and is given by:

$$\sigma_{\Re}[m]^2 = \frac{1 - \chi_m^2 - \rho_m k_m(y_m)}{2N} \tag{2.55}$$

where

$$\chi_m = \mathbb{E}[\cos(\Delta_i[m])], \tag{2.56}$$

$$\rho_m = \chi_m^2 - \mathbb{E}[\cos(2\Delta_i[m])], \tag{2.57}$$

and

$$k_m(y_m) \triangleq \mathbb{E}\left[\cos(2\Phi_1[m])|y_m\right] \tag{2.58}$$

is the mean value of the cosine of $2\Phi_1[m]$ conditioned to $y_m$, where $\Phi_1[m]$ is the received phase relative to node 1.

The following assumptions and conjectures are made on the distribution of the received phases $\Phi_1[m], \ldots, \Phi_N[m]$:

- Conditioned on $y_m$, the phases $\Phi_i[m]$ are identically distributed, interchangeable random variables.
- On the basis of the Gibbs conditioning principle of statistical mechanics, it is conjectured that the received phases $\Phi_i[m]$ follow an *exp-cosine* distribution when conditioned to the NRSS.
- The use of the Gibbs principle of statistical mechanics implies conditional independence of the $\Phi_i[m]$, which is not strictly true under the feedback algorithm.
- Because of the properties of the *exp-cosine* distribution, and since, based on the conjecture, $k_m(y_m)$ only depends on $y$ and not on $m$, $k(y)$ is given by:

$$k(y) \equiv \frac{I_2\left(\eta(y)\right)}{I_0\left(\eta(y)\right)} \tag{2.59}$$

  where $I_2$ and $I_0$ are the modified Bessel functions of orders 2 and 0, respectively, and the function $\eta(y)$ is such that $\frac{I_1(\eta)}{I_2(\eta)} = y$, where $I_1$ is the modified Bessel function of order 1. This derives from the properties of the exp-cosine distribution.

Intuitively, if the NRSS is large, the received phases can be expected to be close to zero (i.e. close to alignment, since, without loss of generality, the system is always rotated on the real axis), and thus $k(y)$ to be close to 1. On the other hand, for small NRSS the phases are expected to be far from alignment, thus distributed in $[0, 2\pi]$, so in this case $k(y)$ is close to zero.

As stated above, we here consider that the variance of the distribution $f_{\Delta_i}(\cdot)$ is fixed, and not optimized at each step, according to the optimized expression provided in [1]. Tuning this variance would in fact require a much richer feedback

than the simple 1 bit, which is the main feature of this algorithm. Hence, parameter $\chi_m$ is here not time-dependent, and the subscript $m$ can thus be dropped yielding the symbol $\chi$:

$$\chi = \mathbb{E}[\cos(\Delta_i)], \tag{2.60}$$

where we assume, without loss of generality, that $\Delta_i$ is uniformly distributed in $[-\pi/\beta, +\pi/\beta]$ for every $i$. The NRSS behavior in fact only depends on the variance of this distribution, and not on the actual PDF.

At the very first iteration of the R1BF algorithm, $y_1$ is obtained as follows:

$$y_1 = y_0 + \sqrt{\frac{1-\chi^2}{2N}} \left( \frac{1}{\sqrt{2\pi}} e^{-\frac{y_0^2(1-\chi)^2}{2\sigma_{\Re}[0]}} - \frac{y_0(1-\chi)}{\sigma_{\Re}[0]} \mathcal{Q}\left( \frac{y_0(1-\chi)}{\sigma_{\Re}[0]} \right) \right) \tag{2.61}$$

At this point:

- $k_0(y) = 0$ (since it is the mean value of the cosine of the $i$-th received phase: at the beginning they are all uniform in $[0, 2\pi]$ so this value is zero), and it can be neglected from (2.55), thus:

$$\sigma_{\Re}[0] = \sqrt{\frac{1-\chi^2}{2N}} \tag{2.62}$$

- $\chi = E[\cos(\Delta_i)] = (\beta/\pi) \times \sin(\pi/\beta)$.

The first increment is then as follows:

$$h_0(y_0) = \sigma_{\Re}[0] \left( \frac{1}{\sqrt{2\pi}} e^{-\frac{y_0^2(1-\chi)^2}{2\sigma_{\Re}^2[0]}} - \frac{y_0(1-\chi)}{\sigma_{\Re}[0]} \mathcal{Q}\left( \frac{y_0(1-\chi)}{\sigma_{\Re}[0]} \right) \right) \tag{2.63}$$

The first increment is the maximum possible one, since it is shown in [1] that $h_m(y_m)$ is a decreasing function of $y$. By defining, for simplicity:

$$p \triangleq \sigma_{\Re}[0] \tag{2.64}$$

$$q \triangleq (1-\chi) \tag{2.65}$$

(2.63), according to (2.52), then becomes:

$$h_0(y_0) = p \left( \frac{1}{\sqrt{2\pi}} e^{-\frac{1}{2}\left(\frac{q}{p} y_0\right)^2} - \frac{q}{p} y_0 \mathcal{Q}\left[ \frac{q}{p} y_0 \right] \right) \tag{2.66}$$

by expanding $h_0(\xi)$ for $\xi \to 0$ we get:

$$h_0(\xi) = \frac{p}{\sqrt{2\pi}} - \frac{q}{2}\xi + \frac{q^2}{2p\sqrt{2\pi}}\xi^2 + O(\xi)^3 \tag{2.67}$$

We define:

$$\mathcal{F}(\xi) \triangleq \frac{p}{\sqrt{2\pi}} - \frac{q}{2}\xi + \frac{q^2}{2p\sqrt{2\pi}}\xi^2 \tag{2.68}$$

which approximates $h_0(\xi)$ for $\xi \to 0$. By defining the parameters:

$$a \triangleq -\frac{q}{2} \tag{2.69}$$

$$b \triangleq \frac{-q^2}{2p\sqrt{2\pi}} \tag{2.70}$$

$$k \triangleq \frac{-p}{\sqrt{2\pi}} \tag{2.71}$$

we use the expression on the right hand side of (2.68) to write the following second order non-homogeneous differential equation:

$$\frac{d\mathcal{Y}(t)}{dt} = a\mathcal{Y}(t) - b\mathcal{Y}^2(t) - k \quad \text{with} \quad \mathcal{Y}(0) = y_0 = \frac{1}{\sqrt{N}} \tag{2.72}$$

The objective is to find an expression for $\mathcal{Y}(t)$, which is a candidate upper bound for (2.51), as long as certain conditions discussed below are verified. Equation (2.72) is a known differential equation, and it is called logistic differential equation with constant harvesting. There are three different possible solutions for this equation, depending on the relationship among coefficients. Because of how $a$, $b$ and $k$ are defined in (2.69), (2.70), (2.71), we have that $4bk > a^2$ always. In fact:

$$4bk = 4\left(\frac{-q^2}{2p\sqrt{2\pi}}\right)\left(\frac{-p}{\sqrt{2\pi}}\right) = \frac{q^2}{\pi} \tag{2.73}$$

$$a^2 = \frac{q^2}{4} \tag{2.74}$$

hence, $4bk > a^2$ is always verified. As a consequence, the solution of Equation (2.72) is:

$$\mathcal{Y}(t) = \frac{a}{2b} - \frac{\sqrt{4bk - a^2}}{2b}\text{Tan}\left[\frac{t}{2}\sqrt{4bk - a^2} - c\right] \tag{2.75}$$

where parameter $c$ depends on the initial condition as follows:

$$c = \text{Arctan}\left[\frac{2b\mathcal{Y}(0) - a}{\sqrt{4bk - a^2}}\right] \tag{2.76}$$

By reconverting the parameters in terms of $p$ and $q$ we have:

$$\begin{aligned}\mathcal{Y}(t) =& \sqrt{\frac{\pi}{2}}\frac{p}{q} + \sqrt{2\pi}\sqrt{\frac{1}{\pi} - \frac{1}{4}}\frac{p}{q}\text{Tan}\left\{\frac{t}{2}\sqrt{\frac{1}{\pi} - \frac{1}{4}}q\right. \\ &\left. - \text{Arctan}\left[\frac{1}{\sqrt{\frac{1}{\pi} - \frac{1}{4}}}\left(\frac{1}{2} - \frac{q}{p}\frac{y_0}{\sqrt{2\pi}}\right)\right]\right\}.\end{aligned} \tag{2.77}$$

By writing the solution of the logistic equation with constant harvesting in terms of the parameters of the algorithm used in Equation (2.61) we obtain:

$$\mathcal{Y}(t) = \sqrt{\frac{\pi(1+\chi)}{4N(1-\chi)}} + \sqrt{\frac{\pi(1+\chi)}{N(1-\chi)}}\sqrt{\frac{1}{\pi}-\frac{1}{4}}\mathrm{Tan}\left\{\frac{t}{2}(1-\chi)\sqrt{\frac{1}{\pi}-\frac{1}{4}} - \mathrm{Arctan}\left[\frac{1}{\sqrt{\frac{1}{\pi}-\frac{1}{4}}}\left(\frac{1}{2}-\sqrt{\frac{(1-\chi)}{\pi(1+\chi)}}\right)\right]\right\} \tag{2.78}$$

The solution (2.78), being a tangent function, has asymptotes, and the expression of the time instant $t_1$ relative to the first asymptote is the following:

$$t_1 = \frac{2(\frac{\pi}{2}+c)}{\sqrt{4bk-a^2}} \tag{2.79}$$

$$= \frac{1}{\sqrt{\frac{1}{\pi}-\frac{1}{4}}(1-\chi)}\left\{\pi + 2\mathrm{Arctan}\left[\frac{1}{\sqrt{\frac{1}{\pi}-\frac{1}{4}}}\left(\frac{1}{2}-\sqrt{\frac{(1-\chi)}{\pi(1+\chi)}}\right)\right]\right\} \tag{2.80}$$

Strangely, expression (2.80) does not depend on the number of nodes $N$, but it depends only on parameter $\chi$ which is related to the distribution of the phase shifts $\Delta_i$. Clearly, the result in (2.78) is as a potential useful upper bound only in the concavity region of (2.78).

Figure 2.27 depicts the position of the asymptote as a function of $\beta$, considering that the distribution of the shifts $\Delta_i$ is uniform in $[-\pi/\beta, +\pi/\beta]$. Figures 2.28, 2.29, and 2.30, represent (2.78) for different values of $N$, and $\beta$. As can be seen, the position of the asymptote (2.79) only depends on $\beta$.

In order for (2.78) to serve as an upper bound for the NRSS for R1BF, two conditions must be verified:

- *Condition* $\mathcal{C}.1$: The function $\mathcal{F}(\xi)$ has to be greater than the expression of the first increment expressed in (2.66), hence, the following must hold:

$$\mathcal{F}(\xi) \geq h_0(\xi) \tag{2.81}$$

  for $\xi \in [1/\sqrt{N}, 1]$, which is the range of interest for the NRSS.

- *Condition* $\mathcal{C}.2$: Since the function $\mathcal{Y}(t)$, in the range $[0, t_1)$, goes from being concave to convex, in its concavity region it must be more concave than the NRSS curve for R1BF, obtained from (2.51). This can be proven by showing that with the random synchronization, the time to achieve the value of NRSS corresponding to $\mathcal{Y}(t_s)$, which is $\mathcal{Y}(t)$ calculated in its saddle point $t_s$, i.e., the point in time where from concave it becomes convex, is greater than $t_s$.

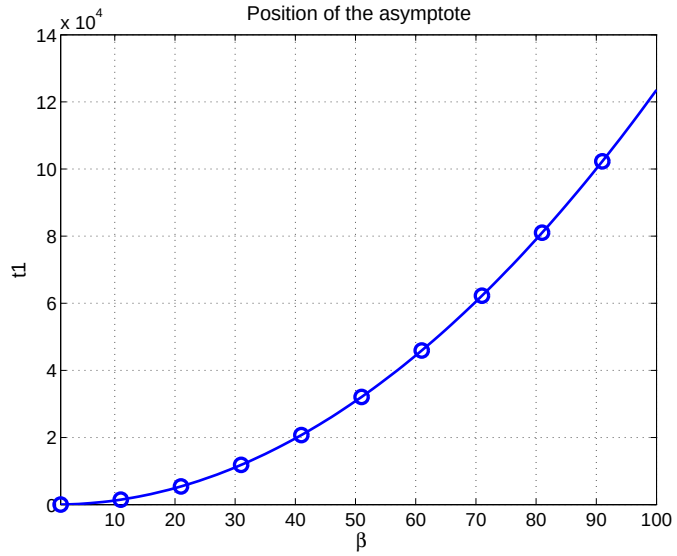


Figure 2.27: Position of the asymptote (2.79) as a function of $\beta$.

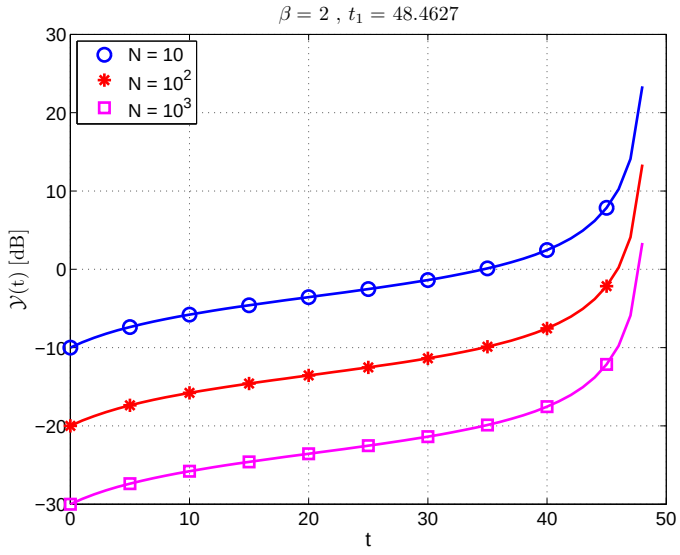


Figure 2.28: Expression (2.78) for different values of $N$, and for $\beta = 2$. As can be seen, $t_1$, shown in (2.79), does not change with $N$.

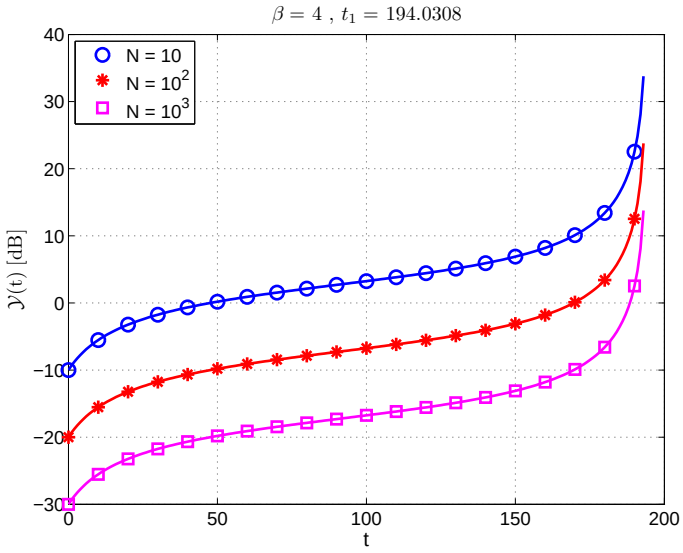


Figure 2.29: Expression (2.78) for different values of $N$, and for $\beta = 4$. As can be seen, $t_1$, shown in (2.79), does not change with $N$.

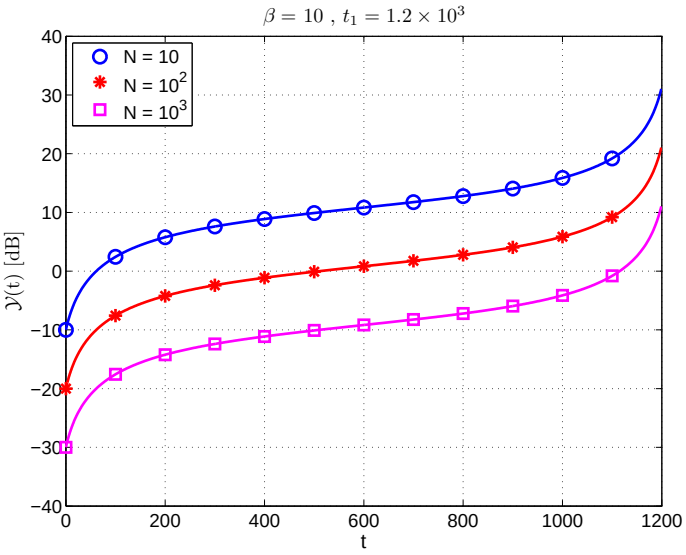


Figure 2.30: Expression (2.78) for different values of $N$, and for $\beta = 10$. As can be seen, $t_1$, shown in (2.79), does not change with $N$.

### Verification of Condition $\mathcal{C}.1$

First of all, we can notice that $\mathcal{F}(\xi)$ and $h_0(\xi)$ are equal for $\xi = 0$:

$$\mathcal{F}(0) = \frac{p}{\sqrt{2\pi}} \tag{2.82}$$

$$h_0(0) = \frac{p}{\sqrt{2\pi}} \tag{2.83}$$

Also, by observing the first derivatives:

$$\frac{d}{d\xi}h_0(\xi) = -\frac{q}{2}\text{Erfc}\left[\frac{q}{\sqrt{2}\pi}\xi\right] \tag{2.84}$$

$$\frac{d}{d\xi}\mathcal{F}(\xi) = -\frac{q}{2} + \frac{q^2}{p\sqrt{2\pi}}\xi \tag{2.85}$$

we can see that, for $\xi = 0$, they are both equal to $-\frac{q}{2}$. We here use the Erfc function instead of the $\mathcal{Q}$ function for simplicity of calculation. In any case, the Erfc and the $\mathcal{Q}$ function comply to the following relation: $\text{Erfc}(x) = 2\mathcal{Q}(\sqrt{2}x)$, so their use is equivalent. As can be seen, (2.84) is always negative, since the argument of the Erfc function is always positive, and there is a minus in front of it. On the other hand, (2.85) is always increasing and it becomes positive for $\xi \geq \sqrt{\frac{\pi}{2}}\frac{p}{q}$. Also, if we look at the second derivatives:

$$\frac{d^2}{d\xi^2}h_0(\xi) = \frac{q^2}{p\sqrt{2\pi}}e^{-\frac{q^2}{2p^2}\xi^2} \tag{2.86}$$

$$\frac{d^2}{d\xi^2}\mathcal{F}(\xi) = \frac{q^2}{p\sqrt{2\pi}} \tag{2.87}$$

we can see that, in this case also, they are both equal to $\frac{q^2}{p\sqrt{2\pi}}$ for $\xi = 0$. We can then see how (2.86) is always decreasing, whereas (2.87) is a constant. We can thus state that, at least in the range of interest, which is for $y_0 \leq \xi \leq 1$, $\mathcal{F}(\xi) > h_0(\xi)$, whereas for $0 \leq \xi \leq 1$, $\mathcal{F}(\xi) \geq h_0(\xi)$. These results are also shown in Figures 2.31, 2.32, 2.33.

### Verification of Condition $\mathcal{C}.2$

In [1] an upper bound is calculated for the convergence time. More precisely, an upper bound for the time to achieve a certain value of normalized NRSS is provided. This is calculated by first finding a lower bound for the optimized convergence rate (i.e. the increment (2.52), which depends on the NRSS and on the optimized variance of the phase shifts). Differently, we need an upper bound for the convergence rate, to use this result to lower bound the time to achieve a certain value of NRSS, by

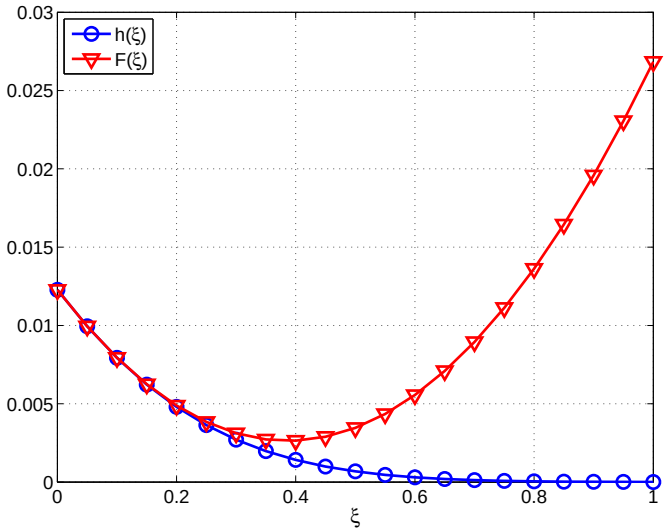


Figure 2.31: Comparison between (2.68) and (2.66).

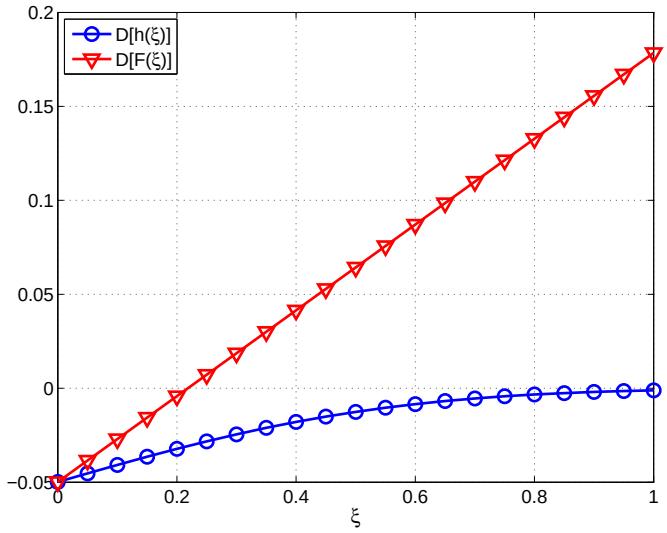


Figure 2.32: Comparison between the first derivatives of (2.68) and (2.66).

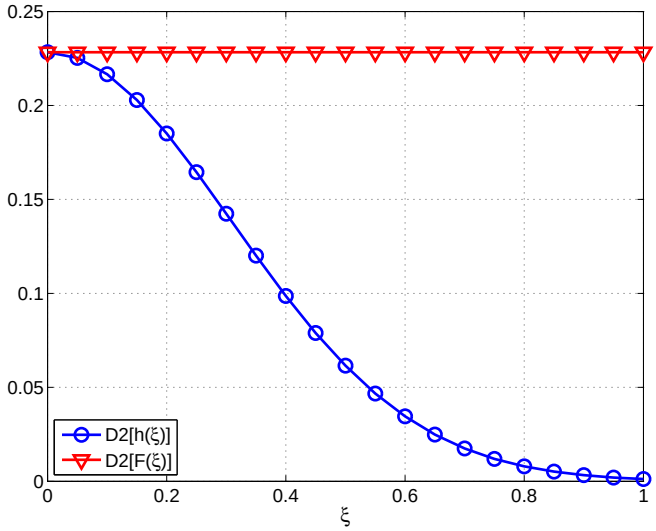


Figure 2.33: Comparison between the second derivatives of (2.68) and (2.66).

following the same steps as in [1]. Unfortunately, the upper bound we derived in (2.81), does not satisfy one requirement, needed to complete this proof. In order to upper bound the convergence rate, in fact, we need an upper bound for the convergence rate which is monotone decreasing, in order to be able to use a modified version of the proof of Theorem 3 in [1], which is based on the inverse function theorem. The analytical verification of this condition remains an open problem.

### NRSS Upper Bound for R1BF

As can be seen, considering the range $[0, t_1)$, where, as stated above, $t_1$ is the position of the first asymptote, the tangent function in expression (2.78) is zero for $t = t_0$, where:

$$t_0 = \frac{2\text{Arctan}\left(\frac{1}{\sqrt{\frac{1}{\pi}-\frac{1}{4}}}\left(\frac{1}{2}-\sqrt{\frac{1-\chi}{\pi(1+\chi)}}\right)\right)}{\sqrt{\frac{1}{\pi}-\frac{1}{4}(1-\chi)}} \tag{2.88}$$

is the time instant relative to the saddle point of (2.78). The first derivative of (2.78) is:

$$\begin{aligned}\mathcal{Y}'(t) =& \frac{1}{2}\left(\frac{1}{\pi}-\frac{1}{4}\right)\sqrt{\frac{\pi(1+\chi)}{N(1-\chi)}}(1-\chi)\text{Sec}^2\left[\sqrt{\frac{1}{\pi}-\frac{1}{4}}\frac{(1-\chi)}{2}t\right.\\ &\left.-\text{Arctan}\left(\frac{1}{\sqrt{\frac{1}{\pi}-\frac{1}{4}}}\left(\frac{1}{2}-\sqrt{\frac{1-\chi}{\pi(1+\chi)}}\right)\right)\right].\end{aligned} \tag{2.89}$$

The value of (2.89) in $t_0$ is the following:

$$\mathcal{Y}'(t_0) = \frac{1}{2}\left(\frac{1}{\pi} - \frac{1}{4}\right)\sqrt{\frac{\pi}{N}(1-\chi^2)} \tag{2.90}$$

since $\mathrm{Sec}^2(t_0) = 1$.

If condition $\mathcal{C}.2$ is verified (and we here conjecture that it is) the following straight line:

$$s(t) = \sqrt{\frac{\pi(1+\chi)}{4N(1-\chi)}} + \left(\frac{1}{2}\left(\frac{1}{\pi} - \frac{1}{4}\right)\sqrt{\frac{\pi}{N}(1-\chi^2)}\right)(t - t_0) \tag{2.91}$$

is an upper bound for the NRSS obtained with the recursive expression (2.51) for R1BF, when $t \geq t_0$. In order to cover a time frame which goes from $t = 0$ to, potentially, infinity, we define $U(t)$ as follows:

$$U(t) \triangleq \begin{cases} \mathcal{Y}(t), & 0 < t \leq t_0 \\ s(t), & t_0 < t < \infty \end{cases} \tag{2.92}$$

which upper bounds the recursive expression (2.51).

### Results

The series of graphs depicted in Figures 2.34- 2.39 represents:

- The NRSS for SDDB with $K = 2$, according to (2.20) (black line, with triangular markers)[2].
- The NRSS for R1BF obtained with the recursion (2.51) (red line, with circular markers, except for Figures 2.37 and 2.39 in which it is represented by a red line only).
- The upper bound derived in (2.92) (blue line, with square markers).

These plots are obtained with different values of $N$, precisely 10, $10^2$, and $10^3$, and different values of $\beta$, namely 2 and 20.

The following observations are in order:

$\mathcal{O}.1$ For a given value of $N$, the tightness of the bound increases as $\beta$ increases, i.e., as the variance of the distribution of the random shifts $f_\Delta(\cdot)$ decreases.

[2] As in Figure 2.19, the NRSS is represented as a function of the number of activated and synchronized devices, $N_\mathrm{s}[m]$, as given in (2.4). The plot can also be interpreted as a function of time, since nodes are synchronized successively (one per time slot) and thus the curves indicate the NRSS that would be attained by the activated nodes after a certain number of rounds.

$\mathcal{O}.2$ For a given value of $\beta$, i.e., for a given variance for $f_\Delta(\cdot)$, the tightness of the bound decreases as $N$ increases.

$\mathcal{O}.3$ The bound in (2.92) is useful when the following condition is verified:

$$\frac{K}{\pi}\sin\left(\frac{\pi}{K}\right) > U(N). \tag{2.93}$$

The left hand side of (2.93) is the lower bound of the NRSS achieved with SDDB with a given resolution $K$, at the $N$-th step of the algorithm. The right hand side of (2.93) is the upper bound for the NRSS achieved with R1BF after $N$ time slots. As a consequence, the gain $\mathcal{G}$ in dB in terms of NRSS achievable with SDDB with respect to R1BF after $N$ time slots is simply:

$$\mathcal{G} = 20\log_{10}\left(\frac{K}{\pi}\sin\left(\frac{\pi}{K}\right)\right) - 20\log_{10}\left(U(N)\right) \tag{2.94}$$

Clearly, the tighter the NRSS bound for R1BF is (we have already shown in Section 2.9.1 that the lower bound for SDDB is tight), the more accurate the expression of the gain is. Figures 2.40, 2.41, and 2.42 represent $\mathcal{G}$ in dB as $N$ varies. As can be seen from the graphs, for very large networks of nodes, the bound looses its tightness, and the gain becomes negative.

$\mathcal{O}.4$ In [1], authors derive a model to optimize the variance of $f_\Delta(\cdot)$ in order to maximize the NRSS increase at each step. The value of the variance of $f_\Delta(\cdot)$ depends on the NRSS, and it changes at each step of the algorithm. It can be seen how the variance decreases as the algorithm unfolds, and, for example, for $N = 10$, $\beta > 10$ after 90 iterations, and for $N = 10^2$ and $10^3$, $\beta > 10$ after 200 iterations. Hence, having to choose a fixed value for $\beta$, since, in practical cases, this parameter is not tunable, unless full feedback is available, it is better to choose a value of $\beta$ which ensures convergence to a larger value of NRSS, instead of selecting a value which allows for a rapid initial increase of the NRSS, but a very slow convergence rate in the later stages of the algorithm. This can also be noticed by observing Figure 2.18.

We can thus conclude that, for useful values of $\beta$ for a fixed-variance R1BF approach, and for reasonable network sizes, i.e. with $N$ in the order of hundreds of nodes, the bound (2.92) is useful, and the gain obtained by using SDDB with respect to R1BF is quantifiable with (2.94).

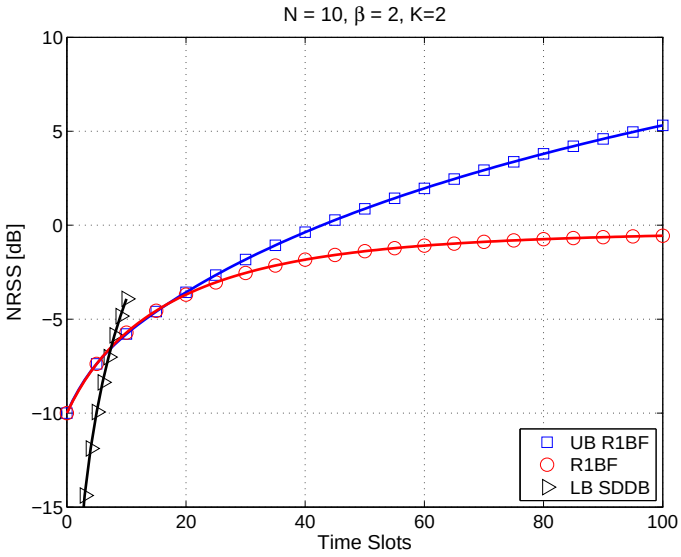


Figure 2.34: The upper bound (2.92) is compared to the recursion (2.51) and to the NRSS for SDDB with $K = 2$ obtained through (2.20); $N = 10$, $\beta = 2$.

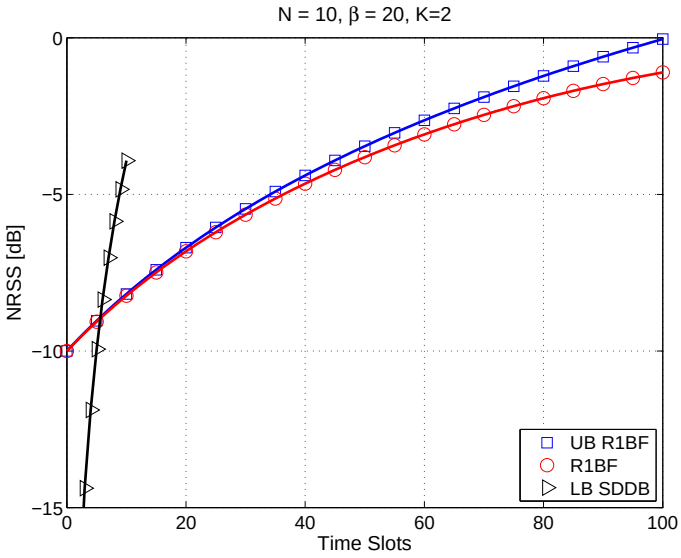


Figure 2.35: The upper bound (2.92) is compared to the recursion (2.51) and to the NRSS for SDDB with $K = 2$ obtained through (2.20); $N = 10$, $\beta = 20$.

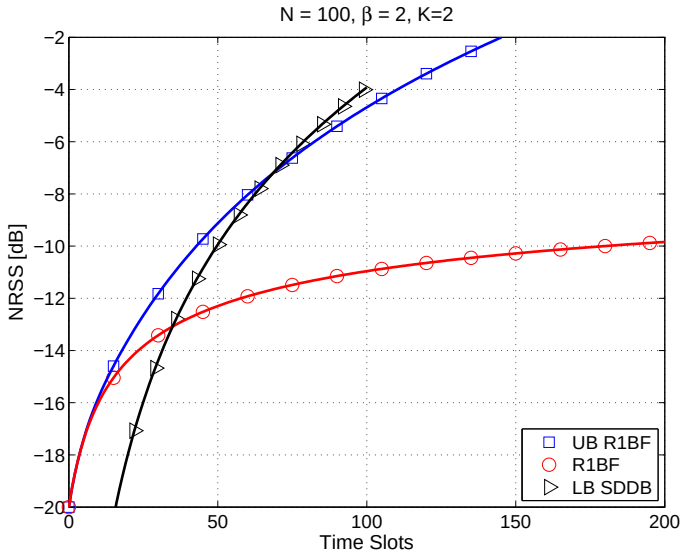


Figure 2.36: The upper bound (2.92) is compared to the recursion (2.51) and to the NRSS for SDDB with $K = 2$ obtained through (2.20); $N = 100$, $\beta = 2$.

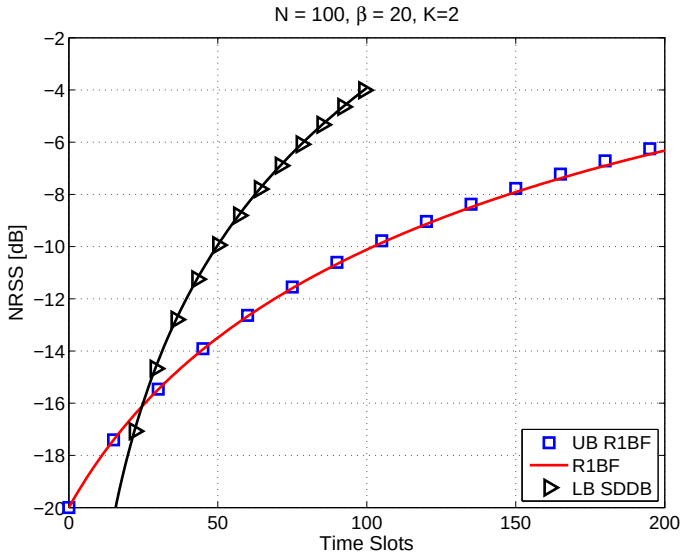


Figure 2.37: The upper bound (2.92) is compared to the recursion (2.51) and to the NRSS for SDDB with $K = 2$ obtained through (2.20); $N = 100$, $\beta = 20$.

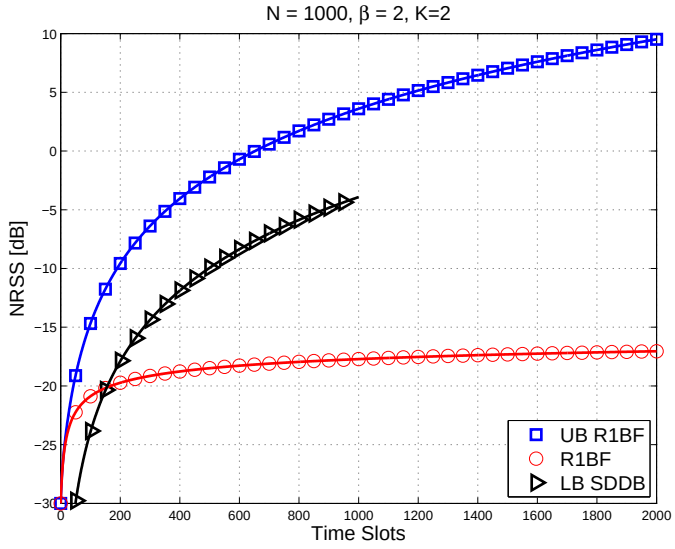


Figure 2.38: The upper bound (2.92) is compared to the recursion (2.51) and to the NRSS for SDDB with $K = 2$ obtained through (2.20); $N = 1000$, $\beta = 2$.

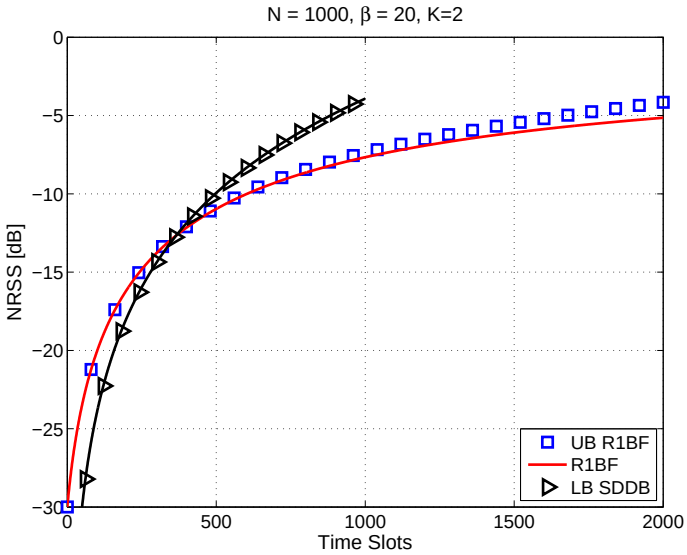


Figure 2.39: The upper bound (2.92) is compared to the recursion (2.51) and to the NRSS for SDDB with $K = 2$ obtained through (2.20); $N = 1000$, $\beta = 20$.

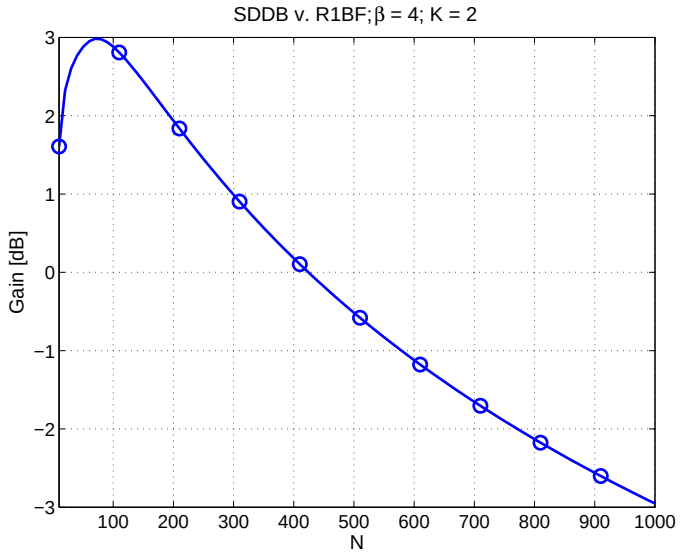


Figure 2.40: Gain obtained by using SDDB with $K = 2$ with respect to R1BF with $\beta = 4$ at the end of the SDDB synchronization round as the network size $N$ changes.

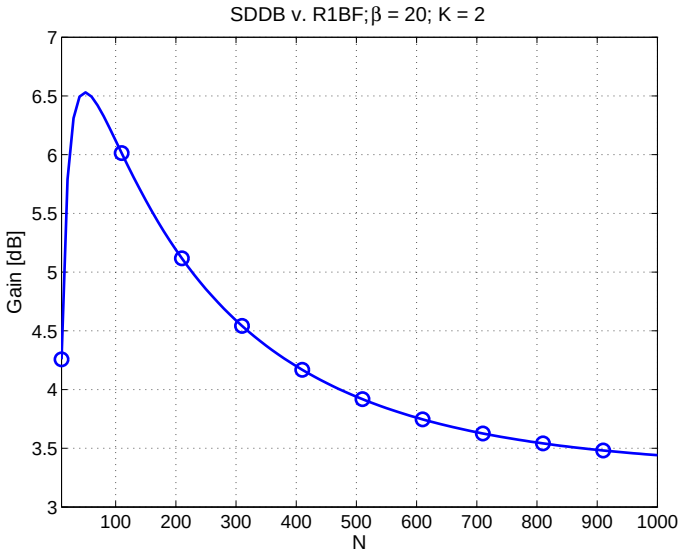


Figure 2.41: Gain obtained by using SDDB with $K = 2$ with respect to R1BF with $\beta = 20$ at the end of the SDDB synchronization round as the network size $N$ changes.

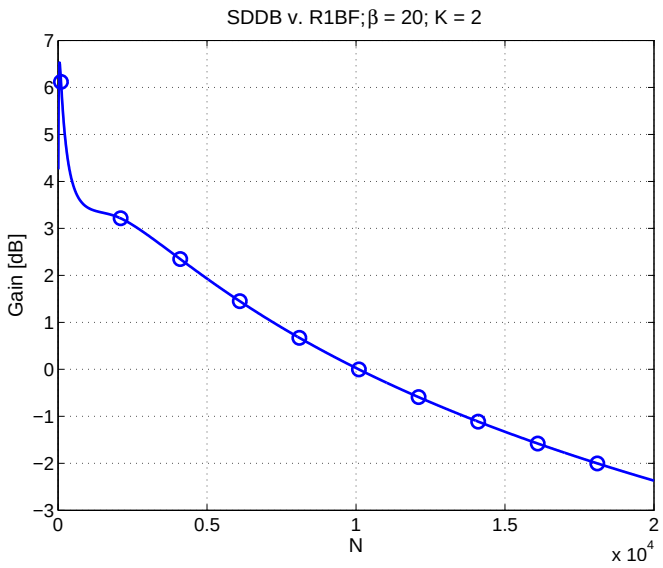


Figure 2.42: Gain obtained by using SDDB with $K = 2$ with respect to R1BF with $\beta = 4$ at the end of the SDDB synchronization round as the network size $N$ changes.

# Chapter 3

# Conclusion for Part I

Part I of this thesis has tackled the problem of phase synchronization for a network of distributed sensors that have to cooperatively emulate a large antenna array to steer a maximum of radiation towards the receiver. New closed-loop algorithms, identified as DJA and SDDB, and based on deterministic local phase adjustments driven by quantized feedback from the receiver, have been presented and have been shown to have better convergence performance with respect to the random solution proposed in [1], which we considered as benchmark.

DJA entails joint and repeated transmissions of synchronization pilots from all the nodes in the network, and nodes, in turn, perform phase tests by locally adjusting the phase of their outgoing beacon according to fixed pre-defined sets of possible phase shifts. The receiver measures the RSS relative to each phase test, and sends one bit of feedback for each test to inform the node whether the applied adjustment has improved or worsened the quality of the RSS. The time to synchronize is proportional to the number of nodes in the network, and the energy consumption due to phase alignment is proportional to $N^2$, where $N$ is the size of the network. This approach has been shown to be robust to time-varying channel drift, since the feedback is based on the state of the resultant signal at each step.

SDDB is a more energy efficient solution for phase alignment, since each node transmits only once in its assigned time slot, and the receiver sends a quantized feedback which represents the phase adjustment that the node has to apply to align its signal to a fixed bias, locally known at the receiver. The energy consumption is proportional to $N$, and the number of feedback bits depends on the available capacity on the feedback channel. It has been shown that, with only 1 bit of feedback, the achievable final gain is within 5 dB from the maximum, whereas with 2 bits of

feedback the final gain is only 1 dB away from the maximum. Analytic expressions that characterize the behavior of the NRSS as SDDB unfolds have been put forth, in the absence and presence of AWGN at the receiver and without and with flat fading. Our analysis is innovative since AWGN had never been incorporated in the model for R1BF synchronization, except for the attempt in [61]. The work in [61] though, does not quantify the gain achievable by R1BF in the presence of AWGN.

The difference between DJA and SDDB does not only consist in the amount of energy consumption required to complete a synchronization cycle. Since DJA continuously involves all the nodes in the network in the synchronization procedure, this allows for potential cooperative transmission of information during the alignment procedure itself. Moreover, the feedback is a function of the actual state of the resultant, which means that this approach is potentially more adaptive to channel and oscillator drift. The energy overhead though, could be too large. Differently, when SDDB is implemented, the synchronization stage and the cooperative transmission stage are disjoint but the gain in terms of energy overhead is highly compelling.

We have put forth an analytic expression, (2.92), which we conjecture upper bounds the NRSS dynamics for R1BF. The motivation for this was to be able to rigorously quantify the performance gain obtained by using a deterministic approach instead of the random one. The completion of the proof that expression (2.92) upper bounds (2.51) is an open problem. However, simulation results validate our claim. The bound expressed in (2.92) is useful for a wide range of shift distributions, and for network sizes which can vary from tens to hundreds of nodes.

The following points pave the way for future developments of this work:

- Evaluation of the impact of having multiple antennas at the receiver on DJA and SDDB performance.

- Evaluation of the impact of nobility of the sensors on the synchronization capabilities of DJA and SDDB.

- Design of periodic phase re-alignment procedures, specifically tailored for given statistics of oscillator dynamics, and given accuracies of frequency synchronization.

- Study of the convergence of DJA and SDDB in the presence of multiple spatial constraints, i.e., not only with the unique objective of maximizing the signal

in the direction of the receiver, but also of reducing interference in other directions, similarly to the work in [65], where the convergence of R1BF has been studied in these conditions.

# Part II

# Coarse Beamforming

# Chapter 4

# Coarse Beamforming for Multi-Beam Satellite Networks

## 4.1 Motivation for Coarse Beamforming

A key enabler for greatly enhancing throughput in next generation satellite systems is to deploy a large number of beams on the coverage area in order to take advantage of Space-Division Multiplexing (SDM), as well as Frequency- and Time- Division Multiplexing (FDM and TDM). As a consequence, the same sub-band in the same time slot can be reused across the served area since interference is, ideally, suppressed by highly directive beams. This allows for potential reuse of the whole system bandwidth on each beam cell on the coverage area.

In reality the effect of side lobes in the beam radiation patterns severely exacerbates interference, and with a view on counteracting inter-beam interference, predefined patterns for the reuse of frequencies among beams have to be employed. Conventionally, different bands are assigned to beams with adjacent footprints, as their radiation patterns partially overlap. An essential parameter for describing this circumstance is the number of colors $N_c$ in the frequency reuse pattern ($N_c \in \mathbb{N},\ N_c \geq 1$) which corresponds to the number of disjoint frequency bands used on the coverage area. However, the benefit in terms of throughput brought by a full frequency reuse pattern can be achieved by resorting to appropriate interference mitigation policies, which have proven to be promising [87], and which only come with a slight increase of complexity in terms of signal processing techniques at the gateway.

In order to achieve a multiple-beam type radiation pattern, the satellite is

equipped with a multi-fed reflector antenna, and beamforming is implemented by linearly combining feed signals with complex coefficients [88]. Different system architectures can be envisaged according to where beamforming processing is carried out. Conventional beamforming techniques, either analog or digital, that completely rely on the payload's processing potential (space beamforming) are nowadays far beyond the state of the art [89]. Yet, when beamforming is fully implemented at the ground segment (on-ground beamforming), and the number of feeds is greater than the number of users, the gateway and the satellite must engage in extensive communication efforts since they have to exchange the whole set of feed signals that have to transit from ground to space and vice-versa [90]. Although this solution may seem compelling, since it drastically reduces payload complexity, and allows to take advantage of full on-ground processing flexibility, it requires a large amount of feeder link spectral resources, since feed signals must be frequency multiplexed both on the up-link and the down-link of the feeder link. In these circumstances, an excessive bandwidth requirement could lead to the design of a costly multiple gateway infrastructure, that might be inefficient also from the point of view of interference management.

As an alternative, in order to minimize the cost of network deployment, a hybrid space/ground architecture has the potential to offer a good degree of flexibility and efficiency by foreseeing the presence of a stage where the stack of feed signals is projected on a sub-space. This reduces the cardinality of the set of signals to be exchanged between space and ground, and consequently spectral requirements on the feeder link are relaxed [89]. The concept of mapping feed signals on a sub-space was introduced in [91], and [92] describes a feed-signal selection procedure based on the location of the active users, in order to make a more efficient use of only a sub-set of feed signals out of the pool of available ones. The work in [93] describes a hybridized space/ground beamforming scheme, with the objective of reducing the amount of circuitry required to process on ground all the satellite signals. A processing scheme on the payload is envisaged to obtain a subset of signals out of the full stack of feed signals. A similar idea is described in [94]. In this thesis, as further described in Section 4.2, we turn this concept into a practical application, devising two schemes for space processing. The hybrid space/ground architecture we consider is depicted in Figure 4.1, and it foresees the presence of a fixed processing scheme to be implemented on board the payload. Since this space processing is non adaptive, it keeps payload complexity affordable. We refer to this

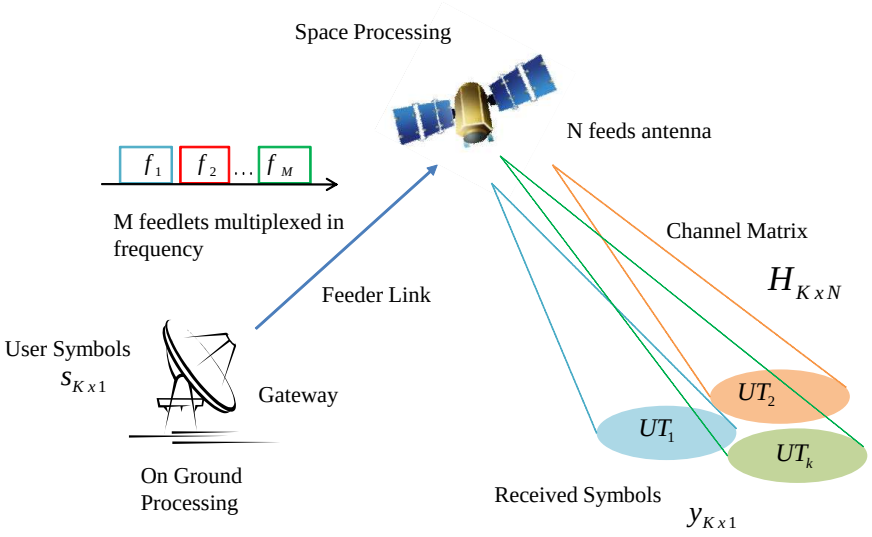


Figure 4.1: Hybrid Space/Ground Processing Architecture

fixed on-board processing as Coarse Beamforming (CB).

## 4.2 The Hybrid Architecture

We focus on a hybrid space/ground architecture with a view on evaluating the impact of Coarse Beamforming implementation in the forward link of a broad-band multi-beam satellite network in terms of system performance. The following points summarize the contribution of this thesis:

1) Two different Coarse Beamforming techniques are proposed, based on Discrete Fourier Transform (DFT) and Principal Component Analysis (PCA), respectively.

2) A preliminary analysis is conducted to measure feed signal degradation as a consequence of compression both in case of an ideal analog and digital feeder link.

3) The analysis is extended to the gateway to User Terminals (UTs) link, a joint precoding and Coarse Beamforming implementation scheme is considered, and its impact on system spectral efficiency and availability is evaluated when the feeder link is analog and ideal.

Point (2) has been an important stepping stone whose promising results have led to developing the full system analysis mentioned in point (2). In our preliminary and

simpler set up, which is described in Chapter 5, we consider the gateway to satellite link, i.e. the feeder link. Ground processing consists in fixed beamforming and feed signal compaction. As a consequence of this processing, a set of intermediate signals, which we refer to as feedlets and whose cardinality is smaller than the number of antenna feeds, has to be forwarded to the space segment. Once the satellite receives the feedlets, it reconstructs feed signals with a fixed processing matrix. The block diagram in Figure 4.2 represents this scheme. For this scenario we measure the level of mismatch between the on-board reconstructed feed signals and the original set (obtained when no dimension reduction of the space takes place) as a function of the number of feedlets. We consider both analog and digital feeder link cases. Clearly, in case of digital feeder link, the mismatch is also a function of the adopted quantization strategy. Sections 5.2 and 5.3 consider the cases where compression is based on PCA and DFT, respectively.

Since the results deriving from this study are promising, in Chapter 6 we extend the analysis to the full gateway to UTs link. In this scenario ground processing consists in an adaptive precoding technique to mitigate interference among users and to allow for the use of a full color frequency reuse scheme and Coarse Beamforming is implemented on board to produce feed signals. In order to restrain payload complexity, this on-board processing scheme has to be fixed and non-channel-adaptive. By taking into account the fixed space processing scheme, the precoder produces a set of feedlets, whose cardinality depends on the dimensions of the on-board Coarse Beamforming matrix. Once signals are sent to the satellite, the Coarse Beamforming matrix is then used for feed signal reconstruction. This scheme is represented with a block diagram in Figure 4.3. Section 6.3 considers PCA- and DFT-based Coarse Beamforming, respectively, for the full scenario case. Spectral efficiency and availability are the metrics used to evaluate system performance as functions of the cardinality of the feedlet set.

The parameters relative to this system were kindly provided by the European Space Agency (ESA) in the framework of a study on next-generation broad-band satellite systems [95–97].

*Notation*: Boldface upper case letters denote matrices and boldface lower case letters refer to column vectors. We denote by $(\cdot)^H$ the Hermitian transpose. The $N \times N$ identity matrix is denoted by $\mathbf{I}_N$. We use the notation $\mathcal{Q}(\cdot)$ to denote the quantized version of a vector. The symbol $\mathbf{0}_N$ denotes a column vector of $N$ zero elements, and the symbol $\mathbf{0}_{N\times M}$ denotes an $N \times M$ matrix of zero elements.

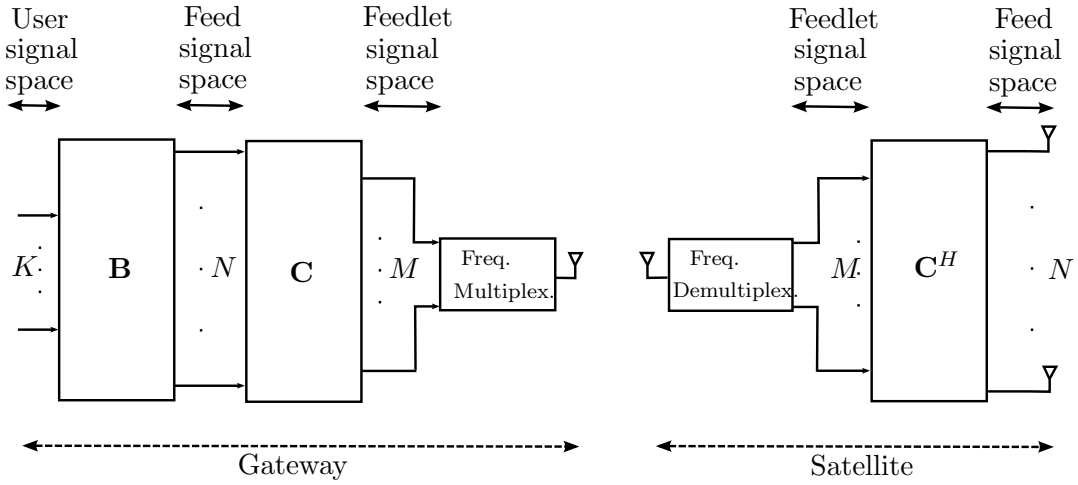


Figure 4.2: Block diagram for the feed signal compression scheme when the feeder link is analog

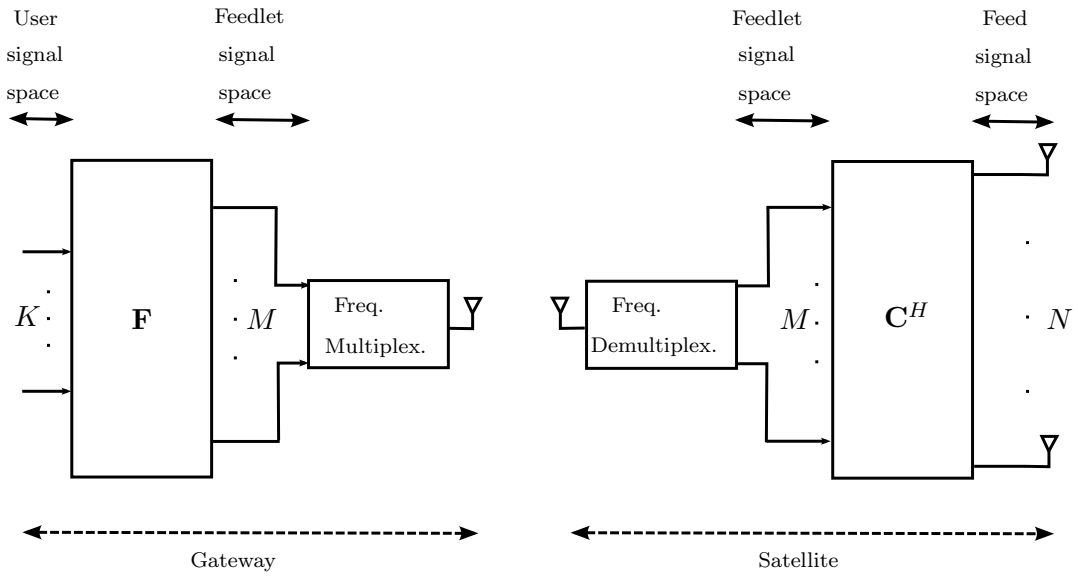


Figure 4.3: Block diagram representing the hybrid space/ground architecture with adaptive precoding implemented at the gateway and Coarse Beamforming implemented on board the satellite

# Chapter 5

# Preliminary Study of Two Coarse Beamforming Techniques

We now evaluate the impact of compression on reconstructed feed signals in the forward link of a multi-beam satellite system by means of a mismatch measure that we denote as Signal to Distortion Noise Ratio (SDNR). This figure of merit evaluates reconstructed feed signal degradation as a consequence of dimension reduction of the feedlet sub-space. We analyze two compression techniques based on DFT and PCA, respectively. The idea that underlies this approach is that the number of feeds exceeds the number of users, and plus adjacent feed radiation patterns partially overlap. As a consequence, the relevant information can be packed more efficiently and represented by fewer coefficients in an appropriate representation domain. As a result of ground processing, the gateway forwards to the satellite a number of feedlets which is smaller than the number of antenna elements. If no processing took place on board, i.e. if the satellite were just a transparent forwarding unit, the whole stack of feed signals would have to be multiplexed and transmitted on the feeder link from the gateway to the space segment. Instead, the dimension of the subspace on which feed signals are projected corresponds to the number of signals to be frequency multiplexed on the feeder link. The smaller this dimension, the greater the gain in terms of bandwidth compaction, but the lower the SDNR will be. A trade off must then be sought between compaction gain and acceptable SDNR level. We assume that the feeder link is perfectly calibrated and noiseless [1].

[1] Quantification of performance loss when this assumption is violated is material for future development of this study.

## 5.1 System Model

We assume TDM, FDM and SDM in the user link such that at a given time slot, for a given frequency sub-band, the gateway is simultaneously serving a set of users whose cardinality depends on the adopted frequency reuse (FR) factor and on the number of beam cells. We focus on the forward link, and we assume that the coverage area is divided in $K$ beam cells, thus the number of served users per carrier amounts to $K/N_{\mathrm{c}}$. The multi-fed reflector on board the satellite is equipped with $N$ antenna elements, with $N > K$, and feed signals are obtained through linear combinations of the user signals. A pictorial representation of this scenario can be observed in Figure 4.1. We consider both the analog and the digital scenario: when the feeder link is digital, feedlets must be quantized so that they can be coded with digital streams of data. We consider uniform quantization of the real part and imaginary part of each of the signals with three different values for the number of quantization levels ( $2^4$, $2^8$, $2^{16}$). The $N \times 1$ vector of feed signals $\mathbf{x}$ can be written as follows:

$$\mathbf{x} = \mathbf{B}\mathbf{s} \tag{5.1}$$

where $\mathbf{s}$ is the $K \times 1$ vector of the complex user signals modeled so that the following expressions hold:

$$\mathbb{E}[\mathbf{s}] = \mathbf{0}_K \tag{5.2}$$

$$\mathbb{E}[\mathbf{s}\mathbf{s}^H] = \mathbf{I}_K \tag{5.3}$$

and $\mathbf{B}$ is a fixed beamforming matrix of dimension $N \times K$, provided in [98]. The following expressions define the $M \times 1$ vectors of feedlet signals for the analog and the digital cases, respectively:

$$\mathbf{f}_{\mathrm{a}} = \mathbf{C}\mathbf{x} \tag{5.4}$$

$$\mathbf{f}_{\mathrm{q}} = \mathcal{Q}(\mathbf{C}\mathbf{x}) \tag{5.5}$$

where $\mathbf{C}$ is an $M \times N$ matrix with $M \leq N$ which implements on-ground compression and it is designed according to the chosen compaction strategy. Subscripts $a$ and $q$ denote the fact that we are considering the analog case and the digital case, respectively. In the analog case, elements in $\mathbf{f}_{\mathrm{a}}$ are exactly the outputs of $\mathbf{C}\mathbf{x}$ computation. In the digital case, the real part and the imaginary part of the feedlet signals are uniformly quantized, i.e. the dynamics of the signals are divided into intervals. Each interval has an assigned value, and all the signals that fall into that interval are mapped on the same value. Vector $\mathbf{f}_{\mathrm{q}}$ represents this mapping.

By multiplexing a number $M < N$ of signals on the feeder link, bandwidth compaction is achieved. In order to assess the effect of this bandwidth compaction on the feed signals, we define a figure of merit called SDNR to measure the mismatch between the vector of feed signals and the vector of on-board reconstructed feed signals of dimensions $N \times 1$, obtained by applying the following transform to the feedlets:

$$\hat{\mathbf{x}}_{\mathrm{a}} = \mathbf{C}^H \mathbf{f}_{\mathrm{a}} \tag{5.6}$$

$$\hat{\mathbf{x}}_{\mathrm{q}} = \mathbf{C}^H \mathbf{f}_{\mathrm{q}} \tag{5.7}$$

where $\mathbf{C}^H$ is of dimensions $N \times M$, and it is used to undo compaction. This results in $\hat{\mathbf{x}}_{\mathrm{a}}$ and $\hat{\mathbf{x}}_{\mathrm{q}}$ which are the reconstructed feed signals for the analog and the digital cases, respectively. Evidently SDNR is a function of $M$, and also of the quantization strategy in the digital case, and we define it as:

$$\mathrm{SDNR}_{\mathrm{a}} = \frac{\mathbb{E}[|\mathbf{x}|^2]}{\mathbb{E}[|\mathbf{x} - \hat{\mathbf{x}}_{\mathrm{a}}|^2]} \tag{5.8}$$

$$\mathrm{SDNR}_{\mathrm{q}} = \frac{\mathbb{E}[|\mathbf{x}|^2]}{\mathbb{E}[|\mathbf{x} - \hat{\mathbf{x}}_{\mathrm{q}}|^2]} \tag{5.9}$$

Clearly in these conditions, if $\mathbf{C}$ were of dimensions $N \times N$, and if it satisfied the condition $\mathbf{C}\mathbf{C}^H = \mathbf{I}_N$, reconstruction would be perfect for the analog case. A degree of mismatch would still be present in the digital case because of the effect of quantization.

## 5.2 PCA-based Compression

Since the Karhunen-Loève transform (KLT) has good energy compacting properties, we have chosen this approach for compression. More specifically, we call $\mathbf{Z}$ the $N \times N$ covariance matrix of the feed signals, defined as follows:

$$\mathbf{Z} = \mathbb{E}[(\mathbf{x} - \mathbb{E}[\mathbf{x}])(\mathbf{x} - \mathbb{E}[\mathbf{x}])^H] \tag{5.10}$$

It is easy to see that $\mathbf{Z}$, in this setting, is equal to $\mathbf{B}\mathbf{B}^H$. In fact:

$$\mathbf{Z} = \mathbb{E}[(\mathbf{B}\mathbf{s} - \mathbb{E}[\mathbf{B}\mathbf{s}])(\mathbf{B}\mathbf{s} - \mathbb{E}[\mathbf{B}\mathbf{s}])^H] \tag{5.11}$$

$$= \mathbf{B}\mathbf{B}^H \tag{5.12}$$

where (5.1) has been used, and (5.2) and (5.3) have been taken into account. Also $\mathbb{E}[\mathbf{B}] = \mathbf{B}$ since $\mathbf{B}$ is deterministic. The following decomposition holds [99]:

$$\mathbf{Z} = \mathbf{A}\mathbf{L}\mathbf{A}^H \tag{5.13}$$

where $\mathbf{A}$ is an $N \times N$ matrix whose columns are the $N$ eigenvectors of $\mathbf{Z}$, and $\mathbf{L}$ is an $N \times N$ diagonal matrix whose diagonal elements are the eigenvalues of $\mathbf{Z}$. We design compression using a subset of $M$ eigenvectors as a basis for the subspace on which feed signals are projected. We call $\mathbf{C}_{\text{klt}}$ the $M \times N$ compression matrix, and we build it as:

$$\mathbf{C}_{\text{klt}} = \mathbf{A}_M^H \tag{5.14}$$

where the expression $\mathbf{A}_M$ denotes a subset of $M$ columns of $\mathbf{A}$. The way this subset is chosen is further explained in Section 5.4. As a consequence, the $M \times 1$ vectors of feedlet signals for the analog and the digital cases respectively, in case of KLT-based compression, have the following expressions:

$$\mathbf{f}_{\text{a,klt}} = \mathbf{C}_{\text{klt}}\mathbf{x} = \mathbf{C}_{\text{klt}}\mathbf{B}\mathbf{s} \tag{5.15}$$

$$\mathbf{f}_{\text{q,klt}} = \mathcal{Q}(\mathbf{C}_{\text{klt}}\mathbf{x}) = \mathcal{Q}(\mathbf{C}_{\text{klt}}\mathbf{B}\mathbf{s}) \tag{5.16}$$

The following expressions account for the on-board reconstructed feed signals in case of KLT-based compression:

$$\hat{\mathbf{x}}_{\text{a,klt}} = \mathbf{C}_{\text{klt}}^H \, \mathbf{f}_{\text{a,klt}} \tag{5.17}$$

$$\hat{\mathbf{x}}_{\text{q,klt}} = \mathbf{C}_{\text{klt}}^H \, \mathbf{f}_{\text{q,klt}} \tag{5.18}$$

where $\hat{\mathbf{x}}_{\text{a,klt}}$ and $\hat{\mathbf{x}}_{\text{q,klt}}$ represent the $N \times 1$ vectors of reconstructed feed signals for the analog and the digital case respectively.

## 5.3 DFT-based Compression

Compression based on DFT transform foresees the use of the discrete Fourier basis to build the matrix $\mathbf{C}$. We denote as $\mathbf{D}$ the $N \times N$ DFT basis. Element $(m, j)$ of matrix $\mathbf{D}$ can be written as follows:

$$\mathbf{D}_{(m,j)} = \frac{1}{\sqrt{N}} e^{\frac{2\pi i}{N}(j-1)(m-1)} \tag{5.19}$$

where $e^{\frac{2\pi i}{N}}$ is an $N$-th root of unity. We design the $M \times N$ compression matrix $\mathbf{C}$ as follows:

$$\mathbf{C}_{\text{dft}} = \mathbf{D}_M \tag{5.20}$$

where $\mathbf{D}_M$ is a subset of $M$ rows of $\mathbf{D}$. The compression is implemented as follows:

$$\mathbf{f}_{\text{a,dft}} = \mathbf{C}_{\text{dft}}\mathbf{x} = \mathbf{C}_{\text{dft}}\mathbf{B}\mathbf{s} \tag{5.21}$$

$$\mathbf{f}_{\text{q,dft}} = \mathcal{Q}(\mathbf{C}_{\text{dft}}\mathbf{x}) = \mathcal{Q}(\mathbf{C}_{\text{dft}}\mathbf{B}\mathbf{s}) \tag{5.22}$$

where (5.21) and (5.22) are the expressions for the feedlets in the analog and digital cases, respectively.

More specifically, the $m$-th feedlet has the following expression for, respectively, the analog and digital cases:

$$f_{\mathrm{a,dft},m} = \frac{1}{\sqrt{N}} \sum_{j=1}^{N} x_j e^{\frac{2\pi i}{N}(j-1)(m-1)} \tag{5.23}$$

$$f_{\mathrm{q,dft},m} = \mathcal{Q}\left( \frac{1}{\sqrt{N}} \sum_{j=1}^{N} x_j e^{\frac{2\pi i}{N}(j-1)(m-1)} \right) \tag{5.24}$$

The reconstructed feed signals are:

$$\hat{\mathbf{x}}_{\mathrm{a,dft}} = \mathbf{C}_{\mathrm{dft}}^{H}\, \mathbf{f}_{\mathrm{a,dft}} \tag{5.25}$$

$$\hat{\mathbf{x}}_{\mathrm{q,dft}} = \mathbf{C}_{\mathrm{dft}}^{H}\, \mathbf{f}_{\mathrm{q,dft}} \tag{5.26}$$

where $\hat{\mathbf{x}}_{\mathrm{a,dft}}$ and $\hat{\mathbf{x}}_{\mathrm{q,dft}}$ represent the $N \times 1$ vectors of reconstructed feed signals for the analog and the digital case, respectively, for the DFT-based compression.

## 5.4 Choice of the Basis for the Subspace

The design of the compression matrix $\mathbf{C}$ consists in truncating the KLT basis or the DFT basis, yielding (5.14) and (5.20), in order to obtain a subset of $M < N$ vectors to span a subspace on which feed signals are projected. Considering a subset of vectors out of $\mathbf{A}$ and $\mathbf{D}$ corresponds to neglecting some chosen dimensions in the spaces spanned by these two matrices. In order to maximize the SDNR, it is desirable to discard those dimensions along which feed signals have the smallest possible degree of variation, i.e., those vectors corresponding to the feedlets with smallest magnitude. We refer to this method as *sorting*. Another approach is to blindly keep the first $M$ vectors of the given basis, and discard the rest. We refer to this method as *non sorting*. The latter does not maximize the SDNR for a given $M$, but it minimizes the complexity of the signal compaction stage. In fact, if $\mathbf{C}$ is adaptive, this means that $\mathbf{C}^H$ also has to follow the variations of $\mathbf{C}$ in terms of which basis vectors have been used, and this increases the complexity of the payload, and of the signaling between gateway and satellite.

## 5.5 Comparison between PCA- and DFT-based Compression

In this section we compare performance in terms of SDNR as a function of the Compaction Ratio (CR) which we define as follows:

$$\mathrm{CR} = \frac{N - M}{N} \tag{5.27}$$

CR ranges from 0 (no compaction, i.e. $M = N$) to 1 (full compaction, i.e. $M = 0$). Figures 5.1 and 5.2 represent a comparison between analog and digital cases, for DFT- and KLT-based compression, respectively. The compression matrices are obtained according the sorting criterion, i.e. the vectors corresponding to the less important coefficients in terms of magnitude were the first ones to be discarded. These are those dimensions that carry the least amount of information. Three different uniform quantization strategies have been considered for the digital case with $2^4$, $2^8$, $2^{16}$ quantization levels respectively for both the real and the imaginary part of the complex feedlet signals. It can be seen how, for the same value of CR, the SDNR improves as the number of quantization levels rises. Clearly the analog case yields the best performance in terms of SDNR for a specific value of compaction ratio. Figures 5.3 and 5.4 represent a cross comparison between the two techniques. KLT and DFT are compared in both the analog and digital cases. It can be seen how, for the analog case, for a given value of CR, the KLT performs much better in terms of SDNR with respect to the DFT. This is not surprising, since KLT provides a basis whose vectors represent those dimensions along which the observed signal admits most of its variation. It is in fact naturally designed to yield a basis that naturally captures most of the necessary information along few useful dimensions. The DFT basis instead, is a fixed basis whose advantage consists in the fact that there is no need for a calibration or initialization stage where the statistics of the feed signals have to be acquired to create the compression matrix. In the digital case, for $2^{16}$ quantization levels, KLT still greatly outperforms DFT. But as the number of quantization levels decreases the performance gap reduces. The SDNR for the KLT, for low values or CR, has an apparently peculiar behavior (completely flat up to $CR = 35\%$), although it can be easily justified by observing the structure of $\mathbf{Z}$, which is shown in (5.11) and (5.12). In fact, the Singular Value Decomposition (SVD) of the beamforming matrix $\mathbf{B}$ is:

$$\mathbf{B} = \mathbf{RTW}^H \tag{5.28}$$

where $\mathbf{R}$ and $\mathbf{W}$ are unitary matrices of dimensions $N \times N$, and $K \times K$ respectively. The columns of $\mathbf{R}$ and $\mathbf{W}$ are the left and the right *singular vectors* respectively. The columns of $\mathbf{R}$ and $\mathbf{W}$ are orthonormal, meaning that $\mathbf{R}^H\mathbf{R} = \mathbf{I}_N$ and $\mathbf{W}^H\mathbf{W} = \mathbf{I}_K$. Matrix $\mathbf{T}$ is diagonal of dimensions $N \times K$ and it has $K$ non zero diagonal elements, which are the singular values of $\mathbf{B}$. We can write Equation (5.12) as follows:

$$\mathbf{B}\mathbf{B}^H = \mathbf{R}\mathbf{T}\mathbf{W}^H\mathbf{W}\mathbf{T}^H\mathbf{R}^H \tag{5.29}$$

$$= \mathbf{R}\mathbf{T}\mathbf{T}^H\mathbf{R}^H \tag{5.30}$$

The matrix $\mathbf{T}\mathbf{T}^H$ is an $N \times N$ diagonal matrix, and it has only $K$ non zero values. By comparing Equation (5.13) and Equation (5.30) we have:

$$\mathbf{A} = \mathbf{R} \tag{5.31}$$

$$\mathbf{L} = \mathbf{T}\mathbf{T}^H \tag{5.32}$$

Considering Equation (5.1), the following expression holds for the feed signals:

$$\mathbf{x} = \mathbf{R}\mathbf{T}\mathbf{W}^H\mathbf{s} \tag{5.33}$$

By considering Equation (5.33), the following observations are in order:

- The product $\mathbf{W}^H\mathbf{s}$, which we denote as $\mathbf{v}$, yields a $K \times 1$ vector of non-zero components.
- The product $\mathbf{T}\mathbf{v}$ yields an $N \times 1$ vector, with only $K$ non zero entries (the first $K$ components).
- Considering Equation (5.14) and Equation (5.31), and assuming that $\mathbf{A}_M^H$ is built with the first $M$ columns of $\mathbf{A}$, applying compression to $\mathbf{x}$ is equivalent to obtaining the vector of feedlets as follows:

$$\mathbf{f}_{\text{a,klt}} = \mathbf{R}_M^H\mathbf{R}\begin{bmatrix} \mathbf{v} \\ \mathbf{0}_{N-K} \end{bmatrix} \tag{5.34}$$

$$= \begin{bmatrix} \mathbf{I}_M & \mathbf{0}_{M\times N-K} \end{bmatrix}\begin{bmatrix} \mathbf{v} \\ \mathbf{0}_{N-K} \end{bmatrix} \tag{5.35}$$

- According to the value of $M$, $\mathbf{f}_{\text{a,klt}}$ can be written as follows:

$$\mathbf{f}_{\text{a,klt}} = \begin{bmatrix} \mathbf{v} \\ \mathbf{0}_{N-K} \end{bmatrix} \qquad \text{if } M = N \tag{5.36}$$

$$\mathbf{f}_{\text{a,klt}} = \begin{bmatrix} \mathbf{v} \\ \mathbf{0}_{M-K} \end{bmatrix} \qquad \text{if } K \leq M \leq N \tag{5.37}$$

$$\mathbf{f}_{\text{a,klt}} = \mathbf{v} \qquad \text{if } M = K \tag{5.38}$$

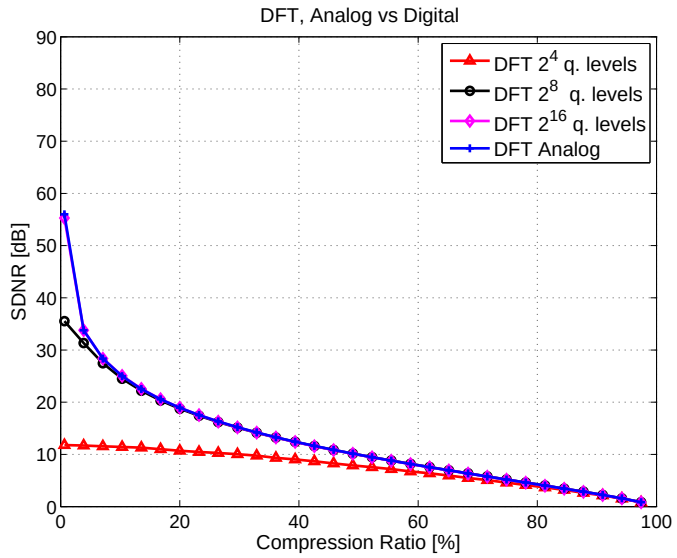


Figure 5.1: Comparison among quantization strategies and analog case in terms of SDNR as a function of the compression ratio for the DFT.

Consequently, a space spanned by $K$ eigenvectors of $\mathbf{Z}$ (as long as they are the ones corresponding to the non zero eigenvalues) is sufficient to describe the feed signals with the KLT. As long as $K < M < N$, there is no potential loss (except for the one due to quantization in the digital case), i.e., the SDNR is potentially infinite. Then, since $K = 100$, it can be seen that for $CR = 35\%$ which corresponds to $M = 100$, i.e., $N - M = 55$, the SDNR starts decreasing very drastically. Hence, we can state that with the KLT, bandwidth compression up to 35% comes with no compression loss.

In Figure 5.5 we represent a comparison between the *sorting* and the *non sorting* paradigms for the analog case. Clearly *sorting* comes with better performance in terms of SDNR for a fixed value of $CR$, although it requires greater complexity. It also appears as the KLT is more robust to non sorting. This is due to the fact that, for how the KLT basis is constructed, the basis vectors are ordered increasingly according to the values of the eigenvalues. Thus, the basis already comes with an implicit sorting criterion.

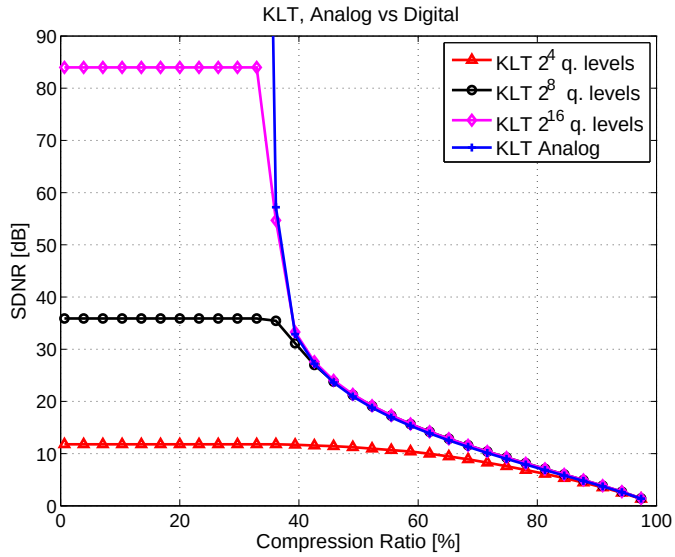


Figure 5.2: Comparison among quantization strategies and analog case in terms of SDNR as a function of the compression ratio for the KLT.

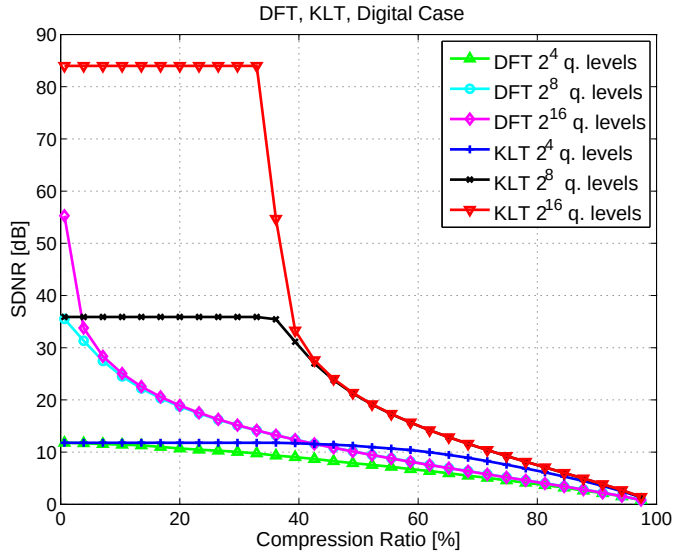


Figure 5.3: Comparison among quantization strategies in terms of SDNR as a function of the compression ratio for the DFT and the KLT in the digital case.

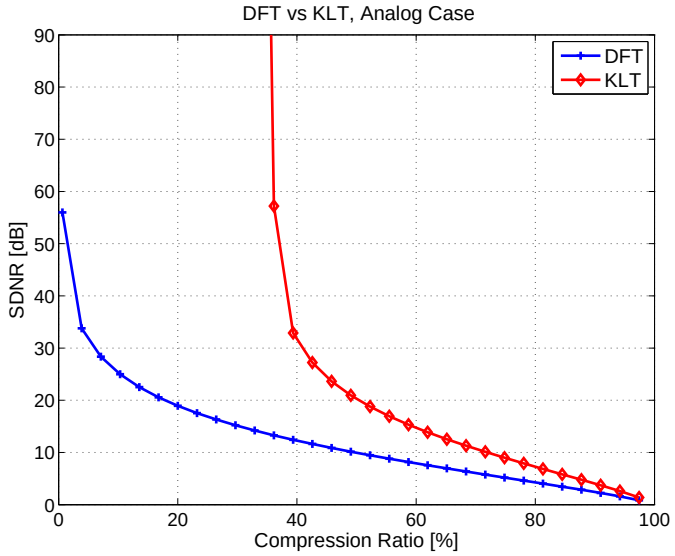


Figure 5.4: Comparison between DFT and the KLT in the analog case.

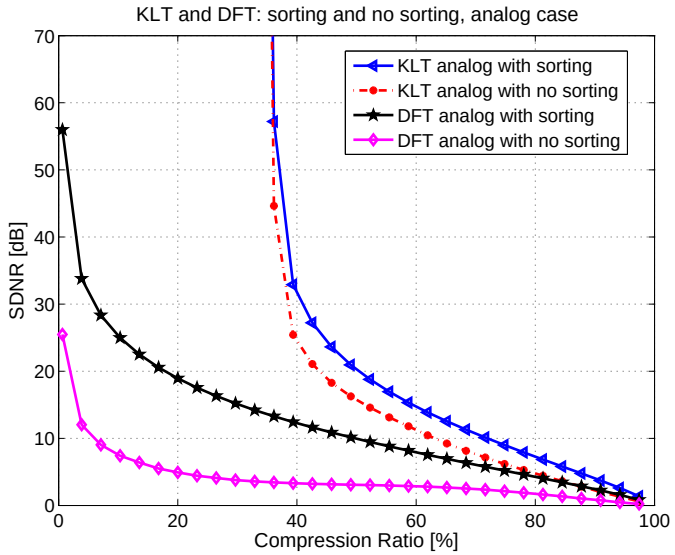


Figure 5.5: Comparison between the *sorting* and *non sorting* paradigms for signal compression

# Chapter 6

# Joint Feeder Link Bandwidth Compaction and Precoding

Up to this point, we have conducted a preliminary study with the objective of evaluating the effect of bandwidth reduction on the quality of on-board reconstructed feed signals. Bandwidth compaction was achieved by projecting feed signals on a subspace of reduced dimensions. The considered subspace was obtained through truncation of the DFT or the KLT basis. We considered a simplified feeder link scenario with a fixed beamforming matrix.

In this chapter we have a view on evaluating the impact of bandwidth reduction on a complete gateway to UTs system where, instead of fixed beamforming, adaptive interference mitigation policies are adopted at the gateway in order to allow for a full color frequency reuse scheme ($N_c = 1$). Space processing, i.e., Coarse Beamforming, is meant to yield feed signal reconstruction from a subset of intermediate feedlets and ground processing is designed to adaptively mitigate interference with linear precoding. Coarse Beamforming has to be fixed and non channel adaptive, in order to keep payload complexity low. The introduction of a fixed processing scheme on board the satellite to reconstruct feed signals from the subset of feedlets has an impact on the design of the precoding matrix that has to take into account a new equivalent channel which also includes the effect of Coarse Beamforming. The effect of non-adaptive space processing reflects on the cardinality of the set of signals that are to be sent from the gateway to the satellite. The channel-dependent precoder produces a number of feedlets which is in accordance with the dimension of the fixed Coarse Beamforming basis used on board the payload. Considering the regularized channel inversion precoder [100], we evaluate system performance in terms of spectral

efficiency and availability as functions of the dimension of the subspace on which feed signals are projected. We still design the Coarse Beamforming schemes along the lines of PCA and DFT. PCA is now based on the SVD of the mean channel matrix.

The set up we are suggesting, and the way these signal processing techniques are arranged and deployed in the system, yielding a hybrid space/ground processing structure, with a view on a more efficient use of the feeder link bandwidth, is highly innovative and beyond the state of the art, and it could become a breakthrough in the design of next generation satellite systems.

## 6.1 System Model

In the forward link of the considered broad-band satellite system a single gateway provides service to a set of fixed UTs, located on the coverage area. We assume FDM, TDM, and SDM in the user link, together with full frequency reuse ($N_c = 1$) such that, for a given frequency band, at each time slot, the gateway is simultaneously serving a subset of $K$ users, where $K$ is also the number of beam cells deployed on the coverage area. The vector of received signals at the UTs can then be written as follows:

$$\mathbf{y} = \mathbf{H}\mathbf{x} + \mathbf{n} \tag{6.1}$$

where $\mathbf{y}$ is a $K \times 1$ vector containing the received signals at each UT, $\mathbf{x}$ is a $N \times 1$ vector which contains the on-board transmitted feed signals, $\mathbf{n}$ is a $K \times 1$ vector containing the stack of noise components. The user link channel matrix $\mathbf{H}$ is of size $K \times N$, and it accounts for the feed radiation patterns (element $h_{i,j}$ of the matrix represents the complex gain of feed $j$ corresponding to the position of user $i$), path loss, rain fading, and its elements are normalized so that elements of $\mathbf{n}$ have unit variance. The vector of feed signals is derived as follows:

$$\mathbf{x} = \mathbf{C}^H\mathbf{f} \tag{6.2}$$

where $\mathbf{C}^H$ is the non channel adaptive Coarse Beamforming matrix of size $N \times M$, and $\mathbf{f}$ is a $M \times 1$ vector containing the stack of feedlets. We consider the feeder link to be analog, and perfectly calibrated and noiseless. At the gateway, adaptive linear precoding takes place, and the expression for $\mathbf{f}$ is the following:

$$\mathbf{f} = \mathbf{F}\mathbf{s} \tag{6.3}$$

where $\mathbf{F}$ is the $M \times K$ precoding matrix, and $\mathbf{s}$ is the $K \times 1$ vector containing the user symbols. The expression for the received signal thus becomes:

$$\mathbf{y} = \mathbf{H}\mathbf{C}^H\mathbf{F}\mathbf{s} + \mathbf{n} \tag{6.4}$$

$$= \mathbf{H_{eq}}\mathbf{F}\mathbf{s} + \mathbf{n} \tag{6.5}$$

where $\mathbf{H_{eq}}$ can be considered as an equivalent channel matrix, of dimensions $K \times M$, which takes into account the channel on the user link, and the effect of space processing. A schematic view of the system under examination is depicted in Figures 4.1 and 4.3.

## 6.2 Linear Precoder Design

In this section we first briefly describe the linear precoder that we consider in this work. We use the regularized inversion of the channel approach [100], and the corresponding $M \times K$ precoding matrix can be written as:

$$\mathbf{F} = \sqrt{\gamma}\, {\mathbf{H_{eq}}}^H \left( \mathbf{H_{eq}} {\mathbf{H_{eq}}}^H + \frac{K}{P}\mathbf{I}_K \right)^{-1} \tag{6.6}$$

where the value of constant $\gamma$ has to comply with the transmit power constraint:

$$\text{trace}(\mathbf{C}^H\mathbf{F}\mathbf{F}^H\mathbf{C}) \leq P \tag{6.7}$$

where $P$ denotes the total transmit power. We assume that $\mathbf{H_{eq}}$ is known at the gateway. The corresponding symbol vector estimate $\hat{\mathbf{s}}$ is then obtained as $\hat{\mathbf{s}} = (\sqrt{\gamma})^{-1}\mathbf{y}$ by inserting (6.6) into (6.5).

Before tackling the problem of designing the fixed Coarse Beamforming matrix $\mathbf{C}^H$, we link the problem considered in this section with the preliminary study presented in Chapter 5. By inserting $\mathbf{H_{eq}} = \mathbf{H}\mathbf{C}^H$ into (6.6), we get

$$\mathbf{F} = \sqrt{\gamma}\, \mathbf{C}\mathbf{H}^H \left( \mathbf{H}\mathbf{C}^H\mathbf{C}\mathbf{H}^H + \frac{K}{P}\mathbf{I}_K \right)^{-1}, \tag{6.8}$$

from which we see that the considered scheme (on-ground precoding and on-board Coarse Beamforming) depicted in Figure 4.3 is equivalent to the preliminary analysis scheme of Figure 4.2 if we replace $\mathbf{B}$ by $\sqrt{\gamma}\, \mathbf{H}^H \left(\mathbf{H}\mathbf{C}^H\mathbf{C}\mathbf{H}^H + \frac{K}{P}\mathbf{I}_K\right)^{-1}$. That is, instead of having a fixed beamforming matrix $\mathbf{B}$ as in Section 5, we consider here the presence of a channel adaptive precoding which also takes into account the choice of the on-board Coarse Beamforming matrix.

## 6.3 Joint Precoding and Coarse Beamforming

The mean squared error (MSE) on the symbol of user $k$ is defined as:

$$\epsilon_k = E[|\hat{s}_k - s_k|^2]. \tag{6.9}$$

The sum MSE (SMSE) associated with the precoder (6.6) can be shown to be

$$\begin{aligned}\text{SMSE} =& \sum_{k=1}^{K} \epsilon_k \\ =& \frac{K}{P}\text{trace}\left((\mathbf{H_{eq}}\mathbf{C}\mathbf{C}^H{\mathbf{H_{eq}}}^H + \frac{K}{P}\mathbf{I}_K)(\mathbf{H_{eq}}{\mathbf{H_{eq}}}^H + \frac{K}{P}\mathbf{I}_K)^{-2}\right) \\ =& \frac{K}{P}\text{trace}\left((\mathbf{H}\mathbf{C}^H\mathbf{C}\mathbf{C}^H\mathbf{C}\mathbf{H}^H + \frac{K}{P}\mathbf{I}_K)(\mathbf{H}\mathbf{C}^H\mathbf{C}\mathbf{H}^H + \frac{K}{P}\mathbf{I}_K)^{-2}\right)\end{aligned} \tag{6.10}$$

We now analyze the effect of the Coarse Beamforming matrix $\mathbf{C}^H$ on the system, and in particular taking the SMSE as a performance measure. $\mathbf{C}^H$, recall, is of size $N \times M$, with $M \leq N$. Obviously, the performance of the system is maximized (i.e. the SMSE (6.10) is minimized) if all feed signals are available on ground. This corresponds to when no Coarse Beamforming is performed on board, i.e. $\mathbf{C}^H = \mathbf{I}_N$, in which case the SMSE reduces to:

$$\text{SMSE} = \frac{K}{P}\text{trace}\left((\mathbf{H}\mathbf{H}^H + \frac{K}{P}\mathbf{I}_K)^{-1}\right) \tag{6.11}$$

$$= \sum_{k=1}^{K} \frac{\frac{K}{P}}{|\sigma_k|^2 + \frac{K}{P}} \tag{6.12}$$

where $\sigma_1, \ldots, \sigma_K$ denote the singular values of $\mathbf{H}$. That is, $\sigma_1, \ldots, \sigma_K$ are the diagonal elements of the wide matrix $\mathbf{\Sigma}$ defined by the following singular value decomposition (SVD) of the channel matrix:

$$\mathbf{H} = \mathbf{U}\mathbf{\Sigma}\mathbf{V}^H \tag{6.13}$$

The rank of $\mathbf{H}$ is precisely the rank of the diagonal matrix $\mathbf{\Sigma}$, or equivalently the number of non-zero singular values. We consider that in this decomposition the singular values are sorted in a decreasing order. Now, a careful analysis of (6.10) leads to the following observations:

$\mathcal{O}.1$ If $M = N$, any unitary matrix $\mathbf{C}^H$ (such that $\mathbf{C}^H\mathbf{C} = \mathbf{I}_N$) achieves (6.12). This extreme case is trivially understood by the fact that the precoder can perfectly pre-compensate the effect of any unitary matrix $\mathbf{C}^H$.

$\mathcal{O}.2$ If $K \leq M \leq N$, the SMSE (6.12) can be achieved by designing $\mathbf{C}^H = \mathbf{V}_M$, where $\mathbf{V}_M$ denotes the first $M$ columns of $\mathbf{V}$. However, it is important to note that this solution does not comply with the non adaptability of space processing, since $\mathbf{V}_M$ is not a fixed matrix but instead it is channel-dependent.

$\mathcal{O}.3$ If $M < K$, the SMSE (6.12) cannot be achieved, the reason being that the precoding is carried out in a space of smaller dimension than the number of users.

In the framework of PCA, the Singular Value Decomposition (SVD) can be used to partition an $N$-dimensional vector space into dominant and non-dominant subspaces. This corresponds to reducing the number of dimensions of the space that contains the useful information, and keeping a subspace, which actually consists in those dimensions along which data points exhibit most variation. This is why we elected the SVD as a Coarse Beamforming tool for this scenario. If matrix $\mathbf{C}^H$ were channel-adaptive, it could be designed according to what was stated in $\mathcal{O}.2$. But since $\mathbf{C}^H$ can not be adaptive, in order to implement a fixed on-board processing scheme, we design matrix $\mathbf{C}^H$ on the basis of the SVD decomposition of the *mean channel matrix* $\tilde{\mathbf{H}}$. This is related to the presence of correlation among feed radiation patterns and to the considered spatial distributions of users. We use the mean channel matrix since $\mathbf{C}^H$ cannot be adaptive, and it has to be designed in order to be as suitable as possible for any channel realization. In order to obtain $\tilde{\mathbf{H}}$, in fact, matrix $\mathbf{H}$ is averaged over different configurations of users on the coverage area which is assumed to be divided into $K$ cells [1]. One UT per cell is considered, with a random position within its assigned area. Consequently, the $K$ users that are simultaneously served at a given time slot and in a given frequency band are reasonably spread over the coverage area. Since each UT is confined to its assigned cell area, and the mean channel matrix $\tilde{\mathbf{H}}$ is averaged over the set of random positions that each UT can have within its region, it is legitimate to assume that the channel matrix $\mathbf{H}$ does not vary much around $\tilde{\mathbf{H}}$. This assumption justifies our non adaptive Coarse Beamforming technique based on the SVD of the mean channel matrix. Since the mean channel matrix $\tilde{\mathbf{H}}$ of dimensions $K \times N$ can be written as:

$$\tilde{\mathbf{H}} = \tilde{\mathbf{U}}\tilde{\mathbf{\Sigma}}\tilde{\mathbf{V}}^H \tag{6.14}$$

[1] In order to identify the cell regions, we used the fixed beamforming scheme provided by ESA, although this matrix has not been used to process the user signals in this scheme.

matrix $\mathbf{C}$ has been designed as a subset of $M < N$ columns of $\tilde{\mathbf{V}}$, considering that the singular values of $\tilde{\mathbf{H}}$ are in decreasing order. We call $\mathbf{C}_{\text{svd}}^H$ the Coarse Beamforming matrix relative to this approach, and it can be written as follows:

$$\mathbf{C}_{\text{svd}}^H = \tilde{\mathbf{V}}_M \tag{6.15}$$

where $\tilde{\mathbf{V}}_M$ denotes the matrix obtained by extracting the first $M$ columns of $\tilde{\mathbf{V}}$.

In a similar fashion as in Chapter 5, the simulation results will compare the SVD-based Coarse Beamforming in (6.15) with a DFT-based Coarse Beamforming. We design the latter by using a truncated version of the $N \times N$ DFT matrix $\mathbf{D}$ defined in Equation (5.19). More precisely, the fixed DFT-based Coarse Beamforming is defined as follows:

$$\mathbf{C}_{\text{dft}}^H = \mathbf{D}_M \tag{6.16}$$

where $\mathbf{D}_M$ denotes the $N \times M$ matrix obtained by considering the $M$ first columns of $\mathbf{D}$.

# Chapter 7

# Results and Conclusion for Part II

In this chapter we present simulation results and draw a conclusion. We consider two performance metrics: (i) spectral efficiency (bits/s/Hz) and (ii) non availability, i.e. the probability that the link associated with a given user is not available, which happens when the Signal to Interference-plus-Noise Ratio (SINR) falls below the SINR needed to support the lowest modulation and coding mode of the considered standard. Both these metrics are deduced from Table 7.2, which provides a one to one relationship between the required received SINR and the efficiency[1] (bits/symbol) achieved by the different adaptive modulation and coding modes included in the DVB-S2 standard, for a packet error rate (PER) of $10^{-6}$. The working points have been extrapolated from the PER curves reported in the DVB-S2 guidelines document [101], with some additional approximate implementation losses [87].

The rest of the parameters used in the simulation are summarized in Table 7.1. We base our analysis on an antenna radiation pattern (i.e. the $\{h_{i,j}\}$ ) provided in [98]. This corresponds to an array fed reflector antenna with $N = 155$ radiating elements, or feeds. As previously mentioned in Section 6.3, UTs are assumed to be reasonably spread over the coverage area, and to be located in different cells. $K = 100$ cells are assumed to be deployed on the coverage area, i.e. 100 users per carrier and per time slot are simultaneously served. Since the channel matrix $\mathbf{H}$ accounts for the antenna radiation patterns, it varies as users vary their positions. As mentioned in Section 6.2, the precoder has been designed according to the regularized channel inversion approach [100]. Two different Coarse Beamforming

[1] Excluding efficiency loss due to preamble and pilot insertion.

schemes based on SVD and DFT respectively are considered, relative to Equations (6.15) and (6.16). Figures 7.1 and 7.3 depict performance in terms of average spectral efficiency per user as a function of $P$. Figures 7.2 and 7.4 depict curves of probability of non availability as a function of $P$. Graphs in Figures 7.1 and 7.2 are obtained in the presence of SVD-based Coarse Beamforming for different values of $M$, as well as fixed beamforming provided by ESA (i.e. when $\mathbf{C}^H = \mathbf{B}$) and, as a benchmark, the case of absence of Coarse Beamforming is inserted (i.e. $\mathbf{C}^H = \mathbf{I}_N$). Graphs in Figures 7.3 and 7.4, on top of this, add performance with DFT-based Coarse Beamforming. From Figures 7.1 and 7.2 it can be noticed that, in case of SVD-based Coarse Beamforming, performance is lower bounded by the case where $\mathbf{C}^H = \mathbf{B}$, and upper bounded by the case where adaptive precoding is implemented at the gateway, and no Coarse Beamforming is implemented on board. This is the case where satellite and gateway exchange the full set of feed signals. Bandwidth compression clearly comes with some performance loss, since the dimension of the feed signal space is reduced. A trade off must be sought between performance loss, and compression gain. It can be observed from Figures 7.3 and 7.4 that DFT-based Coarse Beamforming implemented jointly with precoding performs worse than the SVD-based Coarse Beamforming case. It even performs worse than the fixed beamforming scheme when $M = 100$. This is coherent with the results described in Section 5.5. PCA, in fact, offers a basis which naturally captures the characteristics of the signal it is meant to describe. It is not surprising then that for a given value of $M$, the spectral efficiency and the probability of availability obtained with SVD-based Coarse Beamforming are better than what is obtained with the DFT-based Coarse Beamforming.

As a conclusion, we can state that this work has tackled the issue of feeder link bandwidth compression in the forward link of a broad-band multi-beam satellite system. In order to reduce spectral requirements on the feeder link when the number of on-board antenna feeds exceeds the number of users, we suggest a hybrid architecture where a fixed non-channel-adaptive processing scheme is implemented on board the payload. This allows to relax bandwidth requirements on the feeder link and to keep payload complexity low by projecting the set of feed signals on a subspace of reduced dimensions, but it comes with a degree of degradation of the feed signals. We first evaluated the impact of signal compression on the quality of reconstructed feed signals, and we showed how a KLT-based compression outperforms the DFT-based scheme. We then considered a complete gateway to UTs system, with interference mitigation techniques implemented at the ground segment. In this set-up we ob-

served the impact of space processing, which we refer to as Coarse Beamforming, on the performance of the precoder in terms of spectral efficiency and availability. We considered SVD- and DFT-based Coarse Beamforming for this scenario, and we showed how the SVD-based Coarse Beamforming outperforms both the DFT-based scheme and the fixed beamforming scheme provided by ESA. As a general conclusion, we can state that PCA is the most appropriate tool to deal with feeder link bandwidth reduction, although it comes with increased complexity with respect to the DFT-based scheme. PCA- and DFT-based approaches have been the object of this study, but of course we are not claiming that these methods are optimal in terms of the trade-off that can be achieved between bandwidth reduction and signal degradation. A very interesting further development of this work would certainly consist in exploring different transforms, and make cross-comparisons among the different Coarse Beamforming schemes by taking into account factors like complexity and performance limits. Additionally, our work is based on the assumption of perfect channel estimation. A more in-depth study should take into consideration channel estimation errors as well as antenna calibration errors to evaluate the robustness of the Coarse Beamforming approach against imperfect parameter estimation, and to be able to answer to questions such as: *For a given SDNR target, which estimation noise can we tolerate in order to have a certain Compression Ratio for the feeder link bandwidth?* Finally, this work is based on real antenna pattern data provided by ESA. An analytical study based on closed form expressions of the antenna gains would provide more general conclusions, and more rigorous expressions for the performance limits. An optimal splitting scheme could then be devised to provide the maximum possible compression for a given SDNR target.

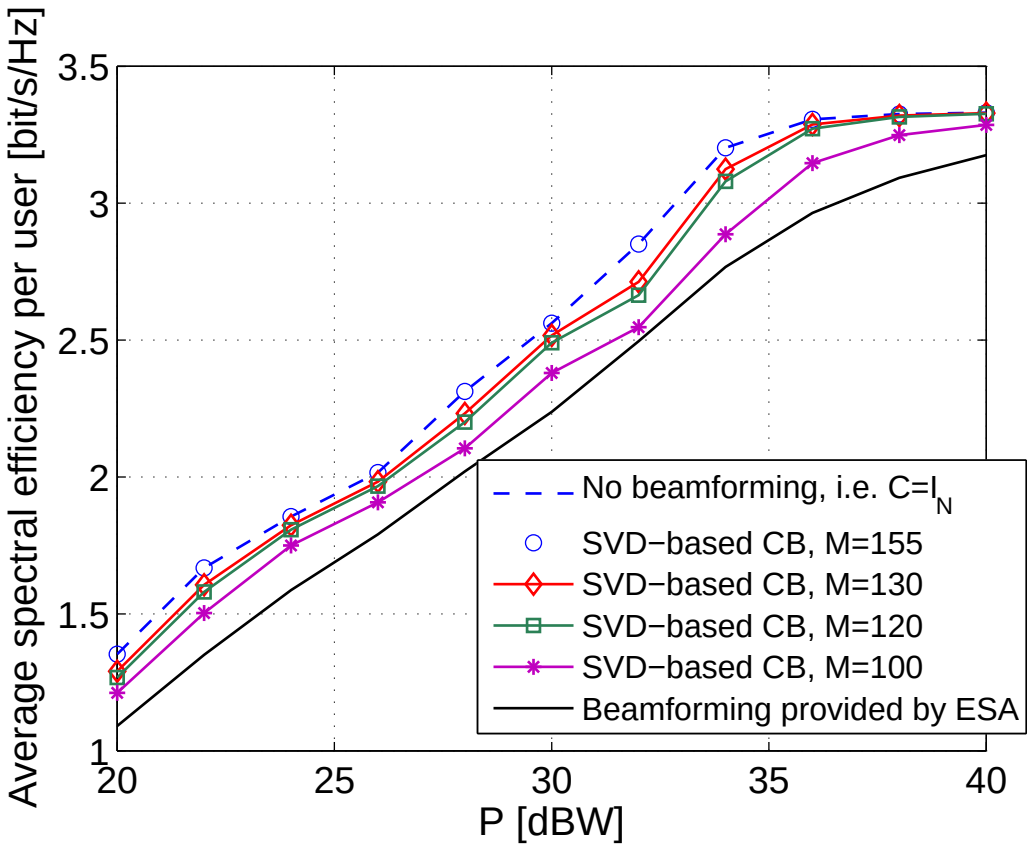


Figure 7.1: Spectral efficiency: subspace dimension varies from 100 to 155 for SVD-based Coarse Beamforming

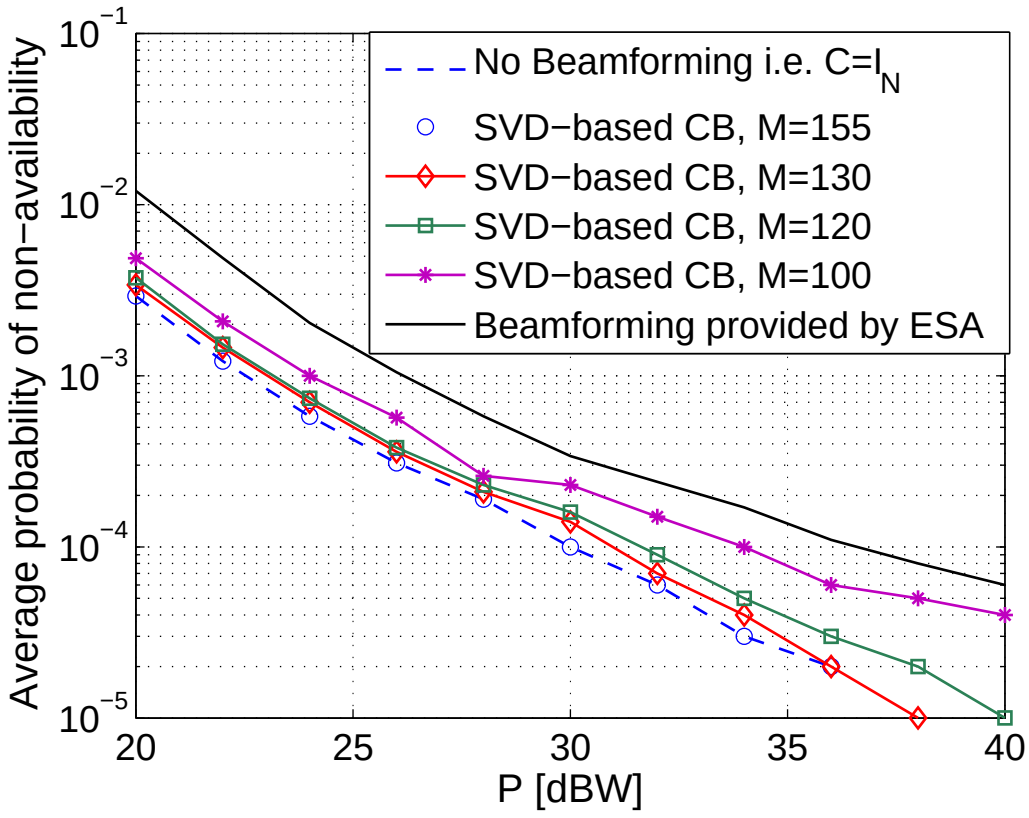


Figure 7.2: Availability: subspace dimension varies from 100 to 155 for SVD-based Coarse Beamforming

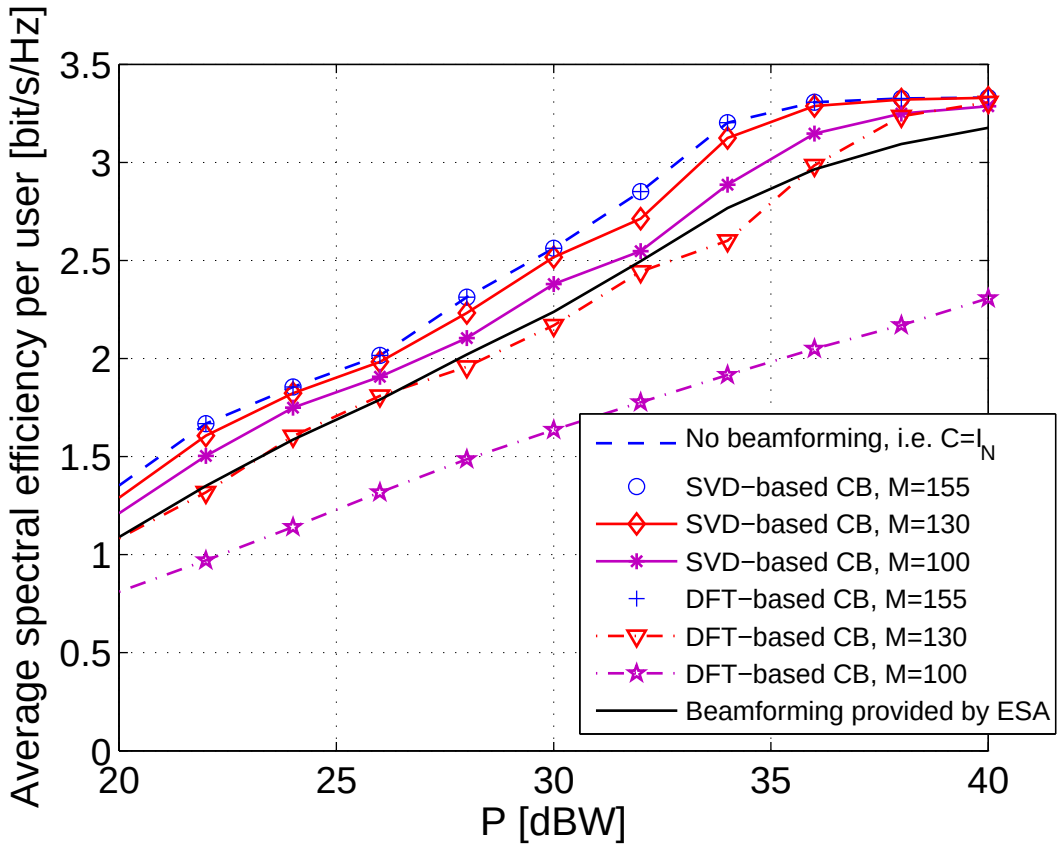


Figure 7.3: Spectral efficiency: subspace dimension varies from 100 to 155 for SVD- and DFT-based Coarse Beamforming

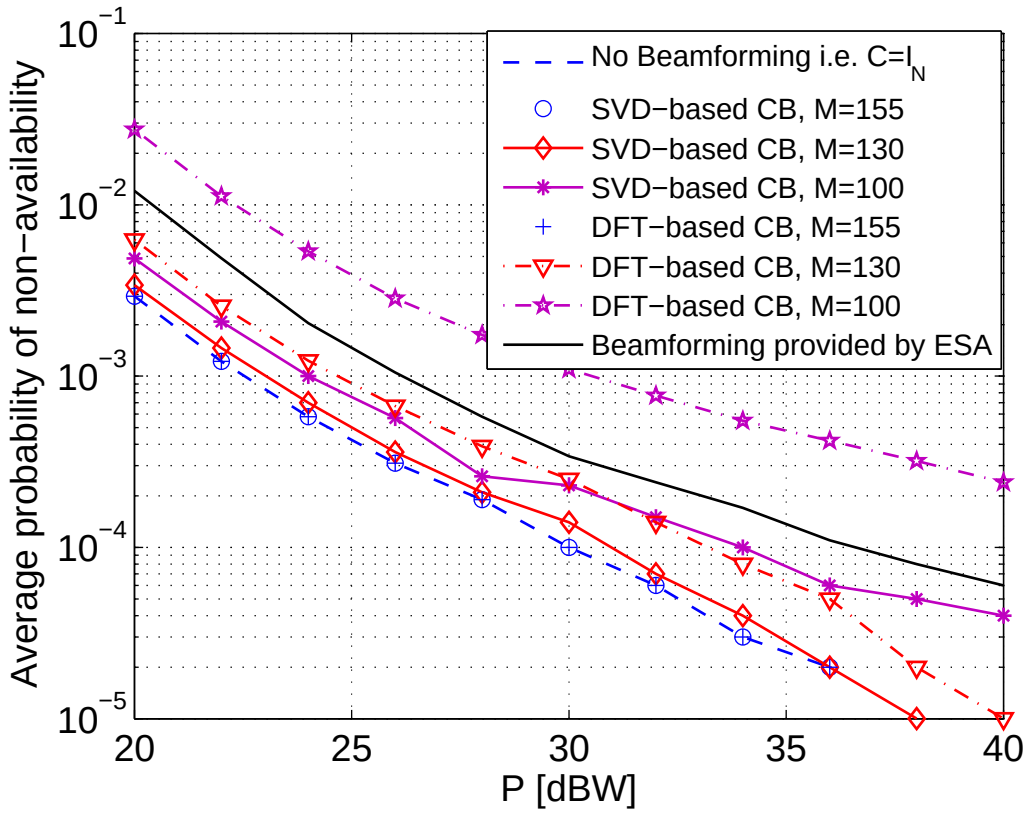


Figure 7.4: Availability: subspace dimension varies from 100 to 155 for SVD- and DFT-based Coarse Beamforming

Table 7.1: User Link System Parameters

| Parameter | Value |
|---|---|
| Satellite height | 35786 Km (geostationary) |
| Satellite longitude, latitude | 10° east, 0° |
| Satellite antenna architecture | Array Fed Reflector |
| Number of feeds $N$ | 155 |
| Feed gain patterns $h_{i,j}$ | provided by ESA |
| Number of beams ($K$) | 100 |
| Beamforming matrix $\mathbf{B}$ | provided by ESA |
| UTs location distribution | Uniformly distributed |
| Frequency on user link | 20 GHz ($K_a$ band) |
| Total service bandwidth $B_T$ | 125 MHz |
| Roll-off factor | 0.25 |
| Polarization | 1 |
| UT antenna gain $G_R^2$ | 41.7 dBi |
| UT clear sky $G_R^2/T_{ClearSky}$ | 17.68 dBi/K |

Table 7.2: Considered Modulation and Coding Modes and Required SINR

| ModCod mode | Efficiency Info bit / symbol | Required SINR [dB] (with approx. impl. losses) |
|---|---|---|
| QPSK_14 | 0.5 | -2.72 |
| QPSK_13 | 2/3 | -1.52 |
| QPSK_12 | 1 | 0.73 |
| QPSK_35 | 1.2 | 1.93 |
| QPSK_23 | 4/3 | 2.83 |
| QPSK_34 | 1.5 | 3.78 |
| QPSK_56 | 5/3 | 4.83 |
| 8PSK_35 | 1.8 | 5.33 |
| 8PSK_23 | 2 | 6.43 |
| 8PSK_34 | 2.25 | 7.63 |
| 16APSK_23 | 8/3 | 9.95 |
| 16APSK_34 | 3 | 11.20 |
| 16APSK_45 | 3.2 | 12.05 |
| 16APSK_56 | 10/3 | 12.60 |
| 32APSK_34 | 3.75 | 14.58 |
| 32APSK_45 | 4 | 15.08 |
| 32APSK_56 | 25/6 | 16.18 |

# Appendices

# Appendix A

# Centralized Beamforming

Classical array analysis deals with centralized beamformers. This section refers to the theory in [2]. Centralized antenna arrays play an important role in many areas, namely:

- Radar
- Radio Astronomy
- Sonar
- Communications
- Direction-finding
- Seismology
- Medical diagnosis and treatment

## Spatial Filtering

The filtering properties of the system can be expressed in terms of a dependence upon angle or wavenumber and the beamforming coefficients are designed to enhance or reject signals according to their spatial dependence. In case of narrow band signals, the beamforming coefficients are complex scalars, which have the effect of scaling and phase rotating the outgoing or incoming signal. The configuration of sensors is then denoted as a phased array. Different array geometries can be envisaged, such as linear, planar and volumetric. The two aspects of centralized array design that determine the performance of the spatial filter are the geometry of the system, and

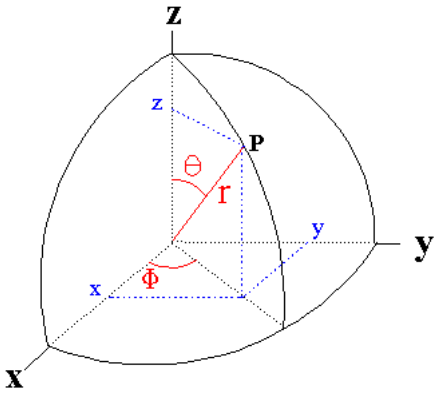


Figure A.1: Spherical Coordinate System.

the choice of the complex weightings of the data at each sensor. The fixed geometry guarantees tight control of the relative phase shifts among elements, and the system is naturally locked to a unique phase and frequency reference. As a consequence, the beampattern is a deterministic function of the number of sensors, their positions, and their beamforming coefficients.

A spherical coordinate system, shown in Figure A.1, is characterized by the three parameters $\theta$, $\phi$, and $r$ which are, respectively, the polar angle, the azimuthal angle, and the radial distance from the origin. The relationships between rectangular and spherical coordinates are the following:

$$\begin{aligned} x &= r\sin\theta\cos\phi \\ y &= r\sin\theta\sin\phi \\ z &= r\cos\theta \end{aligned}$$

An array is a configuration of $N$ sensors scattered in the 3-dimensional space. An example of an $N$-dimensional array is shown in Figure A.2. The position of sensor $i$ can be identified with a 3-dimensional vector $\mathbf{p}_i$:

$$\mathbf{p}_i = \begin{bmatrix} r_i\sin\theta_i\cos\phi_i \\ r_i\sin\theta_i\sin\phi_i \\ r_i\cos\theta_i \end{bmatrix}. \tag{A.1}$$

When a plane wave, with velocity of propagation $c$, impinges on the array, its direction can be identified by vector $\mathbf{a}$, as shown in Figure A.2, and represented as

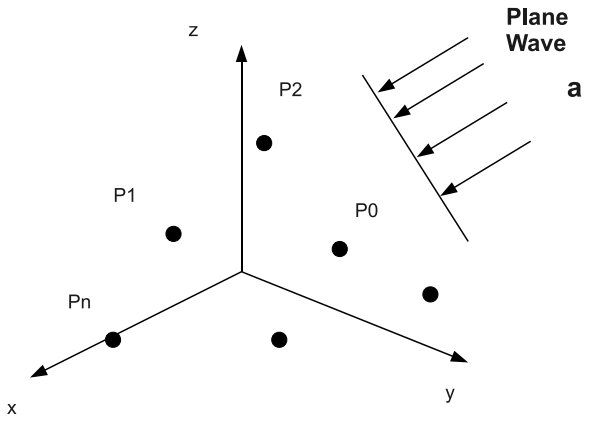


Figure A.2: $N$-dimensional array with plane-wave input.

follows:

$$\mathbf{a} = \begin{bmatrix} -\sin\theta_i \cos\phi_i \\ -\sin\theta_i \sin\phi_i \\ -\cos\theta_i \end{bmatrix}. \tag{A.2}$$

The wavenumber $\mathbf{k}$ is defined as:

$$\mathbf{k} = \frac{2\pi}{\lambda}\mathbf{a} \tag{A.3}$$

where $\lambda$ is the wavelength of the plane wave. The array-manifold vector, which incorporates the spatial characteristics of the array is defined as follows:

$$\mathbf{v_k}(\mathbf{k}) = \begin{bmatrix} e^{-j\mathbf{k}^T\mathbf{p}_0} \\ e^{-j\mathbf{k}^T\mathbf{p}_1} \\ \vdots \\ e^{-j\mathbf{k}^T\mathbf{p}_{N-1}} \end{bmatrix}. \tag{A.4}$$

In a phased array, sensors adjust the incoming or outgoing signal with a complex weight, in order to create the desired beampattern in space. The complex weight vector can be denoted as:

$$\mathbf{w}^H = \left[w_0^*,\ w_1^*, \ldots, w_{N-1}^*\right]. \tag{A.5}$$

The frequency-wave-number response function of the array is:

$$\Upsilon(\lambda, \mathbf{k}) = \mathbf{w}^H \mathbf{v_k}(\mathbf{k}). \tag{A.6}$$

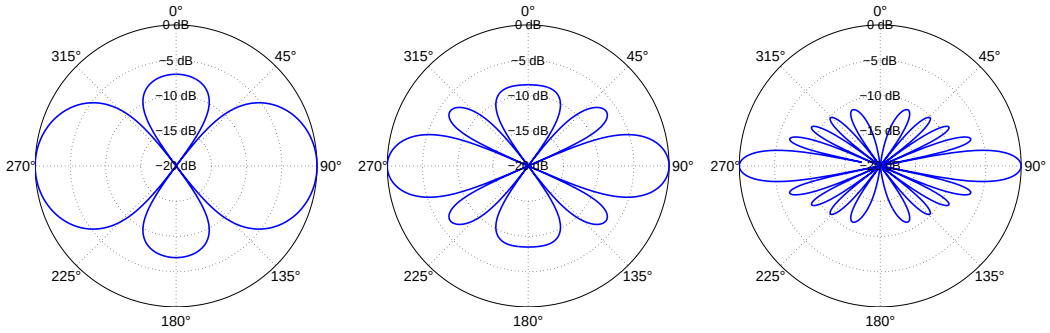


(a) $N = 5$ (b) $N = 10$ (c) $N = 20$

Figure A.3: Beampatterns for ULAs with $d = \lambda/4$, and different values of the number of elements, $N$.

The beampattern of the array is the frequency-wave-number response function of the array evaluated versus the direction:

$$B(\lambda : \theta, \phi) = \Upsilon(\lambda, \mathbf{k})|_{\mathbf{k}=\frac{2\pi}{\lambda}\mathbf{a}(\theta,\phi)}. \tag{A.7}$$

## The Uniform Linear Array

When the $N$ sensors are all located on the $z$-axis, with uniform spacing equal to $d$, the array is linear and uniform. If the center of the array coincides with the center of the system, the positions of the $i$-th node is:

$$\mathbf{p}_i = \begin{bmatrix} 0 \\ 0 \\ \left(i - \frac{N-1}{2}\right) d \end{bmatrix} \tag{A.8}$$

where $i = 0, \ldots, N-1$.

If, in addition, the array is uniformly weighted, the following condition applies:

$$w_i = \frac{1}{N}, \quad \forall i = 0, \ldots, N-1 \tag{A.9}$$

the expression of the beampattern is:

$$B_\theta(\theta) = \frac{1}{N} \frac{\sin\left(\frac{N}{2}\frac{2\pi}{\lambda}\cos\theta d\right)}{\sin\left(\frac{1}{2}\frac{2\pi}{\lambda}\cos\theta d\right)}, \quad 0 \leq \theta \leq \pi \tag{A.10}$$

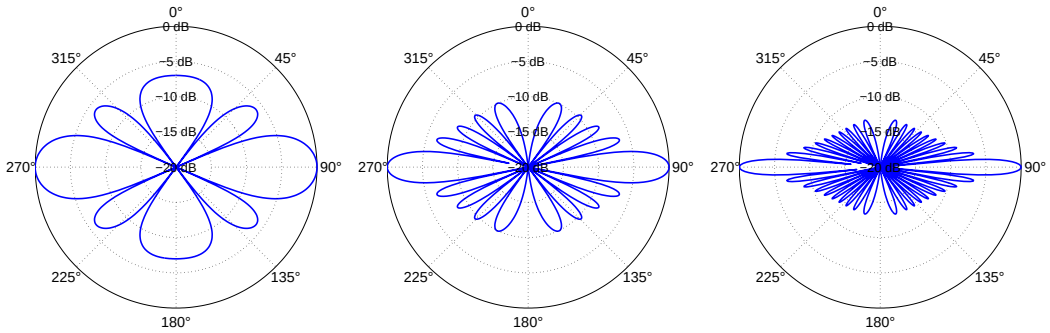


(a) $N = 5$ (b) $N = 10$ (c) $N = 20$

Figure A.4: Beampatterns for ULAs with $d = \lambda/2$, and different values of the number of elements, $N$.

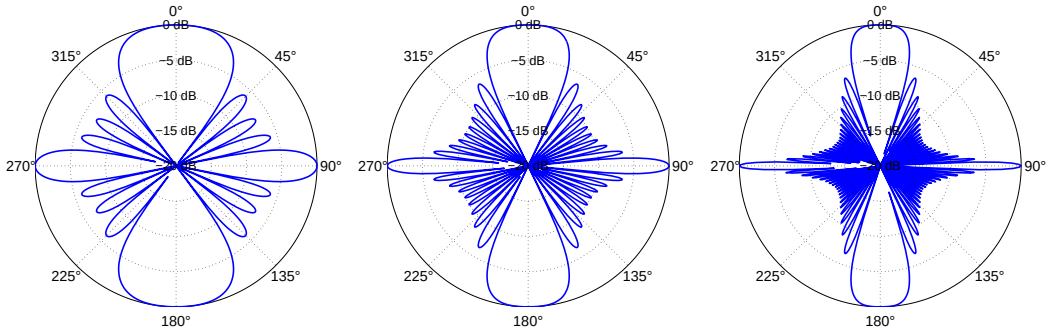


(a) $N = 5$ (b) $N = 10$ (c) $N = 20$

Figure A.5: Beampatterns for ULAs with $d = \lambda$, and different values of the number of elements, $N$.

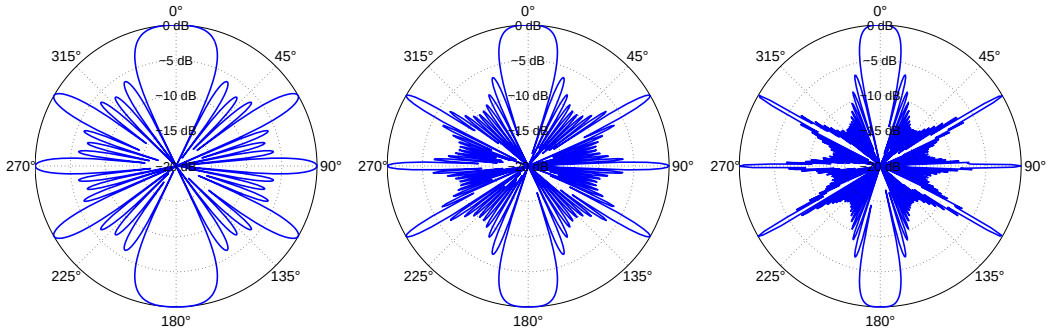


(a) $N = 5$ (b) $N = 10$ (c) $N = 20$

Figure A.6: Beampatterns for ULAs with $d = 2\lambda$, and different values of the number of elements, $N$.

## Performance measures

Beampattern parameters:

- 3-dB beamwidth (the Half Power Beam Width, HPBW).
- Distance to first null.
- Distance to first sidelobe.
- Height of first sidelobe.
- Location of remaining nulls.
- Rate of decrease of sidelobes.
- Grating lobes.

Array parameters:

- Directivity.
- Array gain versus spatially white Gaussian noise.
- Sensitivity and the tolerance factor.

# Appendix B

# Proof of Propositions 1 and 2

For notational compactness, let us define

$$x \triangleq \frac{1}{N}\sum_{i=1}^{N}\cos\tilde{\psi}_i \tag{B.1}$$

$$y \triangleq \frac{1}{N}\sum_{i=1}^{N}\sin\tilde{\psi}_i \tag{B.2}$$

where $\tilde{\psi}_1,\ldots,\tilde{\psi}_N$ are independent random variables, identically and uniformly distributed in $[-\pi/K,+\pi/K)$ and the NRSS is simply $\sqrt{x^2+y^2}$. For $K\to\infty$, clearly $x\to 1$ and $y\to 0$. Thus, we expand the NRSS around $x=1$ and $y=0$ obtaining

$$\begin{aligned}\sqrt{x^2+y^2} =& x+\frac{3}{2}y^2-\frac{3}{2}xy^2+\frac{1}{2}x^2y^2+O\left(y^3\right)+O\left(y^3\right)(x-1)+O\left(y^3\right)(x-1)^2\\ &+O\left((x-1)^3\right).\end{aligned} \tag{B.3}$$

We now take expectations over $\tilde{\psi}_1,\ldots,\tilde{\psi}_N$. For the first term in (B.3),

$$\mathbb{E}[x] = \int_{-\frac{\pi}{K}}^{+\frac{\pi}{K}}\cdots\int_{-\frac{\pi}{K}}^{+\frac{\pi}{K}}\left(\frac{1}{N}\sum_{i=1}^{N}\cos\xi_i\right)f_{\tilde{\psi}_1\cdots\tilde{\psi}_N}(\xi_1,\ldots,\xi_N)d\xi_1\cdots d\xi_N \tag{B.4}$$

$$= \frac{1}{N}\left(\frac{K}{2\pi}\right)^N\int_{-\frac{\pi}{K}}^{+\frac{\pi}{K}}\cdots\int_{-\frac{\pi}{K}}^{+\frac{\pi}{K}}\left(\sum_{i=1}^{N}\cos\xi_i\right)d\xi_1\cdots d\xi_N \tag{B.5}$$

$$= \frac{K}{\pi}\sin\left(\frac{\pi}{K}\right) \tag{B.6}$$

$$= 1-\frac{\pi^2}{6K^2}+o\left(\frac{1}{K^2}\right). \tag{B.7}$$

For the second term, in turn,

$$\mathbb{E}\left[y^2\right] = \int_{-\frac{\pi}{K}}^{+\frac{\pi}{K}} \cdots \int_{-\frac{\pi}{K}}^{+\frac{\pi}{K}} \left(\frac{1}{N}\sum_{i=1}^{N}\sin\xi_i\right)^2 f_{\tilde{\psi}_1\cdots\tilde{\psi}_N}(\xi_1,\ldots,\xi_N)d\xi_1\cdots d\xi_N \tag{B.8}$$

$$= \frac{1}{N^2}\left(\frac{K}{2\pi}\right)^N \int_{-\frac{\pi}{K}}^{+\frac{\pi}{K}} \cdots \int_{-\frac{\pi}{K}}^{+\frac{\pi}{K}} \left(\sum_{i=1}^{N}\sin\xi_i\right)^2 d\xi_1\cdots d\xi_N \tag{B.9}$$

$$= \frac{K}{2\pi N}\left(\frac{\pi}{K} - \frac{1}{2}\sin\left(\frac{2\pi}{K}\right)\right) \tag{B.10}$$

$$= \frac{\pi^2}{3NK^2} + o\left(\frac{1}{K^2}\right) \tag{B.11}$$

and, for the third term,

$$\mathbb{E}\left[xy^2\right] = \int_{-\frac{\pi}{K}}^{+\frac{\pi}{K}} \cdots \int_{-\frac{\pi}{K}}^{+\frac{\pi}{K}} \left(\frac{1}{N}\sum_{i=1}^{N}\cos\xi_i\right)\left(\frac{1}{N}\sum_{i=1}^{N}\sin\xi_i\right)^2 \cdot f_{\tilde{\psi}_1\cdots\tilde{\psi}_N}(\xi_1,\ldots,\xi_N)d\xi_1\cdots d\xi_N \tag{B.12}$$

$$= \frac{1}{N^3}\left(\frac{K}{2\pi}\right)^N \int_{-\frac{\pi}{K}}^{+\frac{\pi}{K}} \cdots \int_{-\frac{\pi}{K}}^{+\frac{\pi}{K}} \left(\sum_{i=1}^{N}\cos\xi_i\right)\left(\sum_{i=1}^{N}\sin\xi_i\right)^2 d\xi_1\cdots d\xi_N \tag{B.13}$$

$$= \frac{K}{3\pi N^2}\sin^3\left(\frac{\pi}{K}\right) + \frac{N-1}{N^2}\frac{K^2}{2\pi^2}\sin\left(\frac{\pi}{K}\right)\left(\frac{\pi}{K} - \frac{1}{2}\sin\left(\frac{2\pi}{K}\right)\right) \tag{B.14}$$

$$= \frac{\pi^2}{3N^2K^2} + \frac{N-1}{N^2}\frac{\pi^2}{3K^2} + o\left(\frac{1}{K^2}\right) \tag{B.15}$$

Finally, the fourth term in (B.3)

$$\mathbb{E}\left[x^2y^2\right] = \int_{-\frac{\pi}{K}}^{+\frac{\pi}{K}} \cdots \int_{-\frac{\pi}{K}}^{+\frac{\pi}{K}} \left(\frac{1}{N}\sum_{i=1}^{N}\cos\xi_i\right)^2\left(\frac{1}{N}\sum_{i=1}^{N}\sin\xi_i\right)^2 \cdot f_{\tilde{\psi}_1\cdots\tilde{\psi}_N}(\xi_1,\ldots,\xi_N)d\xi_1\cdots d\xi_N \tag{B.16}$$

$$= \frac{1}{N^4}\left(\frac{K}{2\pi}\right)^N \int_{-\frac{\pi}{K}}^{+\frac{\pi}{K}} \cdots \int_{-\frac{\pi}{K}}^{+\frac{\pi}{K}} \left(\sum_{i=1}^{N}\cos\xi_i\right)^2\left(\sum_{i=1}^{N}\sin\xi_i\right)^2 d\xi_1\cdots d\xi_N \tag{B.17}$$

$$= \frac{K}{32\pi N^3}\left(\frac{4\pi}{K} - \sin\left(\frac{4\pi}{K}\right)\right) + \frac{N-1}{N^3}\frac{K^2}{4\pi^2}\left(\frac{\pi^2}{K^2} - \frac{1}{4}\sin^2\left(\frac{2\pi}{K}\right)\right)$$

$$+ \frac{4}{3}\frac{N-1}{N^3}\left(\frac{K}{2\pi}\right)^2\sin^4\left(\frac{\pi}{K}\right)$$

$$+ 2\frac{(N-1)(N-2)}{N^3}\left(\frac{K}{2\pi}\right)^3 4\sin^2\left(\frac{\pi}{K}\right)\left(\frac{\pi}{K} - \frac{1}{2}\sin\left(\frac{2\pi}{K}\right)\right) \tag{B.18}$$

$$= \frac{\pi^2}{3K^2N^3} + \frac{N-1}{N^3}\frac{\pi^2}{3K^2} + \frac{N-1}{N^3}\frac{\pi^2}{3K^2} + 2\frac{(N-1)(N-2)}{N^3}\frac{\pi^2}{3K^2} + o\left(\frac{1}{K^2}\right) \tag{B.19}$$

By putting together (B.7), (B.11), (B.15), and (B.19), the expectation of Equation (B.3) gives (2.18). This proves Proposition 1.

Proposition 2 follows from neglecting the imaginary part of $\hat{\mathcal{R}}_{N,K}$, in which case $\mathbb{E}[|\hat{\mathcal{R}}_{N,K}|]$ is given directly by (B.6).

# Appendix C

# Proof of Proposition 3

The second raw moment of $|\hat{\mathcal{R}}_{N,K}|$ equals

$$\mathbb{E}\left[|\hat{\mathcal{R}}_{N,K}|^2\right] = \int_{-\frac{\pi}{K}}^{+\frac{\pi}{K}} \cdots \int_{-\frac{\pi}{K}}^{+\frac{\pi}{K}} \left(\frac{1}{N}\sum_{i=1}^{N} \cos\xi_i\right)^2 f_{\tilde{\psi}_1 \cdots \tilde{\psi}_N}(\xi_1, \ldots, \xi_N) d\xi_1 \cdots d\xi_N + \int_{-\frac{\pi}{K}}^{+\frac{\pi}{K}} \cdots \int_{-\frac{\pi}{K}}^{+\frac{\pi}{K}} \left(\frac{1}{N}\sum_{i=1}^{N} \sin\xi_i\right)^2 f_{\tilde{\psi}_1 \cdots \tilde{\psi}_N}(\xi_1, \ldots, \xi_N) d\xi_1 \cdots d\xi_N \tag{C.1}$$

$$= \frac{1}{N^2}\left(\frac{K}{2\pi}\right)^N \int_{-\frac{\pi}{K}}^{+\frac{\pi}{K}} \cdots \int_{-\frac{\pi}{K}}^{+\frac{\pi}{K}} \left(\sum_{i=1}^{N} \cos\xi_i\right)^2 d\xi_1 \cdots d\xi_N + \frac{1}{N^2}\left(\frac{K}{2\pi}\right)^N \int_{-\frac{\pi}{K}}^{+\frac{\pi}{K}} \cdots \int_{-\frac{\pi}{K}}^{+\frac{\pi}{K}} \left(\sum_{i=1}^{N} \sin\xi_i\right)^2 d\xi_1 \cdots d\xi_N. \tag{C.2}$$

The first term in (C.2) yields

$$\frac{K}{4\pi N}\sin\left(\frac{2\pi}{K}\right) + \frac{1}{2N} + \left(\frac{K}{\pi}\right)^2 \frac{N-1}{N}\sin^2\left(\frac{\pi}{K}\right) \tag{C.3}$$

whereas the second term in (C.2) was already evaluated in Appendix B, Eq. Equation (B.10). The result equals the claim of Proposition 3.

# Appendix D

# Proof of Propositions 4 and 5

Let us lower bound $\mathbb{E}[|\hat{\mathcal{R}}_{N,K,\gamma}|]$ with $\mathbb{E}[\Re(\hat{\mathcal{R}}_{N,K,\gamma})]$ by first finding the distribution of $\Theta$. The received complex signal $r$ in (2.14) can be written as

$$r = \cos\psi + n_{\Re} + j(\sin\psi + n_{\Im}) \tag{D.1}$$

where, if $z$ is a complex scalar, $z_{\Re}$ and $z_{\Im}$ represent its real and imaginary part, respectively. For a given $\psi = \psi'$, $r_{\Re}$ and $r_{\Im}$ are independent Gaussian random variables with variance $\sigma^2/2$ and mean $\cos\psi'$ and $\sin\psi'$, respectively. The PDF of $r$ conditioned on $\psi = \psi'$ is

$$f_{r|\psi=\psi'}(\rho) = \frac{\gamma}{\pi} e^{-\gamma((\rho_{\Re}-\cos\psi')^2+(\rho_{\Im}-\sin\psi')^2)}. \tag{D.2}$$

Based on (D.2), the joint PDF of $A$ and $\Theta$, conditioned on $\psi = \psi'$, is then [102]

$$f_{A,\Theta|\psi=\psi'}(a,\theta) = \frac{\gamma}{\pi} a e^{-\gamma(a^2+1-2a\cos(\theta-\psi'))} \tag{D.3}$$

and, integrating over $a$, we obtain the marginal PDF of $\Theta$ conditioned on $\psi = \psi'$ as

$$f_{\Theta|\psi=\psi'}(\theta) = \int_0^{+\infty} f_{A,\Theta|\psi=\psi'}(a,\theta)da \tag{D.4}$$

$$= \frac{\gamma}{\pi} e^{-\gamma\sin^2(\theta-\psi')} \int_0^{+\infty} a e^{-\gamma(a-\cos(\theta-\psi'))^2} da. \tag{D.5}$$

The integration in (D.5) gives (2.27). The result in (2.25) represents $\mathbb{E}[\Re(\hat{\mathcal{R}}_{N,K,\gamma})]$ because of the following: for a given $\psi'$, depending on the noise realization, the received signal may fall in any of the $K$ different regions. If $\Theta$ falls within $D_k$, a phase shift of $2\pi k/K$ will be applied to the signal, and the phase of its useful part will be $\psi' - 2\pi k/K$. Hence, the useful part of each node's signal becomes a weighted sum of $K$ cosines, whose phases are $\psi' - 2\pi k/K$, for $k = 0, \ldots, K-1$,

and whose weights correspond to the probability of $\Theta$ being in the corresponding decision region $D_k$. The expression is then averaged according to the distribution of $\psi$ that we consider uniform in $[-\pi/K, +\pi/K)$. Due to the symmetry of the system, this is equivalent to considering $\psi$ uniformly distributed in any of the $K$ regions. Proposition 4 is thus proven.

For low SNR, (2.27) expands as

$$f_{\Theta,\gamma|\psi=\psi'}(\theta) = \frac{1}{2\pi} + \sqrt{\gamma}\frac{\cos(\theta-\psi')}{2\sqrt{\pi}} + \gamma\frac{(2\cos^2(\theta-\psi')-1)}{2\pi} + o(\gamma) \tag{D.6}$$

and, plugging (D.6) into (2.26), we obtain

$$\begin{aligned} p_{D_k,\gamma|\psi=\psi'} =& \frac{1}{K} + \sqrt{\frac{\gamma}{\pi}}\sin\left(\frac{\pi}{K}\right)\cos\left(\psi' - \frac{k2\pi}{K}\right) \\ &+ \frac{\gamma}{2\pi}\sin\left(\frac{2\pi}{K}\right)\cos\left(2\psi' - \frac{k4\pi}{K}\right) + o(\gamma). \end{aligned} \tag{D.7}$$

By using (D.7) in (2.25), we obtain:

$$\begin{aligned} \mathbb{E}\left[|\hat{\mathcal{R}}_{N,K,\gamma}|\right] \geq& \frac{1}{\pi}\sin\left(\frac{\pi}{K}\right)\sum_{k=0}^{K-1}\cos\left(\frac{2k\pi}{K}\right) + \sqrt{\frac{\gamma}{\pi}}\frac{K}{8\pi}\sin\left(\frac{\pi}{K}\right)\left[4\pi + 2\sin\left(\frac{2\pi}{K}\right)\right. \\ &\left.\cdot\sum_{k=0}^{K-1}\cos\left(\frac{4k\pi}{K}\right)\right] + \gamma\frac{K}{12\pi^2}\sin\left(\frac{2\pi}{K}\right)\sum_{k=0}^{K-1}\cos\left(\frac{2k\pi}{K}\right)\left[3\sin\left(\frac{\pi}{K}\right)\right. \\ &\left.+ \sin\left(\frac{3\pi}{K}\right)\left(2\cos\left(\frac{4k\pi}{K}\right) - 1\right)\right] + o(\gamma). \end{aligned} \tag{D.8}$$

Expression (D.8) can be simplified by observing that, for every $K$

$$\begin{aligned} \sum_{k=0}^{K-1}\cos\left(\frac{2\pi k}{K}\right) &= \frac{1}{2}\sum_{k=0}^{K-1}\left(e^{j\frac{2\pi k}{K}} + e^{-j\frac{2\pi k}{K}}\right) \\ &= \frac{1}{2}\left(\frac{1-e^{j2\pi}}{1-e^{j\frac{2\pi}{K}}} + \frac{1-e^{-j2\pi}}{1-e^{-j\frac{2\pi}{K}}}\right) \\ &= 0. \end{aligned} \tag{D.9}$$

This is also valid for the summation of $\cos(4k\pi/K)$ terms in (D.8). Hence, the coefficients that multiply the terms of orders 0 and 1 in the expression (D.8) are always zero, and this simplification yields (2.29). This proves Proposition 5.

# Appendix E

# Proof of Proposition 6

Without loss of generality, we can fix $\psi = 0$, which is equivalent to fixing any other value in $[0, 2\pi)$. With that $r = 1 + n$ and (D.2) becomes

$$f_{r|\psi=0}(\rho) = \frac{\gamma}{\pi} e^{-\gamma((\rho_{\Re}-1)^2+\rho_{\Im}^2)}, \tag{E.1}$$

from which $f_{A,\Theta|\psi=0}(a,\theta)$ in turn becomes

$$f_{A,\Theta|\psi=0}(a,\theta) = \frac{a}{\pi}\gamma e^{-\gamma(a^2+1-2a\cos\theta)} \tag{E.2}$$

and the distribution of $\Theta$ conditioned on $\psi = 0$ is given by

$$f_{\Theta|\psi=0}(\theta) = \int_0^{+\infty} f_{A,\Theta}(a,\theta)da \tag{E.3}$$

$$= \frac{\gamma}{\pi} e^{-\gamma\sin^2\theta} \int_0^{+\infty} a e^{-\gamma(a-\cos\theta)^2} da. \tag{E.4}$$

The integration in (E.4) gives

$$f_{\Theta|\psi=0}(\theta) = \frac{1}{2\pi} e^{-\gamma} \left\{ 1 + 2e^{\gamma\cos^2\theta}\sqrt{\pi\gamma}\cos\theta \left[ 1 - \mathcal{Q}\left(\sqrt{2\gamma}\cos\theta\right)\right]\right\}. \tag{E.5}$$

In order to de-condition (E.5), the following integration can be carried out:

$$\int_{-\pi}^{+\pi} f_\Theta(\theta - \psi')\delta(\psi')d\psi' = f_\Theta(\theta) \tag{E.6}$$

because $\psi$ is conditioned to having a punctual deterministic value, and hence its distribution is a delta function.

The first raw moment of the real part of $\hat{\mathcal{R}}_{N,\infty,\gamma}$ can be written as

$$\mathbb{E}\left[\Re\left(\hat{\mathcal{R}}_{N,\infty,\gamma}\right)\right] = \int_{-\pi}^{+\pi} \cos\theta f_\Theta(\theta)d\theta. \tag{E.7}$$

This derives from the fact that the node will rotate its vector exactly by $\theta$, which is the phase observed at the receiver. As a consequence, instead of remaining on the real axis, as it would if the feedback were correct, its phase is centered on zero with distribution $f_\Theta(\cdot)$. In order to integrate (E.7), we proceed as follows: reordering the terms in (E.5), we write

$$f_\Theta(\theta) = \frac{1}{2\pi} e^{-\gamma} + \sqrt{\frac{\gamma}{4\pi}} e^{-\gamma \sin^2 \theta} \cos\theta + \sqrt{\frac{\gamma}{4\pi}} \left(1 - 2\mathcal{Q}(\sqrt{2\gamma}\cos\theta)\right) e^{-\gamma \sin^2 \theta} \cos\theta \tag{E.8}$$

and we then define the integrals

$$\mathcal{I}_1 \triangleq \frac{1}{2\pi} e^{-\gamma} \int_{-\pi}^{+\pi} \cos\theta d\theta \tag{E.9}$$

$$\mathcal{I}_2 \triangleq \sqrt{\frac{\gamma}{4\pi}} \int_{-\pi}^{+\pi} e^{-\gamma \sin^2 \theta} \cos^2\theta d\theta \tag{E.10}$$

$$\mathcal{I}_3 \triangleq \sqrt{\frac{\gamma}{4\pi}} \int_{-\pi}^{+\pi} \left(1 - 2\mathcal{Q}(\sqrt{2\gamma}\cos\theta)\right) e^{-\gamma \sin^2 \theta} \cos^2\theta d\theta \tag{E.11}$$

such that (E.7) is simply $\mathcal{I}_1 + \mathcal{I}_2 + \mathcal{I}_3$. Obviously, (E.9) is zero and (E.11) is also zero because the integrand is an odd function for $\theta \in [-\pi, +\pi)$. In turn, (2.30) admits the closed form that constitutes the claim of Proposition 6.

# Appendix F

# Proof of Propositions 7 and 8

For notational compactness, let us define:

$$x \triangleq \frac{1}{N}\sum_{i=1}^{N} G_i \cos\tilde{\psi}_i \tag{F.1}$$

$$y \triangleq \frac{1}{N}\sum_{i=1}^{N} G_i \sin\tilde{\psi}_i \tag{F.2}$$

where $\tilde{\psi}_1, \ldots, \tilde{\psi}_N$ are a set of independent and identically distributed random variables, uniform in $[-\pi/K, +\pi/K)$ and $G_i$ are Rayleigh distributed with parameter $p$. The NRSS is simply $\sqrt{x^2+y^2}$. For $K \to \infty$, when $N$ is large enough, clearly $x \to \mathbb{E}[G]$ and $y \to 0$.

Thus, we expand the NRSS around $x = \mathbb{E}[G]$ and $y = 0$ obtaining

$$\begin{aligned}\sqrt{x^2+y^2} =& x + \frac{3}{2\mathbb{E}[G]}y^2 - \frac{3}{2\mathbb{E}^2[G]}xy^2 + \frac{1}{2\mathbb{E}^3[G]}x^2y^2 + O\left(y^3\right) + \\ & O\left(y^3\right)(x-\mathbb{E}[G]) + O\left(y^3\right)(x-\mathbb{E}[G])^2 + O\left((x-\mathbb{E}[G])^3\right).\end{aligned} \tag{F.3}$$

We now take expectations over $\tilde{\psi}_1, \ldots, \tilde{\psi}_N$. For the first term in (F.3), we have:

$$\mathbb{E}[x] = \frac{1}{N}\mathbb{E}\left[\sum_{i=1}^{N} G_i \cos\tilde{\psi}_i\right] \tag{F.4}$$

$$= \frac{1}{N}\sum_{i=1}^{N} \mathbb{E}[G_i]\mathbb{E}\left[\cos\tilde{\psi}_i\right] \tag{F.5}$$

$$= \mathbb{E}\left[G\right]\mathbb{E}\left[\cos\tilde{\psi}\right] \tag{F.6}$$

$$= \mathbb{E}[G]\frac{K}{\pi}\sin\left(\frac{\pi}{K}\right) \tag{F.7}$$

$$= \mathbb{E}[G]\left(1 - \frac{\pi^2}{6K^2} + o\left(\frac{1}{K^2}\right)\right). \tag{F.8}$$

For the second term in (F.3), we have:

$$\mathbb{E}[y^2] = \frac{1}{N^2}\mathbb{E}\left[\left(\sum_{i=1}^{N} G_i \sin\tilde{\psi}_i\right)^2\right] \tag{F.9}$$

$$= \frac{1}{N^2}\sum_{i=1}^{N} G_i^2 \mathbb{E}\left[\sin^2\tilde{\psi}_i\right] + \frac{1}{N^2}\sum_{i=1}^{N}\sum_{\substack{j=1\\ j\neq i}}^{N} G_i G_j \mathbb{E}\left[\sin\tilde{\psi}_i \sin\tilde{\psi}_j\right] \tag{F.10}$$

$$= \frac{1}{N}\mathbb{E}[G^2]\left(\frac{1}{2} - \frac{K}{4\pi}\sin\left(\frac{2\pi}{K}\right)\right) \tag{F.11}$$

$$= \frac{\mathbb{E}[G^2]}{N}\left(\frac{\pi^2}{3K^2} + o\left(\frac{1}{K^2}\right)\right). \tag{F.12}$$

For the third term in (F.3), we have:

$$\mathbb{E}[xy^2] = \mathbb{E}\left[\frac{1}{N^3}\left(\sum_{i=1}^{N} G_i\cos\tilde{\psi}_i\right)\left(\sum_{i=1}^{N} G_i\sin\tilde{\psi}_i\right)^2\right] \tag{F.13}$$

$$= \frac{1}{N^3}\mathbb{E}\left[\left(\sum_{i=1}^{N} G_i^3\cos\tilde{\psi}_i\sin^2\tilde{\psi}_i\right)\left(\sum_{i=1}^{N}\sum_{\substack{j=1\\ j\neq i}}^{N} G_i G_j^2\cos\tilde{\psi}_i\sin^2\tilde{\psi}_j\right)\right] \tag{F.14}$$

$$= \frac{1}{N^2}\left(\mathbb{E}[G^3]\mathbb{E}[\cos\tilde{\psi}\sin^2\tilde{\psi}] + N\mathbb{E}[G]\mathbb{E}[G^2]\mathbb{E}[\cos\tilde{\psi}]\mathbb{E}[\sin^2\tilde{\psi}]\right) \tag{F.15}$$

$$= \frac{\mathbb{E}[G^3]}{N^2}\frac{K}{3\pi}\sin^3\left(\frac{\pi}{K}\right) \tag{F.16}$$

$$+ \frac{1}{N}\mathbb{E}[G]\mathbb{E}[G^2]\frac{K}{\pi}\sin\left(\frac{\pi}{K}\right)\left(\frac{1}{2} - \frac{K}{4\pi}\sin\left(\frac{2\pi}{K}\right)\right) \tag{F.17}$$

$$= \frac{1}{N^2}\left(\mathbb{E}[G^3]\frac{\pi^2}{3K^2} + N\mathbb{E}[G]\mathbb{E}[G^2]\frac{\pi^2}{3K^2}\right) + o\left(\frac{1}{K^2}\right). \tag{F.18}$$

For the fourth term in (F.3), we have:

$$\mathbb{E}[x^2y^2] = \mathbb{E}\left[\frac{1}{N^4}\left(\sum_{i=1}^{N} G_i\cos\tilde{\psi}_i\right)^2\left(\sum_{i=1}^{N} G_i\sin\tilde{\psi}_i\right)^2\right] \tag{F.19}$$

$$= \frac{1}{N^4}\mathbb{E}\Bigg[\left(\sum_{i=1}^{N} G_i^2\cos^2\tilde{\psi}_i + \sum_{i=1}^{N}\sum_{\substack{j=1\\ j\neq i}}^{N} G_i G_j\cos\tilde{\psi}_i\cos\tilde{\psi}_j\right) \tag{F.20}$$

$$\cdot\left(\sum_{i=1}^{N} G_i^2\sin^2\tilde{\psi}_i + \sum_{i=1}^{N}\sum_{\substack{j=1\\ j\neq i}}^{N} G_i G_j\sin\tilde{\psi}_i\sin\tilde{\psi}_j\right)\Bigg] \tag{F.21}$$

$$= \frac{1}{N^4}\mathbb{E}\Bigg[\sum_{i=1}^{N} G_i^4\cos^2\tilde{\psi}_i\sin^2\tilde{\psi}_i + \sum_{i=1}^{N}\sum_{\substack{j=1\\ j\neq i}}^{N} G_i^2 G_j^2\cos^2\tilde{\psi}_i\sin^2\tilde{\psi}_j \tag{F.22}$$

$$+ 2\sum_{i=1}^{N}\sum_{\substack{j=1\\ j\neq i}}^{N} G_i^3 G_j \cos\tilde{\psi}_i \sin^2\tilde{\psi}_i \cos\tilde{\psi}_j \tag{F.23}$$

$$+ \sum_{i=1}^{N}\sum_{\substack{j=1\\ j\neq i}}^{N}\sum_{\substack{l=1\\ l\neq i, l\neq j}}^{N} G_i G_j G_l \cos\tilde{\psi}_i \cos\tilde{\psi}_j \sin^2\tilde{\psi}_l \Bigg] \tag{F.24}$$

$$= \frac{1}{N^3}\Big(\mathbb{E}[G^4]\mathbb{E}[\cos^2\tilde{\psi}\sin^2\tilde{\psi}] + N\mathbb{E}^2[G^2]\mathbb{E}[\cos^2\tilde{\psi}]\mathbb{E}[\sin^2\tilde{\psi}] \tag{F.25}$$

$$+ 2N\mathbb{E}[G^3]\mathbb{E}[G]\mathbb{E}[\sin^2\tilde{\psi}\cos\tilde{\psi}]\mathbb{E}[\cos\tilde{\psi}] \tag{F.26}$$

$$+ N^2\mathbb{E}[G^2]\mathbb{E}^2[G]\mathbb{E}^2[\cos\tilde{\psi}]\mathbb{E}[\sin^2\tilde{\psi}]\Big) \tag{F.27}$$

$$= \frac{\mathbb{E}[G^4]}{N^3}\left(\frac{1}{8} - \frac{K}{32\pi}\sin\left(\frac{4\pi}{K}\right)\right) \tag{F.28}$$

$$+ \frac{1}{N^2}\mathbb{E}^2[G^2]\left(\frac{1}{4} - \frac{K^2}{16\pi^2}\sin^2\left(\frac{2\pi}{K}\right)\right) \tag{F.29}$$

$$+ \frac{2}{N^2}\mathbb{E}[G^3]\mathbb{E}[G]\frac{K^2}{3\pi^2}\sin^4\left(\frac{\pi}{K}\right) \tag{F.30}$$

$$+ \frac{1}{N}\mathbb{E}[G^2]\mathbb{E}^2[G]\frac{K^2}{\pi^2}\sin^2\left(\frac{\pi}{K}\right)\left(\frac{1}{2} - \frac{K}{4\pi}\sin\left(\frac{2\pi}{K}\right)\right) \tag{F.31}$$

$$= \frac{\pi^2}{3K^2N^3}\Big(\mathbb{E}[G^4] + N\mathbb{E}^2[G^2] + 2N\mathbb{E}[G^3]\mathbb{E}[G] \tag{F.32}$$

$$+ N^2\mathbb{E}[G^2]\mathbb{E}^2[G]\Big) + o\left(\frac{1}{K^2}\right) \tag{F.33}$$

By putting everything together, according to (F.3), we obtain (2.41).

# Appendix G

# Proof of Proposition 9

The received complex signal in (2.36) can be rewritten as:

$$r = G\cos\psi + n_{\Re} + j(G\sin\psi + n_{\Im}) \tag{G.1}$$

For a given $\psi = \psi'$, and $G = g$, $r_{\Re}$ and $r_{\Im}$ are independent Gaussian random variables with variance $\sigma^2/2$ and mean $g\cos\psi'$ and $g\sin\psi'$, respectively. The PDF of $r$ conditioned on $\psi = \psi'$ and $G = g$ is

$$f_{r|\psi=\psi',G=g}(\rho) = \frac{\gamma}{\pi} e^{-\gamma((\rho_{\Re}-g\cos\psi')^2+(\rho_{\Im}-g\sin\psi')^2)}. \tag{G.2}$$

Based on (G.2), the joint PDF of $A$ and $\Theta$, conditioned on $\psi = \psi'$ and $G = g$ is then [102]

$$f_{A,\Theta|\psi=\psi',G=g}(a,\theta) = \frac{\gamma}{\pi} a e^{-\gamma(a^2+g^2-2ag\cos(\theta-\psi'))} \tag{G.3}$$

and, integrating over $a$, we obtain the marginal PDF of $\Theta$ conditioned on $\psi = \psi'$ and $G = g$ as

$$f_{\Theta|\psi=\psi',G=g}(\theta) = \int_0^{+\infty} f_{A,\Theta|\psi=\psi',G=g}(a,\theta)da \tag{G.4}$$

$$= \frac{\gamma}{\pi} e^{-\gamma g^2\sin^2(\theta-\psi')} \int_0^{+\infty} a e^{-\gamma(a-g\cos(\theta-\psi'))^2} da. \tag{G.5}$$

The integration in (G.5) gives (2.44).

# Appendix H

# Proof of Proposition 10

For low SNR, the marginal PDF of $\Theta$ conditioned on $\psi = \psi'$ and $G = g$ in 2.44, can be expanded as follows:

$$f_{\Theta|\psi=\psi',G=g}(\theta) = \frac{1}{2\pi} + \frac{g\cos(\theta-\psi')}{2\sqrt{\pi}}\sqrt{\gamma} + \frac{g^2\cos\left(2(\theta-\psi')\right)}{2\pi}\gamma + o(\gamma) \tag{H.1}$$

By plugging H.1 into 2.43 we obtain:

$$\begin{aligned} p_{D_k|\psi=\psi',G=g} =& \frac{1}{K} + \sqrt{\frac{\gamma}{\pi}} g \sin\left(\frac{\pi}{K}\right)\cos\left(\psi' - \frac{k2\pi}{K}\right) \\ &+ \frac{\gamma}{2\pi} g^2 \sin\left(\frac{2\pi}{K}\right)\cos\left(2\psi' - \frac{k4\pi}{K}\right) + o(\gamma). \end{aligned} \tag{H.2}$$

By using H.2 in 2.42 we obtain:

$$\begin{aligned} \mathbb{E}\left[|\hat{\mathcal{R}}_{N,K,\gamma,p}|\right] \geq& \frac{p}{\sqrt{2\pi}}\sin\left(\frac{\pi}{K}\right)\sum_{k=0}^{K-1}\cos\left(\frac{k2\pi}{K}\right) \\ &+ \sqrt{\frac{\gamma}{\pi}}\frac{K}{4\pi}\sin\left(\frac{\pi}{K}\right)p^2\left[4\pi - 2\sin\left(\frac{2\pi}{K}\right)\sum_{k=0}^{K-1}\cos\left(\frac{4k\pi}{K}\right)\right] \\ &+ \gamma\frac{K}{4\pi^2}\sqrt{\frac{\pi}{2}}p^3\sin\left(\frac{2\pi}{K}\right)\sum_{k=0}^{K-1}\cos\left(\frac{k2\pi}{K}\right)\left[3\sin\left(\frac{\pi}{K}\right)\right. \\ &\left.+ \sin\left(\frac{3\pi}{K}\right)\left(2\cos\left(\frac{4k\pi}{K}\right) - 1\right)\right] + o(\gamma) \end{aligned} \tag{H.3}$$

Since $\sum_{k=0}^{K}\cos\left(\frac{k2\pi}{K}\right)$ is zero for every $K$, as shown in Section D, expression H.3 reduces to 2.45. Proposition 10 is thus proven.

# Appendix I

# Proof of Propositions 11 and 12

Without loosing generality, $\psi$ can be fixed to be zero. Hence, (G.2) becomes:

$$f_{r|\psi=0,G=g}(\rho) = \frac{\gamma}{\pi} e^{-\gamma((\rho_{\Re}-g)^2+\rho_{\Im}^2)}. \tag{I.1}$$

Based on (I.1), the joint PDF of $A$ and $\Theta$, conditioned on $\psi = 0$ and $G = g$ is then [102]

$$f_{A,\Theta|\psi=0,G=g}(a,\theta) = \frac{\gamma}{\pi} a e^{-\gamma(a^2+g^2-2ag\cos\theta)} \tag{I.2}$$

and, integrating over $a$, we obtain the marginal PDF of $\Theta$ conditioned on $\psi = 0$ and $G = g$ as

$$f_{\Theta|\psi=0,G=g}(\theta) = \int_0^{+\infty} f_{A,\Theta|\psi=0,G=g}(a,\theta)da \tag{I.3}$$

$$= \frac{\gamma}{\pi} e^{-\gamma g^2 \sin^2\theta} \int_0^{+\infty} a e^{-\gamma(a-g\cos\theta)^2} da. \tag{I.4}$$

The integration in (I.4) yields 2.47, since, by de-conditioning with respect to $\psi$, which has as PDF a Delta distribution centred at zero, the function is not affected by any changed as shown in Section D, Eq. (E.6). This then proves Proposition 11.

At low SNR, (2.47) can be expanded as follows:

$$f_{\Theta|G=g}(\theta|G=g) = \frac{1}{2\pi} + \frac{g\cos\theta}{2\sqrt{\pi}}\sqrt{\gamma} + \frac{g\cos 2\theta}{2\pi} g^2 + o(\gamma). \tag{I.5}$$

By plugging I.5 into (2.46), expression (2.48) is obtained.

# Bibliography


[1] R. Mudumbai, J. Hespanha, U. Madhow, and G. Barriac, "Distributed transmit beamforming using feedback control," *IEEE Trans. on Inf. Theory*, vol. 56, no. 1, pp. 411–26, Jan. 2010.

[2] H. L. Van Trees, *Optimum Array Processing (Detection, Estimation, and Modulation Theory, Part IV)*. New York: Wiley, 2002.

[3] H. Unz, "Linear arrays with arbitrarily distributed elements," *IRE Trans. on Anten. Propag.*, vol. 8, no. 2, pp. 222–3, Mar. 1960.

[4] S. Sandler, "Some equivalences between equally and unequally spaced arrays," *IRE Trans. on Anten. Propag.*, vol. 8, no. 5, pp. 496–500, Sep. 1960.

[5] A. Ishimaru, "Theory of unequally-spaced arrays," *IRE Trans. on Anten. Propag.*, vol. 10, no. 6, pp. 691–702, Nov. 1962.

[6] Y. Lo and R. Simcoe, "An experiment on antenna arrays with randomly spaced elements," *IEEE Trans. on Anten. Propag.*, vol. 15, no. 2, pp. 231–5, Mar. 1967.

[7] Y. Lo and S. Lee, "Sidelobe level of non-uniformly spaced antenna arrays," *IEEE Trans. on Anten. Propag.*, vol. 13, no. 5, pp. 817–8, Jul. 1965.

[8] A. Maffet, "Array factors with non-uniform spacing parameter," *IRE Trans. on Anten. Propag.*, vol. 10, no. 2, pp. 131–6, Mar. 1962.

[9] Y. Lo, "A mathematical theory of antenna arrays with randomly spaced elements," *IEEE Trans. on Anten. Propag.*, vol. 12, no. 3, pp. 257–68, May 1964.

[10] M. Donvito and S. Kassan, "Characterization of the random array peak side lobe," *IEEE Trans. on Anten. Propag.*, vol. 27, no. 3, pp. 379–85, May 1979.

[11] A. Panicali and Y. Lo, "A probabilistic approach to large circular and spherical arrays," *IEEE Trans. on Anten. Propag.*, vol. 17, no. 4, pp. 514–22, Jul. 1969.

[12] D. Culler, D. Estrin, and M. Srivastava, "Overview of sensor networks," *IEEE Computer*, vol. 37, no. 8, pp. 41–9, Aug. 2004.

[13] A. D. S. Roy and S. Bandyopadhyay, "Agro-sense: Precision agriculture using sensor-based wireless mesh networks," in *Proc. 1st IEEE ITU-T Kaleidoscope Academic Conference, (K-INGN)*, Geneva, May 2008, pp. 383–8.

[14] T. Ahonen, R. Virrankoski, and M. Elmusrati, "Greenhouse monitoring with wireless sensor network," in *Proc. IEEE/ASME International Conference on Mechtronic and Embedded Systems and Applications, (MESA)*, Beijing, China, Oct. 2008, pp. 403–8.

[15] X. Jiang, Y. Tang, and Y. Lei, "Wireless sensor networks in structural health monitoring based on ZigBee technology," in *Proc. IEEE 3rd International Conference on Anti-counterfeiting, Security, and Identification in Communication, (ASID)*, Hong Kong, China, Aug. 2009, pp. 449–52.

[16] G. Hackmann, S. Fei, N. Castaneda, L. C. Lu, and S. Dyke, "A holistic approach to decentralized structural damage localization using wireless sensor networks," in *Proc. IEEE Real-Time Systems Symposium, (RTSS)*, Barcelona, Spain, Nov. 2008, pp. 35–46.

[17] T. D. Räty, "Survey on contemporary remote surveillance systems for public safety," *IEEE Trans. on Systems, Man, and Cybernetics, Part C: Applications and Reviews*, vol. 40, no. 5, pp. 493–515, Sep. 2010.

[18] S. K. Udgata, G. Sindhura, and S. L. Sabat, "A novel architecture for intelligent and adaptive wireless-sensor-network-based alarming system," in *Proc. 5th IEEE Conference on Wireless Communication and Sensor Networks, (WCSN)*, Allahabad, India, Dec. 2009, pp. 1–6.

[19] P. J. Pramod, S. V. Srikanth, N. Vivek, M. U. Patil, and C. Sarat, "Intelligent intrusion detection system (In2DS) using wireless sensor networks," in *Proc. International Conference on Networking, Sensing and Control, (ICNSC)*, Okayama, Japan, Mar. 2009, pp. 587–91.

[20] D. Han and J. Lim, "Smart home energy management system using IEEE 802.15.4 and ZigBee," *IEEE Trans. on Consumer Electronics*, vol. 56, no. 3, pp. 1403–10, Aug. 2010.

[21] J. K. Hart and K. Martinez, "Environmental sensor networks: A revolution in the earth system science?" *Earth-Science Reviews*, vol. 78, no. 3-4, pp. 177–91, Oct. 2006.

[22] G. J. Pendock, L. Evans, and G. Coulson, "Wireless sensor module for habitat monitoring," in *Proc. IEEE 3rd International Conference on Intelligent Sensors, Sensor Networks and Information, (ISSNIP)*, Melbourne, Australia, Dec. 2007, pp. 699–702.

[23] A. M. C. Lee, C. T. Angeles, M. C. R. Talampas, L. G. Sison, and M. N. Soriano, "MotesArt: Wireless sensor network for monitoring relative humidity and temperature in an art gallery," in *Proc. IEEE International Conference on Networking, Sensing and Control, (ICNSC)*, Sanya, China, Apr. 2008, pp. 1263–8.

[24] R. C. Wasielewski, "Wireless technologies for the orthopaedics: Diagnostics and surgical applications," in *Proc. IEEE Topical Conference on Biomedical Wireless Technologies, Networks, and Sensing Systems, (BioWireleSS)*, Phoenix, AZ, Jan. 2011, pp. 1–2.

[25] C. Li and X. Wang, "Cooperative multibeamforming in ad hoc networks," *EURASIP Journal on Advances in Signal Processing*, vol. 2008, p. 66, 2008.

[26] D. R. Brown, U. Madhow, P. Bidigare, and S. Dasgupta, "Receiver-coordinated distributed transmit nullforming with channel state uncertainty," in *Proc. 46th Annual Conference on Information Sciences and Systems (CISS)*, Mar. 2012, pp. 1–6.

[27] A. F. Dana and B. Hassibi, "On the power efficiency of sensory and ad hoc wireless networks," *IEEE Trans. on Inf. Theory*, vol. 52, no. 7, pp. 2890–914, Jul. 2006.

[28] H. Rahul, S. Kumar, and D. Katabi, "JMB: Scaling wireless capacity with user demands," in *Proc. of the ACM Conf. on Applications, Technologies, Architectures, and Protocols for Computer Communication (SIGCOMM)*, Helsinki, Finland, Aug. 2012, pp. 235–46.

[29] C. Asensio-Marco and B. Beferull-Lozano, "Accelerating consensus gossip algorithms: Sparsifying networks can be good for you," in *Proc. IEEE Int. Conf. on Comm. (ICC)*, Cape Town, South Africa, May 2010, pp. 1–5.

[30] L. Dong, A. P. Petropulu, and H. V. Poor, "A cross-layer approach to collaborative beamforming for wireless ad hoc networks," *IEEE Trans. Signal Proc.*, vol. 56, no. 7, pp. 2981–93, Jul. 2008.

[31] L. Dong and A. Petropulu, "A comparison of cooperative beamforming to direct transmission based on spectral efficiency," in *Proc. 42nd Annual Conf. on Information Sciences and Systems, (CISS)*, Princeton, NJ, Mar. 2008, pp. 423–8.

[32] L. Dong, A. P. Petropulu, and H. V. Poor, "Weighted cross-layer cooperative beamforming for wireless networks," *IEEE Trans. Signal Proc.*, vol. 57, no. 8, pp. 3240–52, Aug. 2009.

[33] Y. Jing and H. Jafarkhani, "Network beamforming using relays with perfect channel information," *IEEE Trans. on Inf. Theory*, vol. 55, no. 6, pp. 2499–517, Jun. 2009.

[34] V. Havary-Nassab, S. Shahbazpanahi, A. Grami, and Z. Luo, "Distributed beamforming for relay networks based on second-order statistics of the channel state information," *IEEE Trans. on Sig. Proc.*, vol. 56, no. 9, pp. 4306–16, Sep. 2008.

[35] Y. Jing and H. Jafarkhani, "Network beamforming with channel means and covariances at relays," in *Proc. IEEE Int. Conf. on Commun. (ICC)*, Beijing, China, May 2008, pp. 3743–7.

[36] E. Koyuncu, Y. Jing, and H. Jafarkhani, "Distributed beamforming in wireless relay networks with quantized feedback," *IEEE Jour. on Selected Areas in Comm.*, vol. 26, no. 8, pp. 1429–39, Oct. 2008.

[37] G. Zheng, K. K. Wong, A. Paulraj, and B. Ottersten, "Robust and distributed beamforming," in *Proc. Int. Conf. Wir. Commun. Sig. Proces. (WCSP)*, Nanjing, China, Nov. 2009, pp. 1–5.

[38] A. Talebi and W. A. Krzymién, "Multiple-antenna multiple-relay cooperative communication system with beamforming," in *Proc. IEEE 67th Vehicular Tech. Conf. (VTC Spring)*, Marina Bay, Singapore, May 2008, pp. 2350–4.

[39] A. G. Marques, X. Wang, and G. B. Giannakis, "Minimizing transmit power for coherent communications in wireless sensor networks with finite-rate feedback," *IEEE Trans. on Sig. Proc.*, vol. 56, no. 9, pp. 4446–57, Sep. 2008.

[40] C. Wang, Q. Yin, J. Zhang, B. Hao, and W. Li, "Distributed transmit beamforming without phase feedback," *EURASIP Journal on Wireless Communications and Networking*, vol. 2010, pp. 4:1–4:8, Apr. 2010.

[41] V. Tarokh, Y. S. Choi, and S. Alamouti, "Complementary beamforming," in *Proc. IEEE 58th Vehicular Technology Conf. (VTC Fall)*, Taiwan, Oct. 2003, pp. 3136–40.

[42] Y. S. Choi, S. M. Alamouti, and V. Tarokh, "Complementary beamforming: New approaches," *IEEE Trans. on Comm.*, vol. 54, no. 1, pp. 41–50, Jan. 2006.

[43] V. Tarokh, Y. S. Choi, and S. Alamouti, "Complementary beamforming methods and apparatuses," *US Patent*, no. 7,099,698 B2, Aug. 29, 2006.

[44] K. Zarifi, A. Ghrayeb, and S. Affès, "Distributed beamforming for wireless sensor networks with improved graph connectivity and energy efficiency," *IEEE Trans. on Sig. Proc.*, vol. 58, no. 3, pp. 1904–21, Mar. 2010.

[45] K. Zarifi, S. Affès, and A. Ghrayeb, "Collaborative null-steering beamforming for uniformly distributed wireless sensor networks," *IEEE Trans. on Sig. Proc.*, vol. 58, no. 3, pp. 1889–1903, Mar. 2010.

[46] M. F. A. Ahmed and S. Vorobyov, "Collaborative beamforming for wireless sensor networks with Gaussian distributed sensor nodes," *IEEE Trans. on Wireless Comm.*, vol. 8, no. 2, pp. 638–43, Feb. 2009.

[47] K. Zarifi, S. Affès, and A. Ghrayeb, "Distributed beamforming for wireless sensor networks with random node location," in *Proc. IEEE Int. Conf. Acoustics, Speech and Sig. Processing (ICASSP)*, Taipei, Taiwan, Apr. 2009, pp. 2261–4.

[48] K. Hardwick, D. Goeckel, and D. Towsley, "Modeling distributed beamforming in wireless networks," in *Proc. IEEE 46th Annu. Allerton Conf. on Comm., Control, and Comp.*, Illinois, USA, Sep. 2008, pp. 475–82.

[49] H. Ochiai, P. Mitran, H. V. Poor, and V. Tarokh, "Collaborative beamforming for distributed wireless ad hoc networks," *IEEE Trans. Signal Proc.*, vol. 53, no. 11, pp. 4110–24, Nov. 2005.

[50] R. Mudumbai, G. Barriac, and U. Madhow, "On the feasibility of distributed beamforming in wireless networks," *IEEE Trans. on Wireless Comm.*, vol. 6, no. 5, pp. 1754–63, May 2007.

[51] Y. Lebrun, K. Zhao, S. Pollin, A. Bourdoux, F. Horlin, and R. Lauwereins, "Performance analysis of distributed ZF beamforming in the presence of CFO," *EURASIP Journal on Wireless Communications and Networking*, vol. 2011, no. 1, p. 177, 2011.

[52] R. Mudumbai, B. Wild, U. Madhow, and K. Ramchandran, "Distributed beamforming using 1 bit feedback: From concept to realization," in *Proc. 44th Annu. Allerton Conf. Commun., Control and Computing*, Monticello, IL, Sep. 2006, pp. 1020–7.

[53] R. Mudumbai, J. Hespanha, U. Madhow, and G. Barriac, "Scalable feedback control for distributed beamforming in sensor networks," in *Proc. IEEE Int. Symp. on Inf. Theory (ISIT)*, Adelaide, Australia, Sep. 2005, pp. 137–41.

[54] G. Barriac, R. Mudumbai, and U. Madhow, "Distributed beamforming for information transfer in sensor networks," in *Proc. 3rd Int. Symp. Inf. Processing in Sensor Netw. (IPSN)*, Berkeley, CA, Apr. 2004, pp. 81–8.

[55] C. Lin, V. V. Veeravalli, and S. P. Meyn, "A random search framework for convergence analysis of distributed beamforming with feedback," *IEEE Trans. on Inf. Theory*, vol. 56, no. 12, pp. 6133–41, Dec. 2010.

[56] M. Seo, M. Rodwell, and U. Madhow, "A feedback-based distributed phased array technique and its application to *Proc. IEEE MTT-S International Microwave Symposium Digest (MTT-S)*, Atlanta, GA, Jun. 2008, pp. 683–6.

[57] S. Song, J. S. Thompson, P. J. Chung, and P. M. Grant, "Improving the one-bit feedback algorithm for distributed beamforming," in *Proc. Wireless Comm. and Networking Conf. (WCNC)*, Sydney, Australia, Apr. 2010, pp. 1–6.

[58] J. A. Bucklew and W. A. Sethares, "Convergence of a class of decentralized beamforming algorithms," *IEEE Trans. on Sig. Pro.*, vol. 56, no. 6, pp. 2280–8, Jun. 2008.

[59] C. S. Tseng, C. C. Chen, and C. Lin, "A bio-inspired robust adaptive random search algorithm for distributed beamforming," in *Proc. IEEE Int. Conf. on Communications (ICC)*, Kyoto, Japan, Jun. 2011, pp. 1–6.

[60] J. Thukral and H. Bölcskei, "Distributed spatial multiplexing with 1-bit feedback," in *Proc. 45th Annu. Allerton Conf. Commun., Control and Computing*, Monticello, IL, Sep. 2007, pp. 502–9.

[61] L. Berbakov, C. A. Haro, and J. Matamoros, "Distributed beamforming using one bit of feedback: AWGN analysis," in *Proc. 18th European Wireless Conference (EW)*, Poznán, Poland, Apr. 2012, pp. 1–4.

[62] W. Haijie, Y. Ding, and H. M. Kwon, "Phase synchronization for distributed sensor networks in feedback bit errors," in *Proc. IEEE Int. Conf. on Wireless Comm., Networking and Information Security (WCNIS)*, Beijing, China, Jun. 2010, pp. 282–6.

[63] W. Tushar, D. Smith, A. Zhang, T. Lamahewa, and T. Abhayapala, "Distributed transmit beamforming: Phase convergence improvement using enhanced one-bit feedback," in *Proc. IEEE Wireless Comm. and Networking Conference (WCNC)*, Paris, France, Apr. 2012, pp. 528–32.

[64] G. Lim and L. J. Cimini, "Partitioned one-bit feedback for cooperative beamforming," in *Proc. 44th Annual Conf. on Information Sciences and Syst. (CISS)*, Princeton, NJ, Mar. 2010, pp. 1–5.

[65] L. Berbakov, C. Anton-Haro, and J. Matamoros, "Distributed beamforming with sidelobe control using one bit of feedback," in *Proc. IEEE 73rd Vehicular Technology Conference (VTC Spring)*, May 2011, pp. 1–5.

[66] F. Quitin, U. Madhow, M. Rahman, and R. Mudumbai, "Demonstrating distributed transmit beamforming with software-defined radios," in *Proc. 13th IEEE Int. Symp. on a World of Wireless, Mobile and Multimedia Networks (WoWMoM)*, San Francisco, CA, Jun. 2012, pp. 1–3.

[67] P. Fertl, A. Hottinen, and G. Matz, "Perturbation-based distributed beamforming for wireless relay networks," in *Proc. IEEE Global Telecom. Conf. (GLOBECOM)*, New Orleans, LA, Nov. 2008, pp. 1–5.

[68] M. Johnson, M. Mitzenmacher, and K. Ramchandran, "Distributed beamforming with binary signaling," in *Proc. IEEE Int. Symp. on Inf. Theory (ISIT)*, Toronto, Canada, Jul. 2008, pp. 890–4.

[69] P. Jeevan, S. Pollin, A. Bahai, and P. P. Varaiya, "Pairwise algorithm for distributed transmit beamforming," in *Proc. IEEE Int. Conf. on Communications (ICC)*, Beijing, China, May 2008, pp. 4245–9.

[70] Y.-S. Tu and G. Pottie, "Coherent cooperative transmission from multiple adjacent antennas to a distant stationary antenna through AWGN channels," in *Proc. IEEE 55th Vehicular Tech. Conf., (VTC Spring)*, vol. 1, Birmingham, AL, May 2002, pp. 130–4.

[71] D. R. Brown, P. Bidigare, and U. Madhow, "Receiver-coordinated distributed transmit beamforming with kinematic tracking," in *Proc. IEEE Int. Conf. on Acoustics, Speech and Signal Processing (ICASSP)*, Mar. 2012, pp. 5209–12.

[72] D. R. Brown, G. Prince, and J. McNeill, "A method for carrier frequency and phase synchronization of two autonomous cooperative transmitters," in *Proc. IEEE 6th Workshop on Signal Processing Adv. Wireless Commun.*, New York, NY, Jun. 2005, pp. 260–4.

[73] I. Ozil and D. R. Brown, "Time-slotted round-trip carrier synchronization," in *Proc. 41st Asilomar Conf. Signals, Sys., Comp.*, Pacific Grove, CA, Nov. 2007, pp. 1781–5.

[74] D. R. Brown and H. V. Poor, "Time-slotted round trip carrier synchronization for distributed beamforming," *IEEE Trans. on Sig. Pro.*, vol. 56, no. 11, pp. 5630–43, Nov. 2008.

[75] R. D. Preuss and D. R. Brown, "Retrodirective distributed transmit beamforming with two-way source synchronization," in *Proc. 44th Annual Conference on Information Sciences and Systems (CISS)*, Mar. 2010, pp. 1–6.

[76] M. F. A. Ahmed and S. A. Vorobyov, "Sidelobe control in collaborative beamforming via node selection," *IEEE Trans. on Signal Proc.*, vol. 58, no. 12, pp. 6168–80, Dec. 2010.

[77] M. O. Pun, D. R. Brown, and H. V. Poor, "Opportunistic collaborative beamforming with one-bit feedback," *IEEE Trans. on Wireless Comm.*, vol. 8, no. 5, pp. 2629–41, May 2009.

[78] M. F. A. Ahmed and S. A. Vorobyov, "Node selection for sidelobe control in collaborative beamforming for wireless sensor networks," in *Proc. IEEE 10th Workshop on Sig. Processing Advances in Wireless Comm. (SPAWC)*, Perugia, Italy, Jun. 2009, pp. 519–23.

[79] C. W. Chang, A. Kothari, A. Jafri, D. Koutsonikolas, D. Peroulis, and Y. C. Hu, "Radiating sensor selection for distributed beamforming in wireless sensor networks," in *Proc. IEEE Military Comm. Conf. (MILCOM)*, San Diego, CA, Nov. 2008, pp. 1–7.

[80] T. Stevens and K. Kastella, "Network localization for distributed transmit beam forming with mobile radios," in *Proc. IEEE Int. Conf. on Acoustics, Speech and Signal Processing (ICASSP)*, Mar. 2012, pp. 5217–20.

[81] D. R. Brown, R. Mudumbai, and S. Dasgupta, "Fundamental limits on phase and frequency tracking and estimation in drifting oscillators," in *Proc. IEEE Int. Conf. on Acoustics, Speech and Signal Processing (ICASSP)*, Mar. 2012, pp. 5225–28.

[82] A. Bletsas, A. Lippman, and J. N. Sahalos, "Simple, zero-feedback, distributed beamforming with unsynchronized carriers," *IEEE Journal on Selected Areas in Comm.*, vol. 28, no. 7, pp. 1046–54, Sep. 2010.

[83] ——, "Zero-feedback, collaborative beamforming for emergency radio: Asymptotic analysis," *Mob. Netw. Appl.*, vol. 16, no. 5, pp. 589–99, Oct. 2011.

[84] R. Mudumbai, P. Bidigare, S. Pruessing, S. Dasgupta, M. Oyarzun, and D. Raeman, "Scalable feedback algorithms for distributed transmit beamforming in wireless networks," in *Proc. IEEE Int. Conf. on Acoustics, Speech and Signal Processing (ICASSP)*, Mar. 2012, pp. 5213–16.

[85] A. Demir, A. Mehrotra, and J. Roychowdhury, "Phase noise in oscillators: a unifying theory and numerical methods for characterization," *IEEE Trans. on Circuits and Systems I: Fundamental Theory and Applications*, vol. 47, no. 5, pp. 655–74, May 2000.

[86] H. Robbins and S. Monro, "A stochastic approximation method," *The Annals of Mathematical Statistics*, vol. 22, no. 3, pp. 400–7, Sep. 1951.

[87] L. Cottatellucci, M. Debbah, G. Gallinaro, M. N. R. Müller, and R. Rinaldo, "Interference mitigation techniques for broadband satellite systems," in *Proc. 24th AIAA Int. Commun. Satell. Systems Conf., (ICSSC)*, San Diego, CA, Jun. 2006.

[88] J. Litva and T. K. Lo, *Digital Beamforming in Wireless Communications*. Boston - London: Artech House, 1996.

[89] P. Angeletti and N. Alagha, "Space/Ground beamforming techniques for emerging hybrid satellite terrestrial networks," in *Proc. 27th AIAA Int. Commun. Satell. Systems Conf., (ICSSC)*, Edinburgh, UK, Jun. 2009.

[90] P. Angeletti, G. Gallinaro, M. Lisi, and A. Vernucci, "On-ground digital beamforming techniques for satellite smart antennas," in *Proc. 19th AIAA Int. Commun. Satell. Systems Conf., (ICSSC)*, Toulouse, France, Apr. 2001, pp. 1–8.

[91] P. D. Karabinis, "Systems and methods for reducing satellite feeder link bandwidth/carriers in cellular satellite systems," *US Patent*, no. 2003/0224785 A1, Dec. 4, 2003.

[92] P. D. Karabinis, S. Dutta, and G. G. Churan, "Satellite communications systems and methods using radio telephone location-based beamforming," *US Patent*, no. WO2005/117288 A2, Dec. 8, 2005.

[93] V. S. Reinhardt, "Hybridized space/ground beamforming," *US Patent*, no. 6,571,081 B1, May 27, 2003.

[94] A. W. A. Draganov, "Optimized beamforming for satellite communication," *US Patent*, no. 2010/0194630 A1, Aug. 5, 2010.

[95] B. Devillers, A. Pérez-Neira, and C. Mosquera, "Joint linear precoding and beamforming for the forward link of multi-beam broadband satellite systems," in *Proc. IEEE Global Telecom. Conf. (GLOBECOM)*, Houston, TX, Dec. 2011, pp. 1–6.

[96] J. Arnau-Yañez, M. Bergmann, E. A. Candreva, G. E. Corazza, R. de Gaudenzi, B. Devillers, W. Gappmair, F. Lombardo, C. Mosquera, A. Pérez-Neira,

I. Thibault, and A. Vanelli Coralli, "Hybrid space-ground processing for high-capacity multi-beam satellite systems," in *Proc. IEEE Global Communications Conference, (GLOBECOM)*, Houston, TX, Dec. 2011, pp. 1–6.

[97] I. Thibault, F. Lombardo, E. A. Candreva, A. V. Coralli, and G. E. Corazza, "Coarse beamforming techniques for multi-beam satellite networks," in *Proc. IEEE Int. Conf. on Comm. (ICC)*, Ottawa, Canada, Jun. 2012.

[98] ESA, private communication to SatNEx III team members, "Antenna pattern data."

[99] G. W. Stewart, *Matrix Algorithms: vol. I Basic Decompositions*. Siam, 1998.

[100] C. Peel, B. Hochwald, and A. Swindlehurst, "A vector perturbation technique for near capacity multiantenna multiuser communication - Part I: Channel inversion and regularization," *IEEE Trans. on Comm.*, vol. 3, no. 1, pp. 195–202, Jan. 2005.

[101] ETSI TR 102 376, "DVB-S2: Digital Video Broadcasting (DVB) user guidelines, for the second generation system for broadcasting, interactive services, news gathering, and other broadband satellite applications (DVB-S2)."

[102] J. G. Proakis and M. Salehi, *Digital Communications*. Boston: McGraw Hill, 2008.